DISSERTATION

Electron Stimulated Desorption
of Condensed Gases
on Cryogenic Surfaces

ausgeführt zum Zwecke der Erlangung des akademischen
Grades eines Doktors der technischen Wissenschaften

unter der Leitung von

Prof. Dr. Herbert Störi
E134 – Institut für Allgemeine Physik

under the supervision of

Dr. Noël Hilleret
CERN – AT – VAC

eingereicht an der Technischen Universität Wien
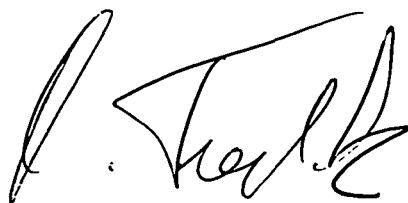Fakultät für Technische Naturwissenschaften und Informatik

von

Dipl. Ing. Herbert Tratnik
Matrikelnr. 9226169
CH-1223 Cologny, Chemin de Planta 5

Wien, im September 2005

Kurzfassung

In den meisten Ultrahochvakuumanlagen bestimmen die Gasabgabe von Festkörpern und die Desorption von Oberflächenadsorbaten Enddruck und Zusammensetzung des Restgases. Speziell im Strahlvakuum von Beschleunigern wie dem LHC, wo Oberflächen intensiver Synchrotronstrahlung und Beschuss durch energetische Ionen und Elektronen ausgesetzt sind, können Oberflächeneigenschaften wie Desorptionsrate oder Sekundärelektronenrate den Betrieb des Beschleunigers wesentlich beeinflussen.

In Teilchenbeschleunigern, die bei flüssiger Heliumtemperatur arbeiten, sind die kalten Oberflächen dem Beschuss von energetischen Photonen, Elektronen und Ionen ausgesetzt. Die durch die ständige Desorption frei werdenden Gase, kondensieren erneut an den kalten Oberflächen und werden wieder von den auftreffenden Elektronen und Ionen desorbiert. Das nach einiger Zeit entstehende Gleichgewicht der Gasbedeckung auf den Oberflächen, die dem Beschuss der energetischen Teilchen ausgesetzt sind, hängt von der Desorptionsrate des kondensierten Gases ab und kann den Betrieb des Beschleunigers durch die veränderte Sekundärelektronenrate dieser Oberflächen beeinflussen.

Es wurden die Desorptionsraten von verschiedenen Gasen die auf einer 4.2 K gekühlten Kupferoberfläche kondensieren unter Elektronenbeschuss gemessen. Diese sind zusammen mit den Werten des Haftungskoeffizienten von diesen Gasen bei 4.2 K dargestellt. Ein Modell um die Veränderungen der Desorptionsrate mit der Oberflächenbedeckung zu erklären wird ebenfalls beschrieben.

In dieser Arbeit wurde die elektronenstimulierte Desorptionsrate bei tiefen Temperaturen gemessen. Dieser Parameter ist von Wichtigkeit um das Vakuumverhalten im LHC unter Anwesenheit einer Elektronenwolke zu verstehen und vorauszusagen, da in diesem Fall die elektronenstimulierte Desorptionsrate die Hauptgasquelle ist. Von speziellem Interesse ist die Veränderung der elektronenstimulierten Desorptionsrate mit der Gasbedeckung, weil die meisten Gase, mit Ausnahme von Wasserstoff, auf der Strahlrohroberfläche kondensieren und dies zu einer Erhöhung der Moleküldichte pro Einheitsfläche führt. Die Messung der elektronenstimulierten Desorptionsrate benötigt ein System wo man erstens die Anzahl der Elektronen, die dann auf die auf Heliumtemperatur gekühlte Probe beschleunigt werden, kennt; zweitens, die Art und Menge der desorbierenden Moleküle messen kann und drittens eine vorherbestimmte Gasmenge hineinströmen lassen kann welches an der kalten Probe kondensiert.

Abstract

In ultra-high vacuum systems outgassing from vacuum chamber walls and desorption from surface adsorbates are usually the factors which influence pressure and residual gas composition. In particular in beam vacuum systems of accelerators like the LHC, where surfaces are exposed to intense synchrotron radiation and bombardment by energetic ions and electrons, properties like the molecular desorption yield or secondary electron yield can strongly influence the performance of the accelerator.

In high-energy particle accelerators operating at liquid helium temperature, cold surfaces are exposed to the bombardment of energetic photons, electrons and ions. The gases released by the subsequent desorption are re-condensed on the cold surfaces and can be re-desorbed by the impinging electrons and ions. The equilibrium coverage reached on the surfaces exposed to the impact of energetic particles depends on the desorption yield of the condensed gases and can affect the operation of the accelerator by modifying the secondary electron yield of these surfaces.

The desorption yields under electron impact of various gases condensed on a copper surface cooled at 4.2K have been measured and will be presented together with the values of the sticking coefficient of these gases on a 4.2K condensing surface. A model to explain the variation of the desorption yields with the surface coverage will also be described.

In this work the electron stimulated desorption yield (ESDY) at cryogenic temperatures has been measured. This parameter is of importance to understand and predict the vacuum behavior in the LHC, in the presence of an electron cloud, as in that case the electron induced desorption will be the main gas source. Of particular interest is the variation of the electron induced desorption yield with the gas coverage as most gases (with the exception of hydrogen) condense on the beam screen surface, which leads to an increased density of molecules per unit area. The measurement of the ESDY requires a measuring system where first a known amount of electrons can be accelerated to a target cooled at helium temperature, second the nature and the number of desorbed molecules can be measured and third a predetermined quantity of gas can be injected and condensed on the cold target.

Contents

List of Tables

List of Figures

Chapter 1

Overview

The subject of this thesis is to measure the electron stimulated desorption yield (ESDY) of condensed gases at cryogenic temperatures. Carried out in the vacuum group at the AT department at CERN its motivation originates from the special requirements on the beam vacuum of the LHC and surfaces exposed to this vacuum.

An introduction of CERN and the LHC is given in chapter 2. Special emphasis is put on the LHC vacuum system and beam related dynamic vacuum effects which are described in more detail.

In chapter 3, models for sticking probability and electron stimulated desorption are presented.

Experiments that investigate the effects of electron stimulated desorption from cryogenic surfaces are described in chapters 4 and 5. These experiments are of phenomenological nature, i. e. their results describe the change of surface properties like molecular desorption yield, secondary electron yield and chemical composition of a surface due to a particular gas injection which condense on a surface and not the fundamental physical process that lead to this changes.

In part III an application to the LHC Beam Vacuum System is presented. In chapter 6 predictions for the beam related dynamic vacuum effects are described.

Finally, a summary and a conclusion is presented.

This thesis does not have a distinct theory part. Instead, theoretical pre - requisites for a particular experiment are presented where they are needed. The same holds for the results, which for each experiment (or simulation) are given at the end of the corresponding chapter.

Chapter 2

CERN and the LHC

2.1 A short introduction of CERN

CERN [1] - *Centre Européene pour la Recherche Nucléaire*, the European Organization for Nuclear Research - was founded in 1954 by 12 European states with the intention to re-establish fundamental physics research in the post world war II Europe. Since then the number of states has been increasing up to the present number of 20: Austria, Belgium, Bulgaria, Czech Republic, Denmark, Finland, France, Germany, Greece, Hungary, Italy, Netherlands, Norway, Poland, Portugal, Slovak Republic, Spain, Sweden, Switzerland and the United Kingdom. Currently CERN employs just under 3000 people of different skills and professions and additionally about 6500 scientists from all over the world come to CERN to do their research, thus making it one of the biggest research institutes for high energy physics in the world.

Since many years particle accelerators have been representing the most powerful tools for researchers in high energy physics. Hence, the development and construction of particle accelerators has been one of CERN's main tasks since its first days. CERN's accelerator complex, consisting of linear and circular machines, is now the most versatile in the world providing beams of a variety of particles in a large range of energies.

Thus, since its beginning, CERN has been providing the means of the high energy physics community to make new discoveries and to test existing theories with precision measurements. It has been helping to establish our present picture of the elementary particles and their interactions - the so called *standard model of particle physics*.[1]

---

[1] For a history of particle physics cf. [2], for an introduction to the standard model of particle physics cf. [3]

Despite the success of the standard model, whose prediction could be verified at the level of 0.1% or better by experiments at LEP, SVC and Tevatron, some aspects of the theory are still obscure and there are several reasons to believe that this is not the ultimate theory of particle physics [4]. Hence, there are strong physics arguments to continue fundamental research at even higher energies. Motivated and supported by these arguments, an even more powerful accelerator, the LHC, is currently under construction at CERN, and is due to become operational in 2007.

2.2 The LHC project

The LHC, the *Large Hadron Collider*, has been designed to collide protons at a center-of-mass energy of 14 TeV with a luminosity of 10^{34} cm^{-2} · s^{-1} [5, 6]. In addition it will provide collisions between lead nuclei up to a center-of-mass energy of 1150 TeV.[2] A list of LHC design parameters is given in Appendix B.

The LHC will be placed into the existing tunnel of the LEP collider, the *Large Electron Positron Collider*, whose operation had been stopped at the end of 2000 and which has been dismantled. Following this tunnel, the LHC will have a circumference of about 26.7 km. As shown in figure 2.1 the general layout of the LHC has an eightfold structure, thereby following the layout of its predecessor LEP. Each of these octants consits of an *arc*, which basically contains the main bending magnets (the *main dipoles*), focussing (quadrupole) magnets and higher order correction magnets, followed by a so called *long straight section*[3] with a length of about 500 m.

The two proton beams, each made up of 2835 tightly packed *bunches* of protons (1.05 × 10^{11} protons per bunch), resulting in a current of 0.536 A per beam, will be circulating in clockwise and anti-clockwise direction in two separate beam pipes which are inserted into a common bending magnet. These beams are brought in collision at four points called *interaction points*.

At these four interaction points huge particle detectors will be installed to measure properties like energy and momentum of the particles emerging from the interaction point after the collision of high energetic particles. These detectors, depicted in figure 2.2, are:

---

[2]This corresponds to 2 × 82 × 7 TeV, since a lead nucleus contains 82 protons. (In reality, this means, each lead nucleus has only 82/208 × 7 ≈ 2.76 TeV/nucleon. This is due the extra mass of the neutrons in the nuclei.)

[3]there are also so called *short straight sections* which are considered as a part of the arcs.

4
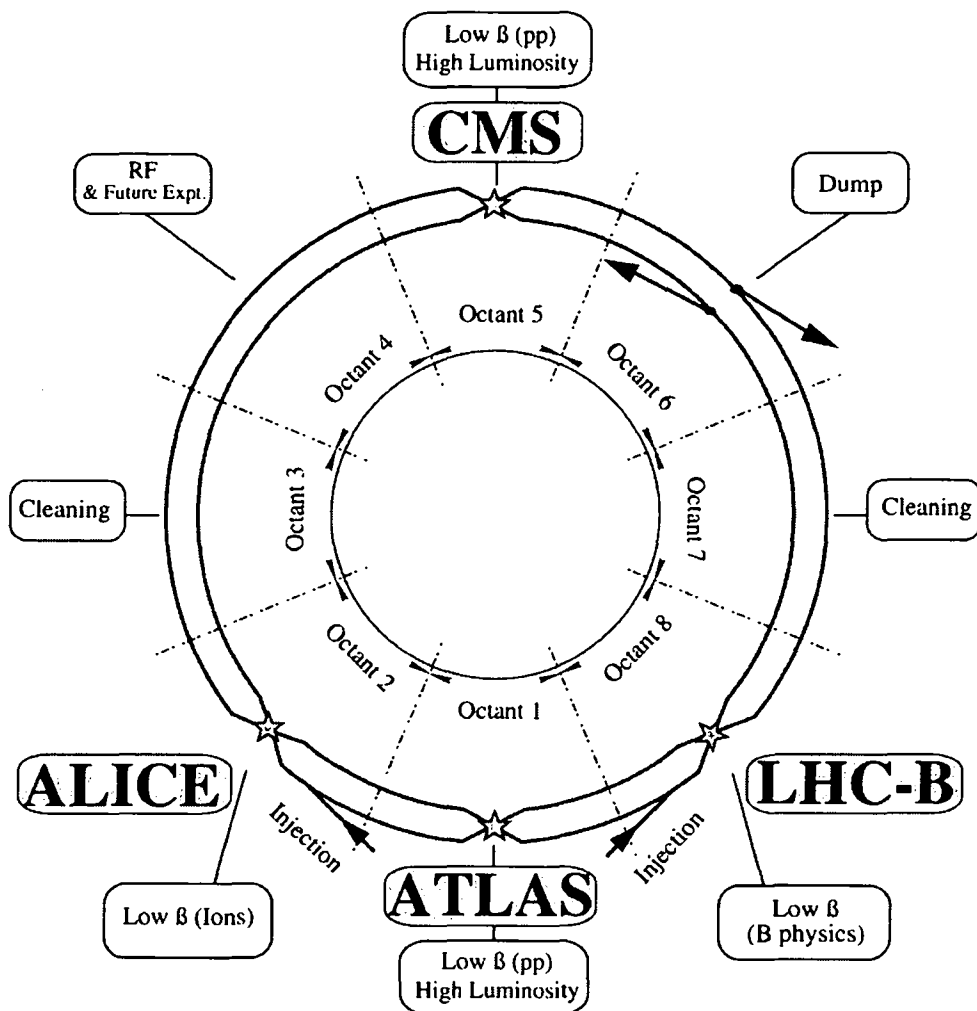
Figure 2.1: General Layout of the Large Hadron Collider.
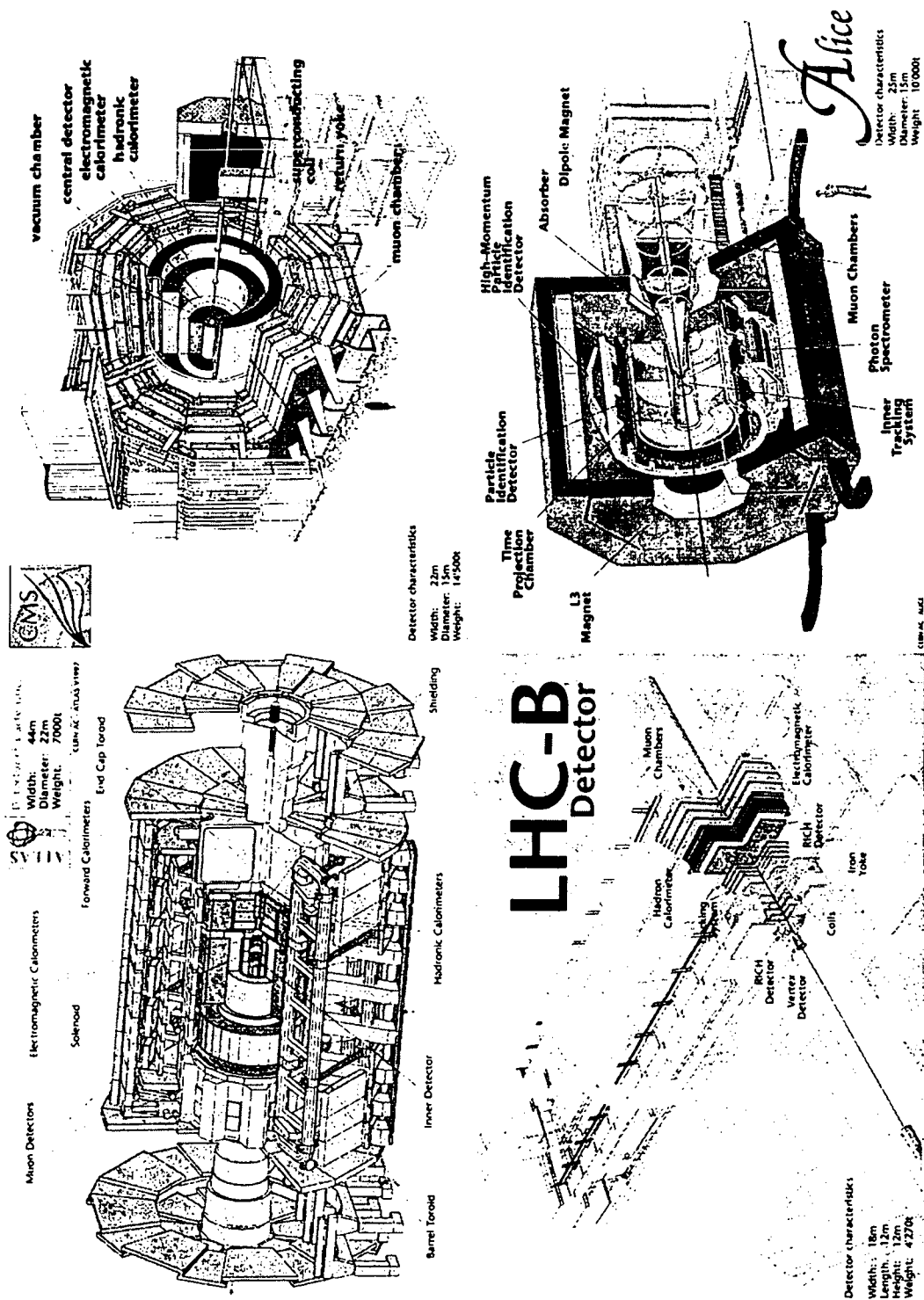
Figure 2.2: Schematic drawings of the four LHC detectors.

- ATLAS (*A Toroidal Lhc ApparatuS*), a general purpose detector for p–p collisions, designed to exploit the full discovery potential of the LHC [7].

- CMS (*Compact Muon Solenoid*), another general purpose detector, designed to detect cleanly the various signatures for new physics by identifying and precisely measuring muons, electrons and photons over a large energy range and at high luminosity [8].

- LHCb, designed to exploit the large number of b-hadrons produced at the LHC in order to make precision studies of CP asymmetries and of rare decays in the B-meson systems [9].

- ALICE (*A Large Ion Collider Experiment*), the only detector of the LHC accelerator fully dedicated to the physics of heavy ion collisions, to establish and to study the phase transition from hadronic matter to deconfined partonic matter, the so called *quark gluon plasma* [10].

The Large Hadron Collider is designed to accelerate protons to an unprecedented energy of 7 TeV. To reach this energy, LHC's main bending magnets, the *main dipoles*, have to provide a nominal magnetic field of about 8.4 T. The current required to create this field is about 11.8 kA and constraints on geometry and heat budget require that the magnet coils are made of superconducting cables (cf. [11, 12]). These cables consist of fine strands (7 μm diameter) of a Nb-Ti alloy which are twisted together and embedded in a copper matrix. Hence, the whole magnet has to be cooled below the critical temperature of the superconductor (the Nb-Ti alloy), which is achieved by means of superfluid helium at 1.9 K. About 80% of the total length of the accelerator will be held at these temperatures, thus making the LHC one of the biggest cryogenic facilities in the world [13].

As shown in figure 2.3, the beam pipes for the two counter-rotating beams, together with a pair of superconducting coils each, are incorporated into a common iron yoke, thereby saving space and cooling power. This assembly, called the *cold mass*, is then cooled to 1.9 K by superfluid helium. The cold mass is insulated from ambient temperature by a surrounding vacuum vessel, the so called *cryostat*.[4] The total length of an assembled dipole is about 16 m and a total number of 1232 of these magnets will be built into the LHC. The smooth operation of the main dipoles is one of the crucial points in the operation of the LHC, since a *quench*, i. e. the transition from superconducting to resistive state, of a single magnet can interrupt machine operation for several hours.

---

[4]For a more detailed description cf. [15, 16, 17, 18]
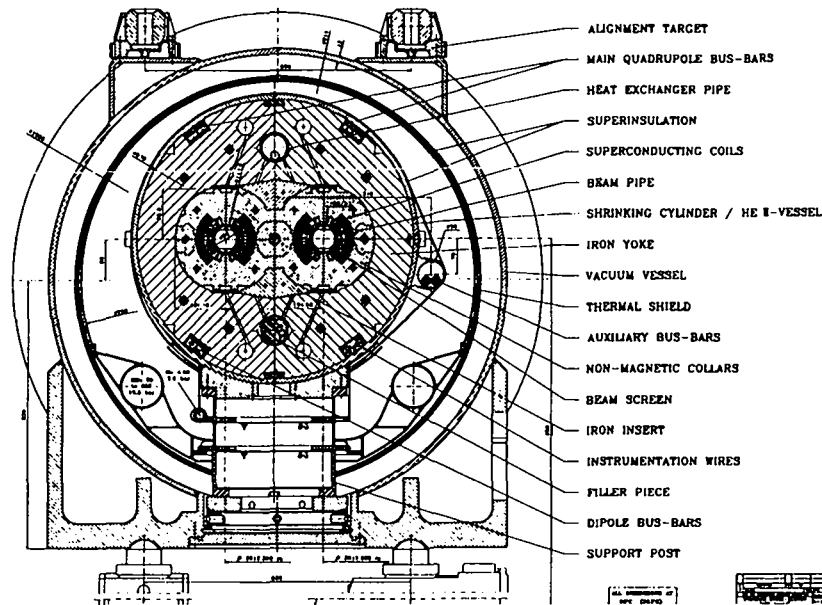
Figure 2.3: Cross section of a LHC dipole cryomagnet assembly (graphic taken from [14].)

2.3 An introduction of the LHC beam vacuum system

As illustrated in figure 2.3, the beam pipes for the two counter-rotating beams (inner diameter 50 mm) are directly built into the inner openings of the magnet (inner diameter 56 mm), thus being in direct contact with the cold mass and acting at the same time as the inner wall of the magnet cryostat (the so called *cold bore*) [14, 19, 20, 21, 22]. This construction implies, that the walls of the beam vacuum system will have the same temperature as the cold mass itself, namely 1.9 K during operation. At this temperature, gases except Helium have a negligible vapor pressure, hence the beam pipe will effectively act as *cryopump* with basically unlimited capacity, making external pumping superfluous during operation [21, 22]. External pumps are required only for the initial pump-down of the vacuum system.

The LHC will be the first superconducting accelerator which is exposed to intense synchrotron radiation. According to [23], the instantaneous power radiated by a charged particle, in this case a proton, traveling on a circular orbit is given by

$$P_{s.r.} = \frac{1}{4\pi\epsilon_0}\frac{2}{3}\frac{e^2}{c^3}\frac{v^4}{r^2}\gamma^4 \qquad\qquad (2.1)$$

where e is charge of the proton (i. e. the elementary charge), c the speed of light in vacuum, v the velocity ($v \approx c$), r the bending radius ($r = 2784.32$ m for the main dipoles) and γ the relativistic factor ($\gamma = 7461$ for 7 TeV protons). Substituting the numerical values into equation 2.1 results in a value for the instantaneous power radiated by one proton of $P_{s.r.} = 1.84 \times 10^{-11}$ W. Having 2835 bunches with 1.05×10^{11} protons per bunch distributed over the circumference of LHC (26658.883 m) results in a average linear proton density of about 1.12×10^{10} m^{-1}, hence the linear heat load caused by synchrotron radiation in the main dipoles is about 0.2 W · m^{-1}.

This heat load, if transferred to the cold mass, would increase excessively the heat dissipated in the superconducting magnets, hence the cold mass has to be shielded against synchrotron radiation. This is achieved by means of the so called *beam screen*, a racetrack shaped tube with two *cooling capillaries* attached to its two flat parts, which actively cool the beam screen to a temperature between 5 K and 20 K by means of pressurized Helium gas (cf. [21]). The beam screen has a diameter of 44 mm and the flat parts are separated by 36 mm. A picture of a prototype beam screen, inserted into a sample beam pipe is shown in figure 2.4.

Another feature of the beam screen is a thin layer of oxygen free high conductivity copper (thickness about 50 μm), which is co-laminated with the base material of the beam screen, a low permeability stainless steel. This layer is intended to carry the beam-induced image currents, thus reducing the machine impedance to an acceptable value. The chosen value for the thickness of the copper layer is in fact a compromise between low impedance and mechanical stability. Eddy currents, induced during a magnet quench are inversely proportional to the impedance. These eddy currents, in conjunction with the magnetic field of the dipole can result in very high Lorentz forces acting on and leading to deformation of the beam screen [24, 25, 26]. Without beam screen the image currents would flow through the beam pipe and produce an unacceptably high resistive heat load on the cold mass, which in turn would lead to a quench of the magnet. In the present configuration the heat load due to the image currents, about 0.1 W · m^{-1} [27, 28], is intercepted by the beam screen.

A third important feature of the beam screen are the pumping slots incorporated in the flat parts of the beam screen, amounting to about 4% of the its total surface. Residual gas molecules can travel through this pumping slots
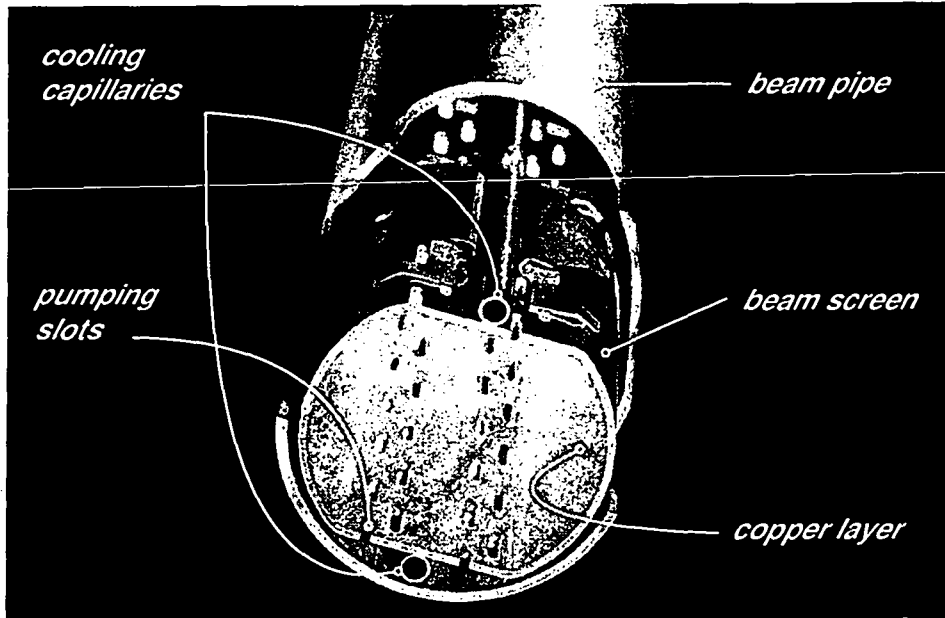
Figure 2.4: Picture of a prototype beam screen, inserted into a sample beam pipe.

and reach the cold bore wall where they will permanently adsorbed [14]. The purpose of the pumping slots will be discussed in more detail in conjunction with the dynamic vacuum effects in the next section.

As a last, nevertheless important point, the beam loss due to nuclear scattering should be mentioned in the context of this introduction. A small fraction of scattered protons escapes from the aperture of the beam pipe and penetrates the surrounding material, thereby producing a shower of secondary particles which is finally absorbed by the cold mass. There is no way that these scattered particles can be absorbed by the beam screen and therefore the machine design includes an allowance of about 0.1 W · m^{-1} for the linear heat load due to nuclear scattering for the two beams [22]. The linear heat load $P_{n.s.}$ (for one beam) can be expressed as

$$P_{n.s.} = \frac{I_{beam}}{e} N_G \sigma_{n.s.;G} E \qquad (2.2)$$

where $I_{beam} \approx 0.536$ A is the (nominal) current of the proton beam, e the

elementary charge [5], N_G the number density of gas G, $\sigma_{n.s.;G}$ the cross section for nuclear scattering of a proton on a molecule of gas G (for Hydrogen molecules and 7 TeV protons, it is $\sigma_{n.s.;H_2} \approx 5 \times 10^{-30}$ m^2 [22]) and E $=$ 7 TeV the proton energy. With the above mentioned numerical values and with $P_{n.s.} < 0.05$ W $\cdot$ m^{-1}, it follows from equation 2.2 that $N_{H_2} \lesssim 2.66 \times 10^{15}$ m^{-3} and in consistency with this requirement an upper limit for the residual number density of Hydrogen molecules of $N_{H_2} = 1 \times 10^{15}$ m^{-3} has been chosen for the design of the beam vacuum system [22]. Assuming a gas temperature of 10 K, the resulting upper limit for the partial pressure of Hydrogen is given as $p_{H_2} = 1.38 \times 10^{-7}$ Pa $\approx 1 \times 10^{-9}$ torr. Corresponding values for other gases can be found in [21] or [22].

2.4 Beam related dynamic vacuum effects and their impact on LHC

2.4.1 Desorption by synchroton radiation

Synchrotron radiation photons hit the inner surface of the beam screen where they either absorbed or scattered, thereby releasing all or part of their energy. In consequence, residual gas molecules adsorbed on this surface can be released into the gas phase, i. e. they are *desorbed*, if the available energy exceeds the energy of the bond between the molecule and surface.

In general, the energy spectrum of the synchrotron radiation, emitted by a charged particle moving on a circular orbit with almost speed of light can be characterized by the so called *critical energy*, given by [23]

$$E_c = \frac{3}{2}\frac{\hbar c}{r}\gamma^3 \tag{2.3}$$

and the number of photons emitted by each beam particle per unit time can be calculated from [23]

$$v_\gamma = \frac{15\sqrt{3}}{8}\frac{P_{s.r.}}{E_c} = \frac{5\sqrt{3}}{6}\frac{\alpha c}{r}\gamma \tag{2.4}$$

where $\hbar$ is the reduced Planck constant, c the speed of light in vacuum, α the fine-structure constant, r the bending radius and γ the relativistic factor. In the case of LHC, it is $E_c \approx 44.1$ eV and $v_\gamma \approx 8.46 \times 10^6$ s^{-1}. With an average

---

[5]In fact, it is $I_{beam}/e = v_p$, i. e. the number of protons passing through an arbitrary cross section of the beam pipe per unit time.

linear proton density of $\mathcal{N}_p \approx 1.12 \times 10^{10}$ m^{-1} an average *linear photon flux* can be calculated as

$$\dot{\mathcal{N}}_\gamma = v_\gamma \mathcal{N}_p \approx 9.45 \times 10^{16} \ s^{-1} \cdot m^{-1}. \tag{2.5}$$

The number of desorbed molecules is proportional to this photon flux, hence

$$\dot{\mathcal{N}}_G = \eta \dot{\mathcal{N}}_\gamma. \tag{2.6}$$

The constant of proportionality η is called the *molecular desorption yield* and is usually given in units of molecule $\cdot$ photon^{-1}. [6] η is in fact not a constant but depends on several factors, among others the nature of the desorbed gas, the surface material, temperature and pre-treatment and the "history" of the surface, i. e. the number of photons the surface has been exposed to.

The phenomenon of desorption by synchrotron radiation, also called *photon stimulated desorption* or *photon induced desorption*, has been subject to extensive studies in the past (c.f. [29, 30] in the context of LEP, [31, 32, 33, 34, 35, 36, 37] in the context of LHC and/or the SSC, the *Superconducting Super Collider*). Values for η at conditions relevant for LHC, given in above cited literature, range from some 10^{-3} molecule $\cdot$ photon^{-1} for H_2 to some 10^{-5} molecule $\cdot$ photon^{-1} for CO_2 and CH_4. After a long exposure of the surface to synchrotron radiation these values are reduced by 1 ... 2 orders of magnitude, an effect which is also called *beam scrubbing*.

In the case of cryogenic vacuum systems, molecules in the gas phase are readily pumped by the cold walls. These molecules are only lightly bound to the surface, i. e. *physisorbed* and they can be re-desorbed by synchrotron radiation with a much higher yield. This process is called the *recycling* of previously physisorbed molecules and the corresponding desorption yield, usually denoted as η', can exceed η by several orders of magnitude (c.f. [32, 36]). Recently, the cracking of adsorbed molecules by synchrotron radiation has been identified as an additional mechanism which can contribute significantly to the gas load in the beam vacuum system [37].

At this point the importance of the pumping slots of the beam screen can be well explained. A fraction of the desorbed and recycled gas molecules can travel through these slots and reach the surface of the cold bore, Since this surface is shielded from synchrotron radiation, these molecules are not recycled and hence can be permanently cryosorbed on the beam pipe. Thus,

---

[6]Nevertheless the physical unit of η is 1.

unlike the inner surface of the beam screen where molecules are continuously recycled, the pumping slots provide the means to remove gas effectively and permanently from the beam vacuum system.

2.4.2 Ion induced pressure instability

Positive ions can be produced in the beam vacuum system through the ionization of residual gas molecules by the beam particles with typical ionization cross sections for 7 TeV protons in the range of 10^{-22} m^2 [38]. These positive ions are then repelled by the positive space charge of the beam and accelerated towards the beam screen where they transfer their kinetic energy onto the surface. In the arcs of the LHC ion energies at impact are typically in the range of several 100 eV [22, 39]. Like with photon stimulated desorption, the number of molecules, desorbed due to the impact of energetic ions, is proportional to the number of incident ions, hence

$$\dot{\mathcal{N}}_G = \eta_i \dot{\mathcal{N}}_+ \qquad (2.7)$$

with $\dot{\mathcal{N}}_G$ being the linear flux of molecules of the species G, desorbed from the beam screen and $\dot{\mathcal{N}}_+$ the linear flux of ions hitting the beam screen. η_i is like before called the *molecular desorption yield* but this time expressed in units of molecule $\cdot$ ion^{-1}. Again, η_i is not a constant. It depends not only of the nature of ions and desorbed molecules, the ion energy, nature and temperature of the surface [40, 41], but also on the surface preparation and condition [42]. In the case of cryogenic vacuum systems, we can again distinguish between tightly bound, chemisorbed molecules and physisorbed molecules. Whereas it is $\eta_i \approx (1 \ldots 10)$ molecule $\cdot$ ion^{-1} in the case of chemisorbed molecules it can by several thousand molecules per ion for physisorbed molecules [43, 44].

If one gas species G is dominant, $\dot{\mathcal{N}}_+$ can be expressed as

$$\dot{\mathcal{N}}_+ = \sigma_{i.;G} N_G \frac{I_{beam}}{e} \qquad (2.8)$$

where $\sigma_{i.;G}$ is the ionization cross section of this species, N_G its number density, I_{beam} the proton beam current and e the elementary charge.

It can be seen from the preceding paragraphs (n. b. equations (2.7) and (2.8)) that the process of ion stimulated desorption in a beam vacuum system

13

is "self-amplifying"[7] and could result in a pressure run-away (or *pressure instability*) if the gas is not pumped away with a sufficient pumping speed. This effect has been observed at the ISR, the *Intersecting Storage Rings*, at CERN (cf. [38]). However, in the cold parts of the LHC the ion induced desorption should not pose any serious problems to the beam vacuum due to the distributed cryo–pumping of the cold walls [22].

2.4.3 Beam induced electron multipacting

Electron multipacting is a phenomenon known from high power radio frequency and microwave cavities where it manifests itself in RF power consumption and break down. It is caused by the synchronous motion of free electrons in an alternating electric field. First free electrons are produced by field emission, photo-electric effect, or ionization of residual gas molecules by cosmic rays. These electrons are accelerated towards the surface of the cavity by the electric field where they, when hitting the surface with sufficient energy, can produce secondary electrons. If the electric field changes its direction at the same time, these secondary electrons are accelerated towards the opposite surface where they in turn produce additional electrons. If the *secondary electron yield*, i. e. the number of secondary electrons produced per incident electron, exceeds unity, the number of electrons which are "bouncing" back and forth is increasing exponentially (also known as the "build up of the *electron cloud*"), finally leading to the break-down of the cavity (cf. [45, 46, 47]). In general, for electron multipacting to develop, the following two condition must be fulfilled [48]:

- the electron must be able to traverse the vacuum chamber in synchronism with the electric field and

- the electron energy at impact must result in an secondary electron yield greater then unity.

Since several years a similar effect has been observed in the beam pipes of high current proton accelerators (cf. [48, 49, 50, 51]). This phenomenon is called *beam induced multipacting* because the alternating electric field is generated by the bunched proton beam. In the case of LHC with its cryogenic vacuum system, the build-up of an electron cloud can have the following implications:

- excessive heat load on the vacuum chamber surfaces (computer simulations give values up to 15 W $\cdot$ m^{-1} [52, 53]),

---

[7]hence an increase of gas density results in an increase of the ion flux which in turn results in an increase of the molecular desorption rate which results in an even faster increase of the gas density ...

- strong pressure rise due to the desorption of adsorbed molecules from the beam screen surface by impact of electrons (*electron stimulated desorption*) and

- coherent oscillations of the proton beam with the electron cloud, leading to emittance growth and luminosity decrease or even beam loss [14].

In the arcs of the LHC, primary electrons are massively created through the photo-electric effect due to the high flux of synchrotron radiation photons. The production rate of photo-electrons per proton (ν_{e-}) is proportional to the production rate of synchrotron radiation photons (ν_γ):

$$\nu_{e-} = 0.45 \nu_\gamma Y. \tag{2.9}$$

Y is the *effective quantum yield*, i. e. the number of photo-electrons produced per incident photon. A value of Y $\approx$ 0.1 is commonly assumed for LHC relevant conditions [54]. Only about 45% of the incident photons have enough energy[8] to produce photo-electrons [53], hence the factor of 0.45 in equation (2.9).

Synchrotron radiation photons emitted by a traveling proton bunch hit the circumference of an arbitrary cross section (normal to the beam axis) of the beam screen at about the same moment as the proton bunch travels through this cross section, hence the instantaneous production rate of photo-electrons varies in synchronism with the bunch structure of the beam [54]. Furthermore, since photons are preferably emitted in the forward tangential direction of the beam orbit, the instantaneous production rate of photo-electrons has also an azimuthal dependency. For a surface material with high reflectivity, photons are likely to be reflected many times before producing a photo-electron, hence the photo-electrons are distributed uniformly over the beam screen surface. On the other hand, if the reflectivity of the surface is low, synchrotron radiation photons are likely to produce photo-electrons at already at their first impact on the surface, hence the photo-electron distribution follows that of the photons. The initial electron distribution has an influence of the development of beam induced multipacting especially in the parts of the accelerator where a strong magnetic field is present, e. g. in the main dipoles.[9]

Photo-electrons receive approximately a "kick-like" acceleration towards the

---

[8]i. e. an energy greater then the work function of copper, about 4 eV [52]

[9]Due to Lorentz forces, electrons are bound to move in spirals around the magnetic field lines.

beam axis by the passing proton bunch, which is proportional to the number of protons in the bunch and hence proportional to the beam current. From the condition for the onset of multipacting - electrons must be able to traverse the beam vacuum from wall to wall before the arrival of the next bunch - a critical beam current can be calculated. For nominal LHC parameters the energy gain during kick acceleration is about 200 eV and the critical beam current for the onset of multipacting is $I_{crit} \approx 0.19$ A [48].

As with the RF related multipacting, the secondary electron yield δ must exceed unity to develop beam induced multipacting. In fact, since some of the secondary electrons can get out of phase with the electron cloud movement and are lost for further multiplication, the critical value of the secondary electron yield $\delta_{crit.}$ is greater than 1. For nominal LHC operating conditions it is $\delta_{crit.} \approx 1.3$ [14].

Because of the critical influence of the secondary electron yield for the development for multipacting and hence for the operation of LHC, this parameter has been the topic of extensive research work carried out in the LHC vacuum group over the last years (cf. [55, 56, 57, 58, 59]). A summery of the main experimental results concerning the secondary electron yield of copper is given in [55], and the curves shown in figure 2.5 show typical examples for these results. The curve denoted as "as received" refers to a surface prepared for installation in the vacuum system, whereas the "fully conditioned" curve refers to a surface with all contaminants stripped off. It can be seen that the maximum secondary electron yield can be reduced significantly by means of proper conditioning of the surface, i. e. during beam operation *beam scrubbing* or by surface conditioning (bake-out, argon glow discharge treatment, ...).

As a last point in this section the desorption of gas molecules by electrons, called *electron stimulated desorption*, should be mentioned. The desorption rate is proportional to the rate of impinging electrons and characterized by the *molecular desorption yield* η_e (given in units molecule $\cdot$ electron^{-1}, cf. sections 2.4.1 and 2.4.2)

$$\dot{\mathcal{N}}_G = \eta_e \dot{\mathcal{N}}_{e^-}.$$ (2.10)

Again, η_e is not a constant but depends on the energy of impinging electrons, the nature of the desorbed gas, the material, temperature, treatment and history of the surface [40, 41, 60, 61, 62].

Due to the electron stimulated desorption, the build-up of an electron cloud
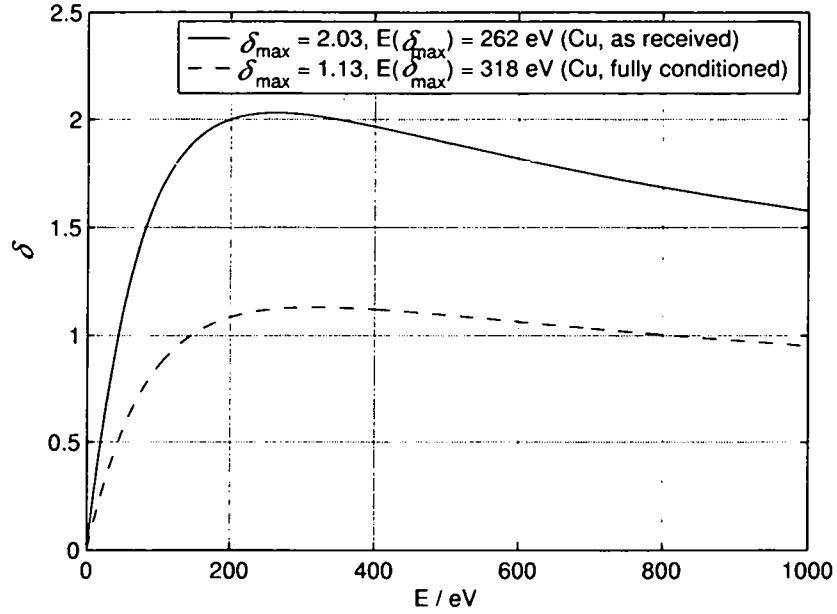
Figure 2.5: Typical plots of the secondary electron yield of copper as a function of the primary electron energy (data taken from [55].)

manifests itself also by a strong increase in the residual gas pressure. In fact, pressure rises up to a factor of 60 could be observed in the SPS[10] during runs with LHC-type beams [50]. Thus, an electron cloud in the beam vacuum system of the LHC would most probably raise the pressure during the conditioning period to an unacceptably high level for the cryogenic system of the LHC.

---

[10]*Super Proton Synchrotron*, one of CERN's accelerators which will be used to pre-accelerate and inject beam particles into the LHC.

Part II

Gases on cryogenic surfaces

In a solid/gas system different interaction mechanism can appear, which
are depending on the experimental conditions. A schematic view of different particles/solid interactions is shown in figure 2.6. One speaks from
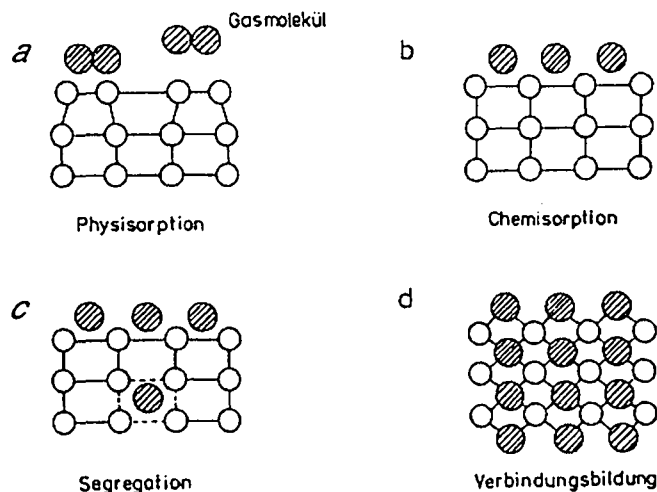
Figure 2.6: Schematic view of different particles/solid-interactions of a 2-atomic molecule. [63])

physisorption at weak interaction of particles with a binding energy less then
50 kJ/mol (0.5 eV/particle). This interaction is a consequence of van-der-Waals-forces between particles and substrate and hence it appears on any
solid-gas-system. Well studied systems of physisorption are for example rare
gases on metals, semiconductors or isolators at low temperatures. Typically
one reaches a complete monolayer-occupancy in the physisorption-layer at
gas pressures, which are in the order of a tenths of the saturated vapour
pressure of these particles. By increasing the gas pressure up to the saturated vapour pressure the particles condense in thick layers on the substrate.
The interaction at physisorption is relatively low, therefore there is almost
no change in the reconstruction of surface atoms. This is indicated in figure
2.6 a. Due to energetic reasons free surface atoms move together in pairs and
they are not changing the distance of each other during physisorption. As
physisorption is the main adsorption process in this work I will describe the
physical basics more in detail later on.

Chemisorption is a strong chemical interaction with interaction energies of
typically more than 50 kJ/mol. An example is schematically displayed in
figure 2.6 b. Here is assumed, that surface reconstruction is repealed due to

19

the strong interaction with the adsorbate. On the one hand chemisorption of molecules can take place molecular and on the other hand chemisorption of molecules can lead to dissociation of these molecules.

The next example in figure 2.6 c shows segregation of particles. These particles are also soluble in the bulk of the solid, whereas in the hatched vicinity of the imbedded atom in the bulk, strong elastic deformations can be occur.

The last shown example in figure 2.6 d illustrates, that at high interaction energy between adsorbed particles and bulk atoms a bonding formation can be occur. Consequence of the shown stoichiometric bonding formation is the formation of new three-dimensional structures with rigorous changed chemical, electronic and magnetic properties not only on the surface.

From thermodynamic considerations follows, that at low temperatures reactions go on preferred where the *total energy* is decreased (e. g. at adsorption), while at high temperatures reactions go on mostly in that direction, where the *total entropy* is increased (e. g. desorption).

Physisorption

In physisorption geometric structure and electronic properties, of free particles and the free surface, remain substantial. Experiments for physisorption require low temperatures, because of the relatively weak interaction. Under these conditions condensation of the particles under formation of liquid or solid three-dimensional phases can occur. If one studies physisorbed particles in the region of monolayers and lower, partial pressure and temperature must be accurately adjusted. If the condensation enthalpy of particles strongly differ from the isosteric heat of physisorption in the region of submonolayers, then one can determine the beginning of condensation from adsorption isotherms as a function of pressure. In this way it is, for example, possible to determine the surface of the substrate from the knowledge of the required space of one molecule (see figure 2.7 or [64]).

The physical reason for physisorption are interactions between adsorbed particles and substrate atoms and it can occur as well in the gas phase between molecules. Thus should be explained at first by free particle forces in the gas phase (a) and afterwards by physisorption forces (b).

a) Two-particle interactions in the gas phase, between chemical not reactive particles are termed in general as van-der-Waals-forces, which can be calculated for example over the perturbation theory 2. mode (e. g. [65]). It is possible to separate the potential energy of two interacting particles in two

20
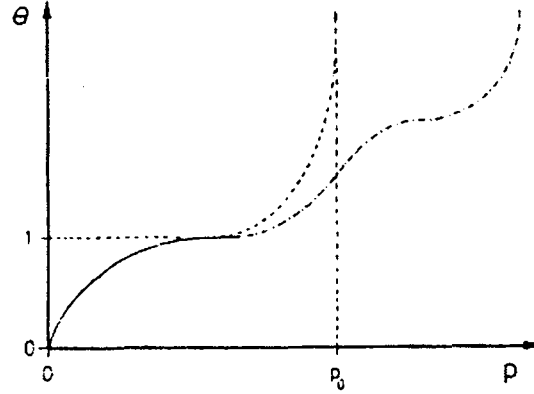
Figure 2.7: BET-isotherm for condensation of the 1. monolayer (dashed). It is also shown the case for condensation after double-layer adsorption (chain dotted line). p_0 is the saturated vapour pressure for condensation on the first monolayer. [63])

distance dependent parts, of an attraction potential E_{attr} and a repulsion potential E_{rep}. The physical reason for the repulsion is the Pauli-principal. The attraction can be described semi-classical as an electrostatic interaction between a temporally static and a temporally fluctuate charge distribution. The former is acquired through multipoles, which characterises a charge distribution in the molecule and cause eloctrostatic multipole-multipole and polarization induced multipole interactions. Thereby it is in general sufficient to take in account only dipole- and quadrupole terms.

The decrease of the total energy of interacting particles as consequence resonant fluctuating charge distributions is known as dispersion-interaction. This interaction has been already derived semi-classical by London 1937 and can be evaluated over polarisabilities and ionisation energies of particles.

Figure 2.8 shows the typical distance progression of a two-particle potential with an attraction- and repulsion term, whereas in general the former can be arranged proportional to r^{-6}. The progression of the repulsion term is not very essential for the calculation of a row of physical properties like, for example real gas corrections or gas viscosity. Therefore one arranges the progression of the repulsion term proportional to r^{-12}. Hence it follows the

21
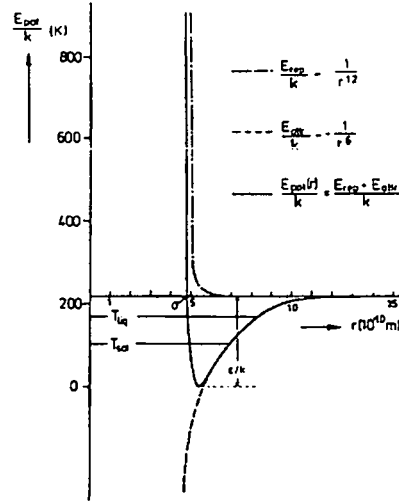
Figure 2.8: Example of a two-particle Lennard-Jones-Potential for description of the interaction of molecules (here ethylene C_2H_4) as a function of the distance r between two molecules. ε is the depth of the potential minimum and σ the effective diameter of the particles. [63])

so-called Lennard-Jones-Potential

$$E_{pot} = 4\varepsilon \left[\left(\frac{\sigma}{r} \right)^{12} - \left(\frac{\sigma}{r} \right)^{6} \right] = E_{rep}(r) + E_{attr}(r), \qquad (2.11)$$

where ε and σ have the meaning shown in figure 2.8. Therein σ is equivalent to the diameter of the particle (more precisely: distance of the particles at the interaction energy $\varepsilon = 0$) and $-\varepsilon$ is the depth of the potential minimum.

With E/k as temperature one can read from the example in figure 2.8 how much is the thermal energy kT at given temperature in comparison to the interaction energy between two ethylene molecules. For demonstration there is also given the temperature of liquefaction T_{liq} and solidification T_{sol} at 10^5 Pa.

On closer examination on the interaction between two particles one must take into account the statistically averaged overall orientations of the particles relative to each other and in general as well angular dependent interaction potentials. Since this is difficult, one often uses the simplified assumption of rotation-symmetric potentials, whose characteristic effective parameter is available from experimental data (e. g. from real gas behaviour or gas vis-

cosity), which are tabled.

b) At physisorption an adsorbed particle (1) gets in interaction with several particles (2) of the substrate. This interaction can be evaluated e. g. through summation over all two-particle interactions from appropriate two-particle potentials. Thus, one can be calculated from respective Lennard-Jones parameters of the interaction of same particles amongst each other and from parameters for the effective interaction of two different particles over $\sigma_{eff} = (\sigma_1 + \sigma_2)/2$ and $\varepsilon_{eff} = \sqrt{\varepsilon_1 \cdot \varepsilon_2}$. In order, one is able to determine the energy of physisorption under consideration of all distances $r_{1,i}$ between adsorbed particle 1 and substrate atoms i over a summation of all fractions of the attractive interaction $E_{attr,i}$ and the repulsive interaction $E_{rep,i}$

$$E_{pot,phys} = \sum_i (E_{attr,i} + E_{rep,i}) = \sum_i 4\varepsilon_{eff} \left[\left(\frac{\sigma_{eff}}{r_{1,i}} \right)^{12} - \left(\frac{\sigma_{eff}}{r_{1,i}} \right)^6 \right]. \quad (2.12)$$

This method implies the additivity of pair interactions and negligible interaction of particles amongst each other. In particular at higher coverages it is more sophisticated, under the consideration of interaction of physisorbed particles amongst each other.

Free electrons in metals show contributions to interaction which cannot be related to single atoms on well defined places. At heteropolar solid compounds one has to take into account position dependent electric fields and polarisabilities. Adsorbing molecules with permanent multipole-moment effects of influence, appear also in non-metallic solids. Further details are described in [64].

The interaction energy of physisorbed particles can be dependent from their orientation relative to the substrate. This effect can be explained quantitative in this way, that the force action of the adsorbing molecule is not rotation-symmetric through the indication of only one centre, but angular dependent over more centres with rotation-symmetric interaction. The observed experimental interaction energy results from the statistically weighted terms for different orientations of the particle relative to the substrate. This statistic average determination of the energy is strongly temperature dependent. Low temperatures cause the freezing of degrees of freedom of motion of the molecule relative to the substrate till to two-dimensional condensation of physisorbed particles in the potential minimum of these particles on the substrate.

The executions show that as result of the energetic heterogeneity of different places of adsorption and a result of the interaction of physisorbed parti-

23

cles amongst each other, in general, one has to take a coverage dependent energy distribution $f(E_{pot})$ to describe the energetic of adsorbed particles. Experimentally one can find the energetic heterogeneity over the width of the thermic spectrum of desorption in comparison to the ideal width minimum at monoenergetic ad- and desorption like in figure 2.9. The dashed
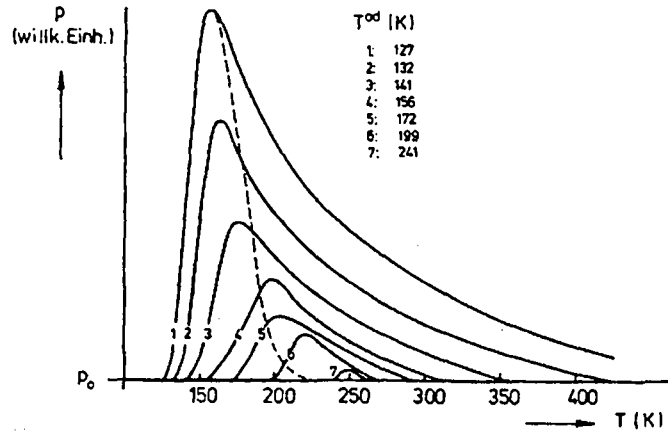
Figure 2.9: Typical thermal spectra of desorption for physisorbed oxygen on $ZnO(10\bar{1}0)$, recorded under conditions of molecular flow. Desorption starts at different temperatures T^{ad} and respectively same starting pressures p_0. The dashed line points the expected TDS-spectrum at desorption from an adsorption condition, which is charcterised through an only well defined energy- and entropy value at $T^{ad} = 127$ K [66]. [63])

line corresponds to an expected TDS-spectrum at a well defined desorption energy. For interpretation of experimental spectra one assumes for example that the occupation of a specified place of adsorption with energy E can be described over a Langmuir-isotherm. The function $f(E_{pot})$ determines the statistic distribution of places and therefore the TDS-spectrum over the statistic-thermodynamic average determination and the experimental evaluated isotherm ([66]). Independently therefore one can get as well the energetic homogeneity from the experimentally evaluated adsorption isotherm.

Over the adsorption isotherms one can get isosteric heats Q_{ads} as a function of the coverage. Hence one gets specific heats of the adsorption complex and over statistic mechanic movement conditions of adsorbed particles.

Chapter 3

Models for sticking probability and electron stimulated desorption

3.1 Sticking probability

When particles from the gas phase hit a solid surface, they will adsorbed or reflected. Rates of adsorption are in general characterised over the sticking coefficient S, which is defined as the ratio between the hits of particles which lead to an adsorption complex and the total amount of hits. Sticking coefficients can be calculated from the experimentally evaluated adsorption rates at constant temperature

$$R_{ads} = \frac{dN_{(s)}^{ad}}{dt} = SZ_{(s)} = S\frac{p}{\sqrt{2\pi mkT}} \tag{3.1}$$

with $Z_{(s)} = p/\sqrt{2\pi mkT}$ as collision factor over the partial pressure p, mass m and temperature T ([67]).

Even if particles will reflected after collision, they will change in general their temperature, the amount of the momentum and their energy through interaction with the surface. These changes can be expressed quantitative over temperature-, momentum- or energy accommodation coefficients $\alpha_T, \alpha_p, \alpha_E$. For example in that way, that the temperature accommodation coefficient α_T is defined over the temperature difference of the particles in the gas phase before and after the collision $T_{(bef)}^g - T_{(aft)}^g$, divided through the maximal possible temperature difference $T_{(bef)}^g - T^S$ with T^S as surface temperature.

It is:

$$\alpha_T = \frac{T^g_{(bef)} - T^g_{(aft)}}{T^g_{(bef)} - T^S} \qquad (3.2)$$

Even though scattered particles have not a Maxwell-Boltzmann-distribution a temperature for characterisation over an appropriate average will be chosen. α_p and α_E are defined analogues.

In a more sophisticated handling, one can define and handle for example momentum-accommodation coefficients corresponding on the x-, y- resp. z-component of the momentum. Energy-accommodation coefficients can be defined for the exchange of energy in well defined oscillation-, rotation- and translation degrees of freedom ([68]).

The sticking coefficient established in equation 3.1 is also on chemical clean surfaces strongly dependent from their geometrical structure, e. g. from concentration of angle- or edge atoms on the surface ([69]). Furthermore one founds in general a strong dependence of the sticking coefficient from coverage of adsorbed particles and temperature. This will be expressed over the formal approach of

$$S = \sigma \cdot f(\Theta) \cdot \exp\left(-\frac{E_{A,ads}}{RT}\right) \qquad (3.3)$$

with the sticking probability σ, with one normalised part of free places of adsorption on the surface $f(\Theta)$ and with the activation energy per mole $E_{A,ads}$. In simple cases $f(\Theta)$ can be calculated. At non-dissociative adsorption under the assumption that $\Theta = 1$ the maximum degree of coverage of adsorbed particles on the surface is

$$f(\Theta) = 1 - \Theta. \qquad (3.4)$$

In case that adsorbed particles under dissociation occupy two surface places, one get

$$f(\Theta) = (1 - \Theta)^2. \qquad (3.5)$$

Further details are in [70] and [71].

3.1.1   Influence of coverage

A physical comprehension of the occurrence of certain values of the sticking coefficient at certain solid/gas systems can be derived from the *Eyring-Theory of the transition state* (e. g. [64], [70], [72]). Accordingly one assumes that the adsorption runs over an activation barrier, like in figure 3.1. The rate of

Figure 3.1: Potential diagram for the reaction of molecules with solid surfaces along the coordinates of reaction RK. There are also drawn parabolic potential curves and zero point energies ε_0 of oscillations, which remain in the active complex and results from bends of the energy-hyper surface. The activated complex is lying on the saddle point, i. e. a potential minimum except for the direction of the coordinate of reaction. [63])

adsorption is given over

$$R_{ads} = \nu^{\neq} N_{(s)}^{ad\neq}. \tag{3.6}$$

Here means $\nu^{\neq}$ a characteristic decay-frequency of the activated complex at a surface concentration of $N_{(s)}^{ad\neq}$. It is assumed there is a thermodynamic equilibrium between the activated complex and the particles in the gas phase, i. e. the concentration of particles in the activated complex $N_{(s)}^{ad\neq}$ and in the gas phase $N_{(v)}^{g}$ and for the concentration on free adsorption places $N_{(s)}^{SF}$ is given through

$$K_c^{\neq} = \exp\left(-\frac{\Delta G^{0\neq}}{RT}\right) = \frac{N_{(s)}^{ad\neq}}{N_{(v)}^{g} \cdot N_{(s)}^{SF}} = \frac{z_{(s)}^{\neq}}{z_{(v)}^{g} \cdot z_{(s)}^{SF}}$$

$$= \frac{z^{\neq}}{z_{(v)}^{g} \cdot z^{SF}} = \frac{z_0^{\neq}}{z_{0(v)}^{g} \cdot z_0^{SF}} \cdot \exp\left(-\frac{\Delta \varepsilon_0^{\neq}}{kT}\right). \tag{3.7}$$

Thereby the equilibrium constant $K_c^{\neq}$ will be expressed over changes in the molar Gibbs energy $\Delta G^{0\neq}$ between gas and activated complex resp. over one-particle partition functions z, where in the transfer from z to z_0 the terms of the zero point energy ε_0 have been separated. Equation 3.7 is valid at energetic equivalent adsorption places and at heterogenous surfaces. One

has to understand $z_0^{\neq}$, z_0^{SF} and $\Delta\varepsilon_0^{\neq}$ as weighted averages over all centres of adsorption.

According to the theory of the transfer condition the activated complex has to be decayed already at the first oscillation. One separates now the sum of partition $z_0^{\neq}$ in $z_{vib}^{\neq}$, the part-sum of partition of this oscillation degree of freedom and $z_{0,eff}^{\neq}$ the sum of partition of all other degrees of freedom:

$$z_0^{\neq} = z_{0,eff}^{\neq} \cdot z_{vib}^{\neq} \tag{3.8}$$

As the force constant of the reactive oscillation is very low, one can write the limiting value for $z_{vib}^{\neq}$ as

$$z_{vib}^{\neq} = \frac{kT}{h\nu^{\neq}} \tag{3.9}$$

So that:

$$R_{ads} = N_{(v)}^g \cdot N_{(s)}^{SF} \cdot \frac{kT}{h} \cdot \frac{z_{0,eff}^{\neq}}{z_{0(v)}^g \cdot z_0^{SF}} \cdot \exp\left(-\frac{\Delta\varepsilon_0^{\neq}}{kT}\right) \tag{3.10}$$

Here is $\Delta\varepsilon_0^{\neq}$ the difference of the zero point energy between gas phase and activated complex, added up over all degrees of freedom with the exception of the movement along the coordinate of reaction, with is in difference to equation 3.7. This expression can be simplified through the assumption of ideal gas conditions ($N_{(v)}^g = p/kT$), $z_0^{SF} \approx 1$ due to the predominant contribution of relatively high oscillation frequencies to the sum of partition, due to the separation of the translation sum of partition in $z_{0(v)}^g = \frac{1}{V} \cdot \frac{(2\pi mkT)^{3/2}}{h^3} \cdot V \cdot z_{0,vib+rot}^g$ and due to the approach $N_{(s)}^{SF} = f(\Theta) \cdot N_{(s)tot}^{SF}$ as total amount of occupied and unoccupied adsorption places per unit area. Hence it follows from equation 3.10:

$$R_{ads} = \frac{p}{kT} \cdot N_{(s)tot}^{SF} \cdot f(\Theta) \cdot \frac{kT}{h} \cdot \frac{h^3 z_{0,eff}^{\neq}}{(2\pi mkT)^{2/3} \cdot z_{0,vib+rot}^g} \cdot \exp\left(-\frac{\Delta\varepsilon_0^{\neq}}{kT}\right)$$

$$= \frac{p}{\sqrt{2\pi mkT}} \cdot N_{(s)tot}^{SF} \cdot f(\Theta) \cdot \frac{h^2 z_{0,eff}^{\neq}}{(2\pi mkT) \cdot z_{0,vib+rot}^g} \cdot \exp\left(-\frac{\Delta\varepsilon_0^{\neq}}{kT}\right) \tag{3.11}$$

In comparison with equation 3.1 and 3.3 it follows for the activation energy

$$E_{A,ads} = N_L \cdot \varepsilon_0 \tag{3.12}$$

28

and for the sticking probability

$$\sigma = \frac{z_{0,eff}^{\neq}}{z_{0(s),trans} \cdot z_{0,vib+rot}^{g}} \cdot N_{(s)tot}^{SF}. \tag{3.13}$$

The term $z_{0(s),trans}$ is the on the area related sum of partition of the two-dimensional translation, the value $z_{0,vib+rot}^{g}$ is the oscillation- and rotation-sum of partition of the particles in the gas phase. The sticking probability is after this simple model representation at given activation energy the higher, the greater the sum of partition in the activated complex is, in comparison to the molecule in the gas phase.

In an analogues manner one can derive terms of σ for mobile activated adsorption complexes or adsorption with dissociation ([70]).

The easiest way to do a comparison with experimental data is with the start-sticking coefficient S_0, which is measured at negligible coverage because in this case $f(\Theta) = 1$ (equation 3.4 and 3.5). But under these experimental conditions the influence from not ideal surface positions of the mono-crystal is the strongest, so that an accurate determination of experimental data on ideal surfaces and in particular on surfaces of semiconductors is not easy.

Concluding one confined comment has to be done. The fundamental assumption of the Eyring-Theory of the transition state is the thermodynamic equilibrium between ground state and activated complex. This condition is fulfilled for $E_{A,ads} \gg RT$, because in this case from the statistical point of view is only a small, fast delivering part of the total particles in the activated state. But if in the other extreme the activation energy is zero, one cannot use the Eyring-Theory. Therfore one can well interpret in the scope of this theory sticking probabilities σ in the order of one (namely for $E_{A,ads} \gg RT$) but not sticking coefficients $S \approx 1$. In the last case the sticking probability is determined by the time dependency of the energy relaxation between the hitting particle and the substrate. This boarder case is not considered in the Eyring-view.

3.2 Electron stimulated desorption

When considering collisions between an incident low-energy particle ($E_i \approx 500$ eV) of mass m and a free particle of mass M, one can estimate the order of magnitude of the maximum energy transferred (ΔE) during the process with classical kinematics. For hard–sphere scattering the elementary result is [73]

$$\Delta E/E_i = (2mM)(1 - \cos\Theta)/(m + M)^2, \tag{3.14}$$

where Θ is the scattering angle in the center of mass frame of reference. One can see that for $m \ll M$, corresponding to electrons impinging on atoms or molecules, eq. 3.14 reduces to

$$\Delta E/E_i \approx 2m/M, \qquad (3.15)$$

where the expression is averaged over the interval $0 \leq \Theta \leq \pi$. So the fractional energy transfer is of order of $2/1840 \approx 0.001$ for electron-atomic hydrogen collisions, implying that less than 0.5 eV would be partitioned to the H atom in this case. However, ESD experiments often observe desorbing molecules, ions and molecular fragments with mass greater than 1 amu and with kinetic energies in the range from 2–10 eV. This indicates that direct momentum transfer is not usually dominant in electron-adsorbate collisions and that electronic energy transfer must be considered. In addition, strong chemisorption bond energies of 1–8 eV are common in many systems of interest, so that normally one treats desorption induced by slow electrons in terms of electronic excitation mechanisms. Physisorbed species are usually more weakly bound, so this simple assumption about direct momentum exchange may not be as well justified for such cases.

Another general conclusion that one may draw from observations of ESD phenomena is that electron–adsorbate scattering is an isolated event. This comes from comparing the typical average current flux density impinging on the substrate ($\sim 1 \ \mu\text{A/cm}^2 \approx 10^{13}$ electrons/cm$^2 \cdot$ s) to the nominal surface coverage of adsorbed species ($\sim 10^{15}$ /cm^2). Using these values, one sees that the probability of an adparticle interacting simultaneously with more than one primary electron is small. These preliminary considerations set the stage for a description of ESD events in terms of isolated electron-adsorbate interactions where electronic energy transfer plays the predominant role.

3.2.1 Influence of coverage and energy

For a large variety of solids electronic excitations caused by bombardment with photons, electrons, and fast light ions induce the desorption of particles. The elementary steps of these DIET (desorption induced by electronic transitions) reactions are (1) the primary electronic excitation, (2) the evolution of this electronic excitation including its modification by Auger processes, propagation through the solid, and localization, (3) the competition between the decay of the excitation and the acceleration of nuclei, and finally (4) secondary phenomena like sputtering of surrounding ground-state material by the fast particles originating from step (3). Films of rare gases on metallic substrates have been widely used as model systems for the investigation of

DIET from weakly bound solids. Several theories have been developed for the description of the microscopic details of the DIET process for monolayers as well for multilayers of rare gases on metals; these will be sketched in the following.

For *monolayers*, one established approach is the so-called Antoniewicz mechanism [74]. For physisorbed species, the basic steps are the primary ionization of an adparticle, its acceleration towards the surface, neutralization close to the surface, and desorption , if the sum of its potential and kinetic energies exceed a critical value [75], [76]. Different descriptions have been given of the real and imaginary parts of the potential for the ionic state which govern the movement to the surface, and the neutralization, respectively [76]. Another, purely quantal approach explains DIET from rare-gas monolayers on metals as due to the squeezing of the wave packet representing the adparticle by the electronically stimulated initiation strong interactions with the surface [77]; here, the nuclear acceleration is a consequence of the uncertainty principle [77].

The Antoniewicz model for ESD

In 1980 [74], Antoniewicz proposed a modification of the original MGR model which has thus far been successful in describing ESD from physisorbed layers [75]. Antoniewicz considered an adsorbate which, by interaction with an incident electron, becomes instantaneously positively ionized (with respect to time scales of nuclear motion). The ion experiences a screened image charge potential, which attracts it toward the surface. Pauli repulsion is also diminished for the ion (as compared to the neutral) since it has a smaller atomic radius. These two effects allow the ion to move very close to the surface, which in turn dramatically increases the probability of resonant tunneling or Auger neutralization by substrate electrons. Upon reneutralization, the image potential vanishes, leaving only the Pauli repulsion. The reneutralized species, still moving toward the surface, is repelled, effectively bouncing off the substrate to escape as a desorbing neutral particle. Fig. 3.2 illustrates this proposed sequence leading to neutral particle desorption.

Antoniewicz also proposed a more complex two–electron process to explain the desorption of positive ions. This is illustrated in fig. 3.3, where the ground–state configuration (M + A) is promoted to an excited ionic curve (M + A$^+$)*. Again the excited ion moves toward the surface, where tunneling neutralizes the ion, placing the system high on the ground–state (M + A) curve. Pauli repulsion, which suddenly dominates at very small separations, will deflect the hot neutral from the substrate, causing it to escape. Since
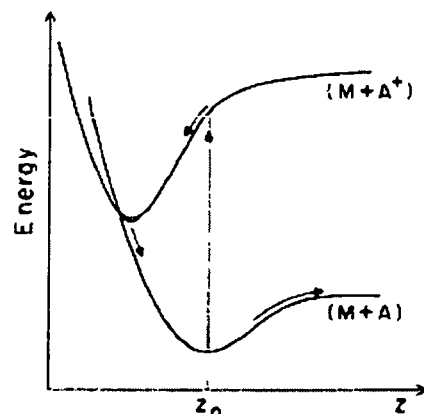
Figure 3.2: Illustrative representation of the Antoniewicz picture of neutral-particle desorption. The ground state (M + A) is excited to an ionic (M + A$^+$) state by a vertical FC transition. Nuclear motion toward the substrate ensues until electron tunneling reneutralizes the ion, which then escapes the surface along a neutral-particle curve. [78]
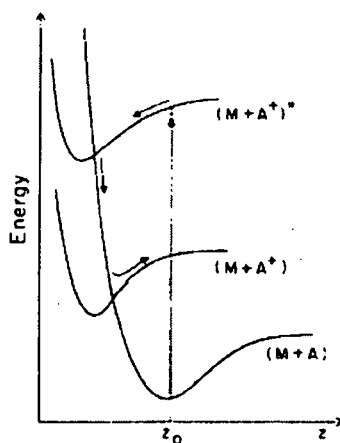
Figure 3.3: Schematic diagram of potential–energy curves in the two–electron Antoniewicz picture. Initial excitation to an excited ionic state (M + A$^+$)* is followed by nuclear motion toward the substrate. Tunneling places the ion high on the ground state (M + A) curve, and a second tunneling process results in ionic desorption along the (M + A$^+$) curve. [78]

the probability of electron hopping processes at short distances is finite, the neutral species may be reionized by resonant electron tunneling into the substrate during its escape, yielding ionic desorbing species, as shown by a curve crossing with the $(M + A^+)$ curve.

Gortel and colleagues have developed rigorous classical and quantum mechanical models for ESD of physisorbed species from surfaces [75, 79] which follow the ideas of Antoniewicz [74]. The classical model assumes a van der Waals attractive potential $(\sim -1/z^3)$ for the neutral adsorbate and adds an attractive image potential $(\sim -1/z)$ upon ionization. Thus the equilibrium position is closer to the surface for the ion than for the neutral, causing nuclear motion initially toward the surface after ionization. Thermal averaging is taken into account since at finite temperatures the neutral adsorbate (before being ionized) has vibrational energy. Thus at the instant of ionization the particle may have a velocity component toward or away from the surface, and a position somewhat greater than or less than z_0. Dissipative forces which draw energy from the moving particle are also incorporated, reflecting the possibility of coupling of the excited particle to substrate phonons or the creation of electron–hole pairs.

Walkup and co–workers [76] provided further analysis of the Antoniewicz motion of noble–gas ions near a metal surface. Using local density functional calculations, the authors predict that the attractive force on a positive ion is substantially less than one would calculate using standard image potential methods. The actual electron charge density distribution at the surface is polarized by the ion and moves (with respect to the plane of the surface) as the ion moves. As the ion approaches the substrate, this image-like surface charge density is repelled by the electron cloud of the ion (Pauli repulsion), pushing the substrate charge density and thus the effective image plane in a negative z direction. Therefore, the "actual" ion–image distance is larger than one would intuitively assume, leading to a reduction in the attractive forces as compared to those calculated using a static image plane model. Fig. 3.4 illustrates this point in simple terms. This phenomenon, when incorporated into calculations of desorption cross–sections, seems to improve the agreement between theory and experiment.

DIET from rare-gas *multilayers* or rare-gas solids (RGS's) was shown to be mainly caused by the excitation of excitons, their diffusion to, and their localization near the surface [80], [81]. Experimentally, excitons can selectively be excited by photons [82]. For electronic simulation with fast ions or electrons, ionization is the prevailing primary excitation. Excitons are then created in secondary steps via electron-hole recombination processes [80].

33
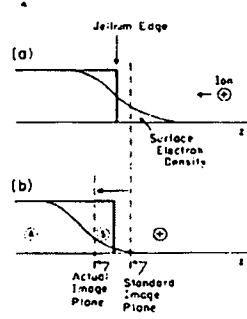
Figure 3.4: Schematic illustration of the shift of the effective image plane of a jellium metal as a positive ion approaches from the vacuum. In (a), the ion polarizes the surface electron density, creating an image–like attractive potential. In (b) the ion is sufficiently close that its electron density presses against that of the surface (Pauli repulsion), pushing the standard image plane position to its actual position. The image charge would appear to be located at S if this phenomenon did not occur, but actually "resides" at A. [78]

The desorption of particles is the consequence of the relaxation processes in the solid before, and after the decay of the localized electronic excitation. For atomic self-trapped excitons all near neighbours of the excited atom are symmetrically displaced [82]. If the exciton is localized at the surface, this electronically excited atom is instantaneously repelled into the vacuum by the forces resulting from its asymmetrical environment [81], [83].

One approximates the distribution of electronic excitations by a Gaussian density for an electron of primary energy E:

$$n^*(r) = (fE/W)G(x)\delta(y)\delta(z), \qquad (3.16)$$

where

$$G(x) = (2\pi\sigma_D^2)^{-1/2}\exp[-(x-r_D)^2/(2\sigma_D^2)]. \qquad (3.17)$$

fE/W is the number of excitations produced by the primary, x the initial thickness and $r_D(E)$ and $\sigma_D(E)$ the mean range and standard deviation of the distribution. The latter two quantities are determined by the atomic number of the target. As a good approximation both quantities may be regarded as proportional to the range. The reason for this is that the distribution of electronically deposited energy is very intensive to variations of the primary energy, once the distribution is depicted in units of the stopping

power $NS_e(E)$ versus the range $R_e(E)$ (cf. Ref. [84]). Then the yield for an infinitely thick film becomes

$$Y = \frac{1}{2}(f_e f E/W) \exp(\sigma_D^2/2l_0^2 - r_D/l_0) \times \text{erfc}[\sigma_D/(\sqrt{2}l_0) - r_D/(\sqrt{2}\sigma_D)], \quad (3.18)$$

where f_e indicates the average number of *ejected* atoms per deexcited molecule or atom at the surface, erfc is the complementary error function and l_0 the diffusion length.

One notes that the ratios σ_D/l_0 and r_D/l_0 enter as arguments for the exponential function. For a fixed l_0 it means as expected that a broad distribution or a small mean range will lead to a large yield.

This relatively simple approach for large film thicknesses is unsuitable for small thicknesses, for which two modifications become necessary. The first important point is the additional boundary condition for an interface in the plane $x = d$, similar to the case of constant excitation density. If the atomic numbers of condensed–gas film and the substrate are similar, the distribution of deposited energy becomes only slightly distorted relative to the distribution in a bulk film. Then, the Gaussian distribution 3.16, 3.17 is still appropriate and the yield becomes [85]

$$Y = (ff_eE/W)\left(\int_0^d G(x)\exp(-x/l_0)dx - \exp(-d/l_0)[\sinh(d/l_0)]^{-1} \times \int_0^d G(x)\sinh(x/l_0)dx\right). \quad (3.19)$$

For the case of thin films on a widely different substrate one has to use a completely different estimate for the excitation density in the film. One ignores the slowing down of primaries in the film and let $r(E_0)\cos\Theta_0 dE_0 d\cos\Theta_0$ be the number of electrons reflected from the substrate with energy E_0 and polar angle Θ_0 per primary. In this approximation one has utilized the knowledge that the reflected electrons exhibit a cosine distribution [86]. The total energy deposited by the primary and the backscattered electrons in the film becomes

$$d\left(NS_e(E) + \int_0^E r(E_0)NS_e(E_0)dE_0\right). \quad (3.20)$$

The first term in the large parentheses is the energy loss of the primary and in the integral every reflected electron contributes with the energy $dNS_e(E_0)/\cos\Theta_0$. Then, one obtains, for the total yield,

$$Y = (\dot{f}f_e/W)\left(NS_e(E) + \int_0^E r(E_0)NS_e(E_0)dE_0\right) \times l_0\tanh(d/2l_0). \quad (3.21)$$

For small thicknesses the yield increases with increasing film thickness d and one notes that the yield for very thin films $(d/l_0 \ll 1)$ is independent of the

diffusion length l_0. For larger thicknesses the excitation density increases considerably as a result of the slowing down and scattering of the primaries.

Sputtering of insulators may be characterized as knock–on sputtering (collisional sputtering) or electronic sputtering. Knock–on sputtering is very well known from ion bombardment of metals. It may be described as a sequence of events, in which target particles are set in motion, from the first collision between the primary and a target atom up to an eventual particle ejection as the result of collisions between slow target particles (fig. 3.5). The main

KNOCK - ON SPUTTERING

ELECTRONIC SPUTTERING

Vacuum   Surface   Solid

o   Target particle
o--Moving target particle
ᴐ   Electronically excited particle
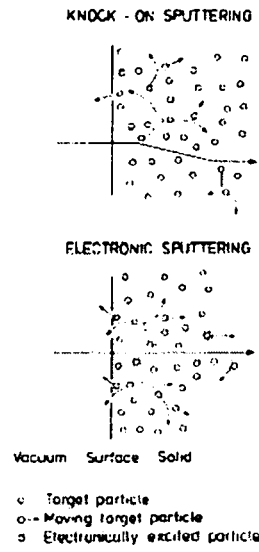
Figure 3.5: Schematic survey of knock-on sputtering and electronic sputtering. The cases shown represent low excitation (collisional) densities. [87]

features of knock–on sputtering for sufficiently small energy densities are well predicted by the linear collision–cascade theory [88, 89]. The backsputtering yield Y from a plane surface is given by

$$Y = \Lambda F_D(E, 0), \tag{3.22}$$

where $F_D(E, x)$ is the spatial distribution of energy deposited into nuclear collisions by the primary of initial energy E. The constant $\Lambda = 3/(4\pi^2 N C_0 U_0)$ depends only on the properties of the target material, the sublimation energy U_0 and the atomic density N. The surface value of the deposited energy ($x = 0$) is often expressed by the nuclear stopping power $N S_n(E)$ for the primary particle and a dimensionless parameter α:

$$F_D(E, 0) = \alpha N S_n(E). \tag{3.23}$$

36

α is a function of the mass ratio of the beam and target atom mass, and a slowly varying function of the energy. (One considers here and in the following only perpendicular incidence.) The energy distribution of the sputtered particles, which explicitly enters into the evaluation of Λ, is determined by

$$dY/dE_1 = k_s E_1/(E_1 + U_0)^3, \qquad (3.24)$$

where k, is a constant (see ref. [89]) and E, the energy of the emitted particle. For large energies the energy distribution exhibits the well–known E_1^{-2}–tail, and for small energies a maximum at $E_1 = U_0/2$.

Knock–on sputtering is important for the energy regime in which nuclear stopping is dominant. For many combinations, where the contribution of fast recoils to the electronic sputtering is very small is significant, a convenient starting point is the deposition of the total energy E of the primary into nuclear collisions or electronic excitations:

$$E = \int F_D(E,x)dx + \int D_e(E,x)dx = \nu(E) + \eta(E). \qquad (3.25)$$

D_e is the spatial distribution of energy deposited in electronic excitations. ν and η are consequently, the energy which ultimately ends up in atomic motion or electronic excitations, respectively [90]. In eq. 3.25, ν *represents the energy which is available for knock-on sputtering, and η the energy for electronic sputtering*. For keV electron bombardment ν is negligible and, therefore, the sputtering is purely electronic.

In the model by Ellegaard et al. [91] the electronic sputtering yield Y is determined by an expression in analogy, to eq. 3.22:

$$Y = \frac{1}{2}\Lambda D_e(E,0)(E_s/W). \qquad (3.26)$$

E_s is the nonradiative energy release from electronic deexcitations, and W the energy required to make an electron–hole pair. Consider then how this sputtering takes place (fig. 3.5). As a result of the slowing–down of the primary particle atoms or molecules are ionized or electronically excited. When these excitations deexcite, e. g., by dissociative recombination, the liberated energy E, may be sufficient to initiate a low–energy cascade. Since these non–radiative transitions are completely isotropically distributed (as indicated in fig. 3.5) in contrast to the knock–on case, one arrives at the factor $\frac{1}{2}$ in eq. 3.26 [91]. The formula is based on the assumption that the energy E_s is released (in a single event) per electron–hole pair, but extensions of eq. 3.26 are straightforward.

Eq. 3.26 is very similar to the expression indicated by Brown et al. [92] and Garrison et al. [93]. (These authors do not include the isotropy factor 1/2 and utilize a different material constant [92, 91]). Eq. 3.22 and 3.26 now enable to estimate the efficiency of the sputtering, i. e. how well is the energy deposition F_D or D_e exploited for the production of sputtered particles? Electronic sputtering is clearly a factor of $\frac{1}{2}(E_s/W)$ less efficient than knock–on sputtering.

The simple formula 3.26 is inapplicable to materials with mobile excitations, for example, as solid rare gases, but extensions of the formula are available [94]. Generally, for the heteronuclear molecules the energy–releasing processes as well as the value of E_s are not systematically known.

The main reason for the occurrence of this particular type of sputtering is the existence of repulsive states, from which kinetic energy for the ejection process is available. However, this means that the energy conversion strongly depends on the specific material, and that one cannot expect to find a single "universal" mechanism for the electronic sputtering. For metals the beam-induced electronic excitations do not generate any repulsive states for the atoms because of the fast relaxation of the free electrons. Consequently, electronic sputtering does not take place from particle–bombarded metals.

The considerations on collision–cascade sputtering in this section apply to cases in which the energy deposition by the primary particle is relatively small. For high excitation densities one reaches the elastic spike regime for knock–on sputtering [89, 95, 96, 97, 98] and an ionization spike regime for electronic sputtering. These regimes are characterized by the creation of dense cascades, in which the moving particles have a large probability of striking other target particles that already have been set in motion.

Chapter 4

Electron stimulated desorption from cryogenic surfaces

4.1   Description of the experiment

The purpose of this experiment is a quantitative and qualitative investigation of the electron stimulated desorption (ESD) yield as a function of the gas coverage and the electron energy at cryogenic temperatures. It has been shown already in chapter 2, that the desorption of gas molecules adsorbed on the surfaces of the beam vacuum system, induced by photons, ions, and/or electrons has a major influence on the performance of the accelerator.

The idea is to measure the ESD yield of a sample at certain gas coverages and electron energies at a temperature of 4.2 K. The *characteristics* of the ESD yield can then be compared with the characteristics of other particle induced desorption yields under similar conditions and/or with the characteristics of ESD yields under different conditions. Furthermore, similar experiments have been carried out since many years in order to investigate the characteristics of particle induced desorption (e. g. [36, 37, 38, 60, 61, 62]), hence the characteristics of the ESD yield can be compared with those results. The measurements of the ESD yields is hence needed to predict the vacuum behavior in the LHC, and to understand the mechanism of ESD from condensed gas layers.

In this experiment, the sample material is copper. The sample is bombarded by electrons. As it will be shown in the next section electrons can be produced using a hot filament and can be accelerated towards the sample by applying a (electrostatic) potential difference between sample and filament. Thus an electron stimulated experiment is much easier to implement than

comparable experiments for ion induced desorption (requires an ion gun) or photon induced desorption (requires a synchrotron or another high intensity light source).

4.2 Experimental setup

As shown in figure 4.1 the experimental setup consists of two parts. The
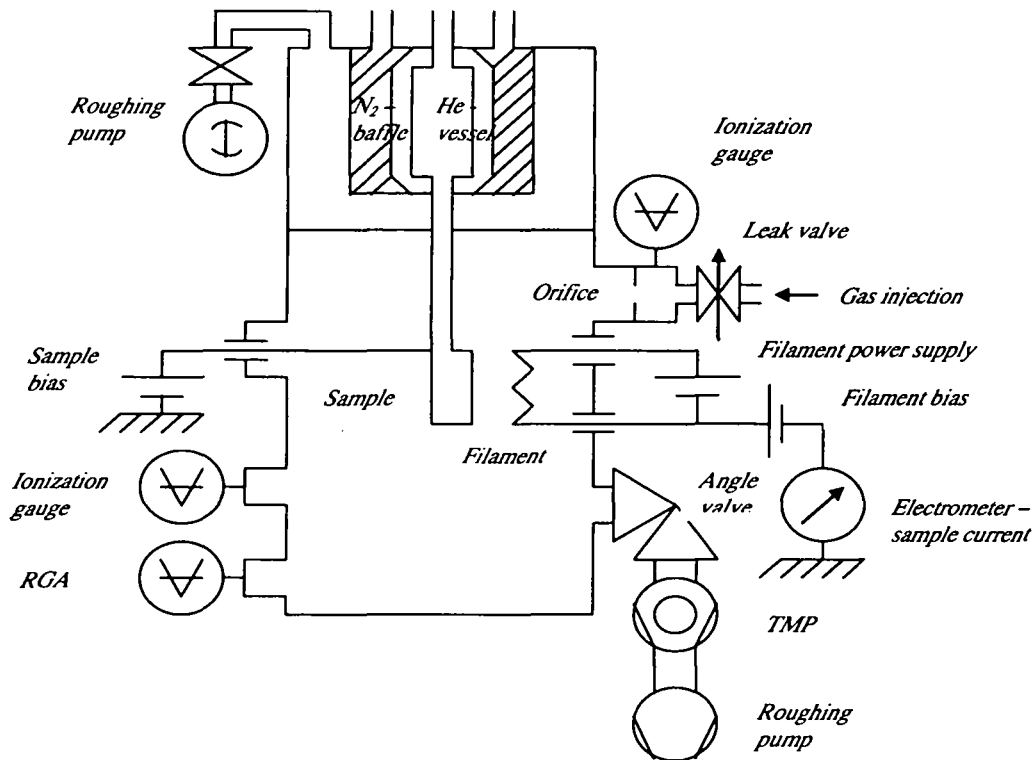
Figure 4.1: Schematic drawing of the experimental setup for the ESD measurements.

upper part is used to cool the sample with liquid helium and to keep the sample at a temperature of 4.2 K. This part shall be called the *cryogenic system*. The lower part is used to perform the ESD measurement. It shall be called the *vacuum system*. The pressure during measurement is typically in the range of 1×10^{-6} Pa. The upper and the lower part are connected by the cooling tube (see figure 4.2), which is a hollow cylinder electrically insulated by a glass section.

To store the liquid helium for a reasonable time, in our case for about one
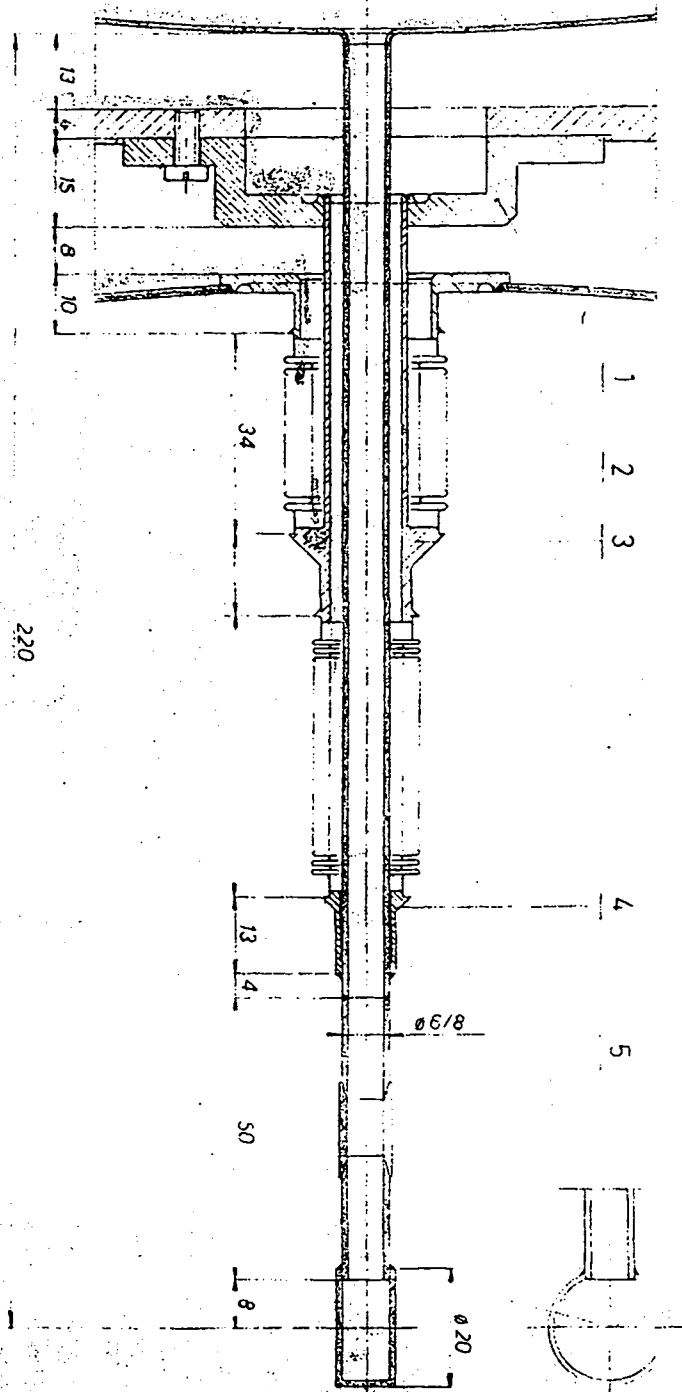
Figure 4.2: Cutaway drawing from the cooling tube.

41

day, the helium vessel (1) is surrounded by a liquid nitrogen baffle (2) and an isolation vacuum. To maintain the isolation vacuum a rotary vane pump (3) - an ALCATEL 2012A is used. (The numbers in the parentheses are referred to the numbers in fig. 4.4, 4.5, 4.6). This pump has a nominal pumping speed of 8 $m^3 \cdot h^{-1}$. The cooling tube is 23 cm long and has an inner diameter of 12 mm as shown in figure 4.3. The material is stainless steel from the type
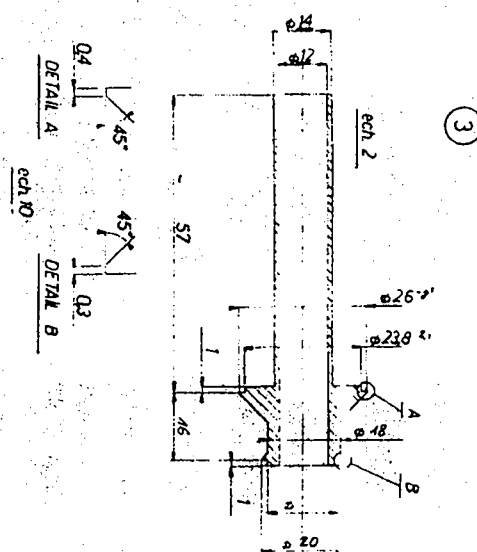
Figure 4.3: Exploded view from a part of the cooling tube.

AISI 316LN. The use of bellows between room temperature and liquid nitrogen temperature and between liquid nitrogen and liquid helium temperature allows to reduce the area of the surfaces at intermediate temperature while keeping the liquid helium consumption reasonable. This results in a reduced uncertainty on the condensing area and on the condensed gas coverage.

The lower vacuum chamber is equipped with the following instrumentation, required for the measurement of the electron stimulated desorption yield:

- a pumping group, consisting of a turbomolecular pump (17) with a nominal pumping speed of 230 $l \cdot s^{-1}$ and a roughing pump (18)

- a quadrupole mass spectrometer (16) - QMG 112 by Balzers instruments - with a secondary electron multiplier for partial pressure measurement

42

- a Bayard Alpert gauge (15) for total pressure measurement

- a heated thorium coated tungsten filament (10), placed at a distance of about 5 cm in front of the sample (9) for the electron production

For calibration and gas injection purposes a gas injection line (6), equipped with an Sapphire-sealed variable leak valve (7) (by VARIAN) is connected to the vacuum chamber. In addition, this injection line is equipped with an orifice (5) and a second Bayard Alpert gauge (4). As we will see later on, this setup permits the determination of the amount of condensed gas, calibration of the mass spectrometer and the measurement of the effective pumping speed of the turbomolecular pump and the cold target.

The thorium coated tungsten filament is powered by a direct current power supply (11) (typical operating conditions: 2...3 A, 4...9 W) and is biased to +9 V with respect to ground[1] in order to prevent electrons from hitting the surrounding vacuum chamber. Electrons are extracted from the filament and accelerated towards the sample by applying a positive potential (with respect to the filament) to the sample. For this purpose, the sample is electrically isolated from the vacuum chamber.[2] In addition this electrical connection is equipped with an electrometer (13) in order to measure the electron current received by the sample. A bias voltage supply (8), stepwise adjustable between 0 V and +3 kV is connected to the sample by means of a vacuum power feed-through. Electron bombardment is initiated by changing the bias voltage from 0 V to 49 V, 109 V, 309 V, 509 V, 709 V and 1009 V thereby generating a potential difference between sample and filament of 40 V, 100 V, 300 V, 500 V, 700 V and 1000 V hence the electrons hit the sample with an kinetic energy of 40 eV, 100 eV, 300 eV, 500 eV, 700 eV and 1000 eV. Measurement data are recorded by a three-channel flatbed recorder.[3]

A complete experimental run for one gas involves the following steps:

1. baffle filling with liquid nitrogen

2. sample cooling with liquid helium

3. defined gas injection in the vacuum chamber

4. measurement of the molecular desorption yield of the gas condensed on the sample

---

[1]hence, as well with respect to the surrounding vacuum chamber, which is grounded
[2]by means of a glass spacer
[3]GOERZ SERVOGOR 124PLUS

5. repeat steps 3 and 4 with different amount of injected gas and electron energy

Some photos of the experiment are shown in figure 4.4, 4.5 and 4.6.

4.3 Determination of the molecular desorption yield

4.3.1 Theoretical and experimental prerequisites

Basic equations

The partial pressure of each species is related to its molar density according to *Daltons law*

$$p_j = n_j \, kT \tag{4.1}$$

and the total pressure is related to the total molar gas density by the *ideal gas law*

$$p = nkT. \tag{4.2}$$

In the equations 4.1 and 4.2 p_j and n_j are the partial pressure and molar density of species j, p and n the total pressure and molar density, k the Boltzmann constant and T the absolute temperature. If the transformation of species (e.g. due to chemical reactions) can be neglected then it holds for the partial pressure of each species

$$V \, \frac{\partial p_j}{\partial t} = \dot{Q}_j - p_j \, S_j \tag{4.3}$$

and in the steady state

$$\dot{Q}_j = p_j \, S_j. \tag{4.4}$$

In equations 4.3 and 4.4 V is the volume of the vacuum chamber and $\dot{Q}_j$ and S_j are the overall gas load[4] (due to outgassing, leaks, etc.) and the effective pumping speed of species j, respectively. Let us assume that without electron stimulated desorption, the vacuum chamber has reached a steady state which is characterized by the "background" pressure $p_j^{(0)}$. The desorption of gas molecules adsorbed on the cold surface represents an additional gas load for the vacuum system. With the presence of electron stimulated desorption

---

[4]measured in units of Pa $\cdot$ m$^3 \cdot$ s^{-1}
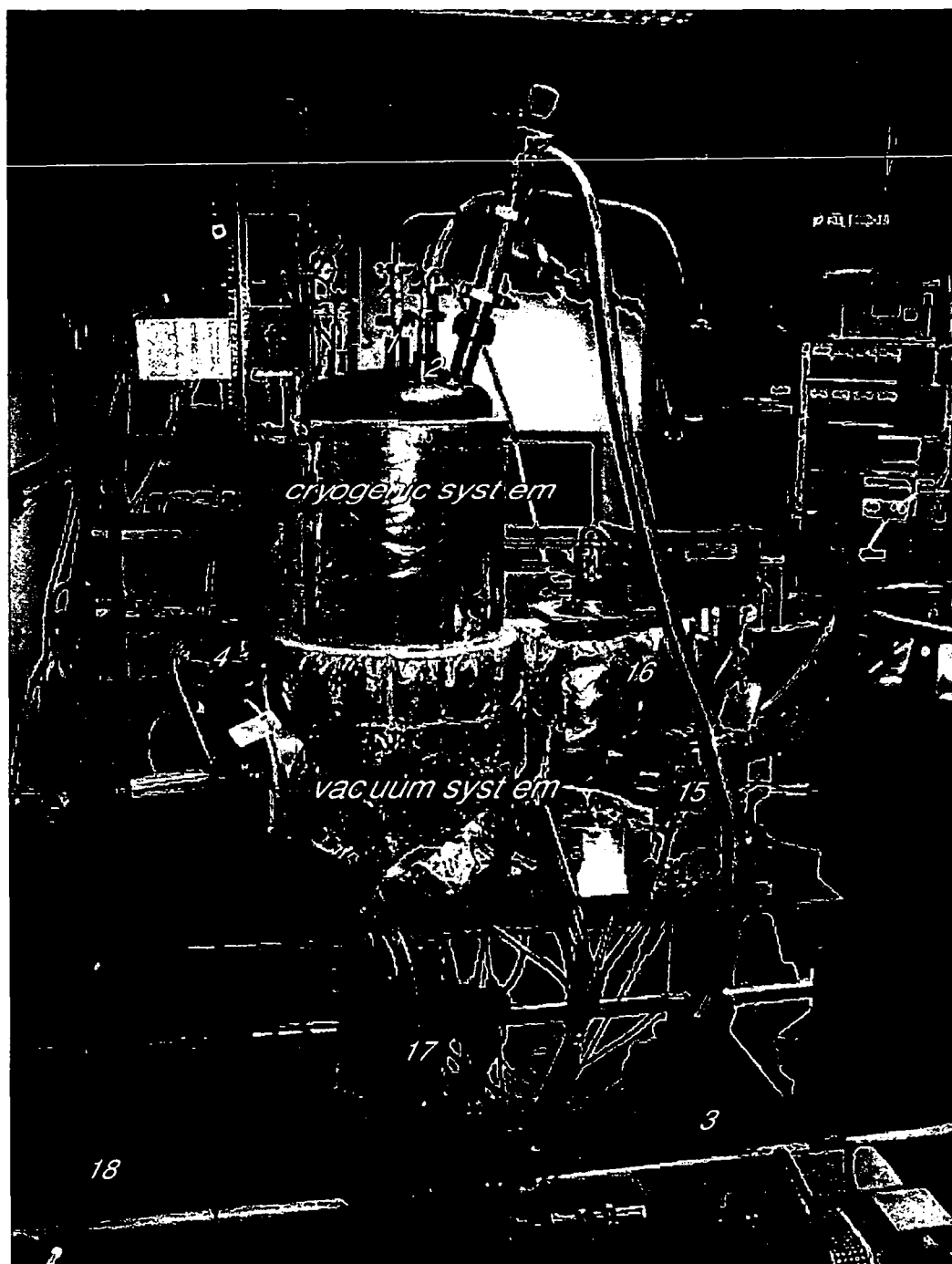
Figure 4.4: Photograph of the experimental setup. 1) inlet to liquid helium vessel; 2) inlet to liquid nitrogen baffle; 3) rotary vane pump for isolation vacuum; 4) Bayard Alpert gauge on gas injection side; 15) Bayard Alpert gauge in vacuum chamber; 16) quadrupole mass spectrometer; 18) roughing pump.

45
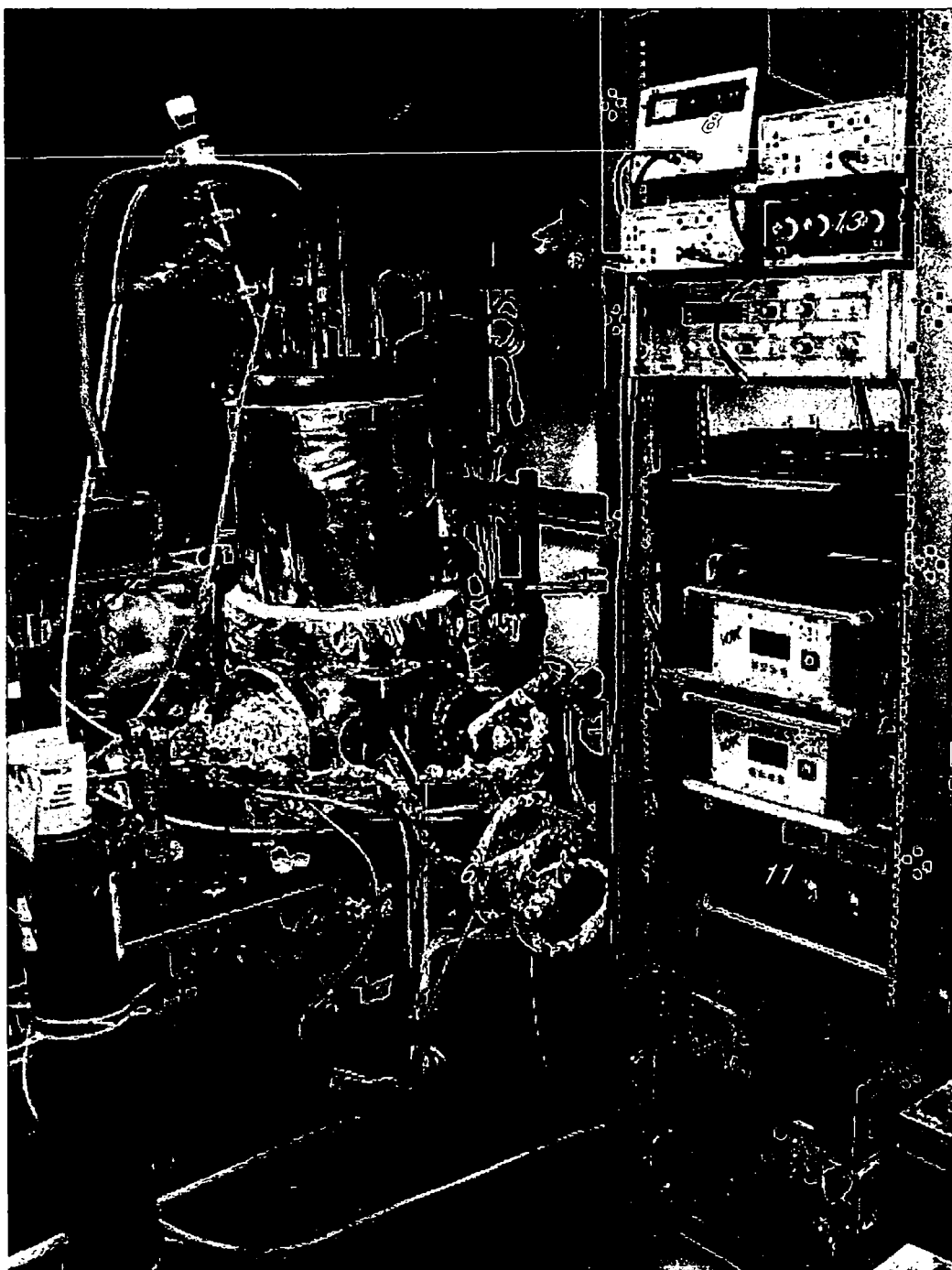
Figure 4.5: Photograph of the experimental setup. 6) gas injection line; 7) Sapphire-sealed variable leak valve; 8) bias voltage supply; 11) current power supply; 13) current amplifier for sample current measurement.
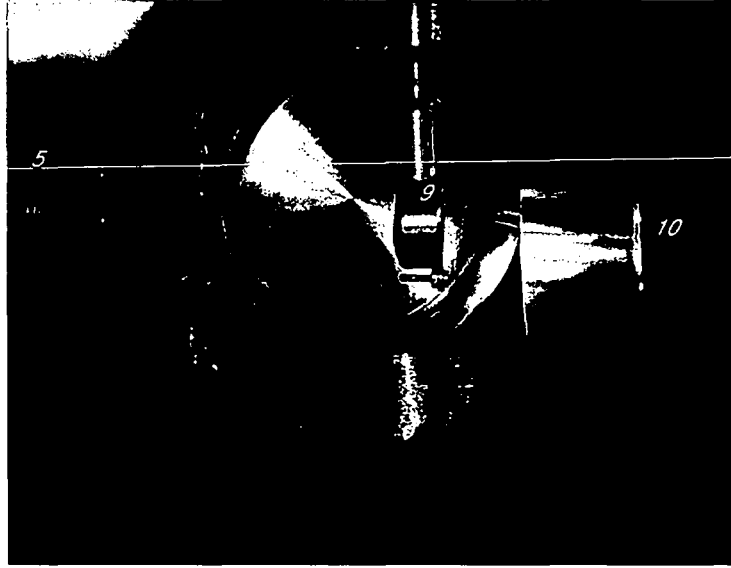
Figure 4.6: Photograph of the vacuum chamber. 5) orifice; 9) copper sample; 10) thorium coated tungsten filament.

the pressure will therefore rise to a new steady state value[5], say $p_j^{(1)}$. This pressure rise can be characterized by the following equation

$$\left(p_j^{(1)} - p_j^{(0)}\right) S_j = \eta_j \frac{I_S}{e} kT \qquad (4.5)$$

where η_j is the molecular desorption yield, I_S the current of impinging electrons, e the elementary charge, and k the Boltzmann constant. The fraction I_S/e gives the number of electrons hitting the surface per unit time. Since η_j is per definition the number of gas molecules (of species j) desorbed per incident electron (cf. section 2.4), the expression $\eta_j I_S/e$ gives the number of molecules desorbed due to electron bombardment per unit time.

Pumping speed

In order to calculate the molecular desorption yield η_j from equation 4.5, the partial pressure of species j (with and without desorption), the electron current I_S, the temperature and the effective pumping speed of the vacuum system for species j must be measured. The measurement of the pumping speed is a relatively straight forward process and has been determined during

---

[5]the characteristic rise time is actually given by the quotient V/S_j

each gas injection. It shall be explained briefly in the following paragraphs.

For the measurement of the effective pumping speed, we make use of the orifice, the second Bayard Alpert gauge and the gas injection system, as illustrated in figure 4.1. Prior to gas injection the vacuum system is in steady state,[6] hence the signals from the two gauges do not change with time. During gas injection, the signals of the two gauges increase until a new steady state value is reached. This new balance is characterized by the equation

$$\Delta p_j \ S_j = (\Delta \hat{p}_j - \Delta p_j) \ C_j. \tag{4.6}$$

Δp_j and $\Delta \hat{p}_j$ are the pressure rises measured by gauge 1 and 2, respectively,[7] and C_j is the conductance of the orifice for species j, which is for molecular flow given by

$$C_j = A \ \frac{\bar{v}_j}{4} \tag{4.7}$$

where A is the opening area of the orifice and $\bar{v}_j$ the mean thermal velocity of species j. Calculation of the effective pumping speed follows directly from equation 4.6. Table C.1 in appendix C summarises the values of the effective pumping speed for the injected gases.

Functional principles of ionization gauges and the mass spectrometer

Bayard Alpert type gauges do not measure pressure directly, i.e. by measuring the force per unit area. Instead, they measure a current of positive ions generated by the ionization of residual gas molecules (cf. [99]). The ionizing particles are electrons emitted by a hot filament, the so-called *hot cathode*. Thus, the raw signal coming from those gauges is an electrical current which is proportional to the number of emitted electrons (also called the *emission current*) and the residual gas density, i.e. (for a fixed temperature)

$$I^* = I_e^* \sum_j s_j^* \ p_j \tag{4.8}$$

where I^* is the raw gauge signal, also called the *gauge collector current*, and I_e^* the emission current. s_j^* is called the *absolute sensibility* of the gauge for species j. Values for the absolute sensibilities of the two gauges used in this experiment are given in table C.3 in appendix C.

---

[6]the characteristic rise time is actually given by the quotient V/S_j

[7]In fact, a total pressure gauge cannot measure partial pressure, but since we are injecting gas of a single species, the increase in total pressure corresponds to the increase in partial pressure of this species.

The quadrupole mass spectrometer works in principle like an ionization gauge. First, residual gas molecules are ionized and/or cracked into smaller fragments using electrons as ionizing particles. The resulting (positive) ions are sent through a quadrupole mass filter (cf. [100]) where they are selected according to their mass-to-charge ratio. Those ions which pass the filter are then counted. In the case of our experiment the quadrupole mass spectrometer counts ions by means of a so-called *secondary electron multiplier*. Hence, the raw output signal of the mass spectrometer is an electron current, proportional to the ion count rate, which is in turn proportional to the emission current and the density of residual gas molecules, i.e. (again for a fixed temperature)

$$I_m^+ = I_e \sum_j s_{m,j} \, p_j. \tag{4.9}$$

The subscript m indicates the setting of the mass filter, i.e. the mass-to-charge ratio of the ions that can pass the filter. In fact, m is the approximate numerical value of the ion mass, measured in atomic mass units, divided by the ionization degree. From here on, the mass-to-charge ratio will be denoted as M/Z. I_m^+ is the raw output signal of the mass spectrometer at $M/Z = m$, also called the *ion current*, and $s_{m,j}$ is the *absolute sensibility* of the mass spectrometer at $M/Z = m$ for species j. I_e is again the emission current.

Before the mass spectrometer can be used as a measuring device, values for the sensibilities $s_{m,j}$ have to be determined by means of a calibration procedure. For the purpose of the calibration pure gases are injected into the vacuum system and the change in the mass spectrometer signal is recorded together with the change in the total pressure. A typical set of such calibration curves is shown in figure 4.7

The absolute sensibilities can change significantly with time with a typical timescale of days, but they change proportional to each other.[8] Hence, absolute sensibilities are usually given as a multiple of a *reference sensibility* s_{ref}[9], i.e.

$$s_{m,j} = s_{ref} \, s_j' \, x_{m,j}. \tag{4.10}$$

s_j' is called the relative sensibility for species j and x_m, j the *cracking pattern* for species j at $M/Z = m$. Relative sensibilities and cracking patterns do not change significantly with time. Tables C.4 and C.5 in appendix C summarise

---

[8]i.e. the mass spectrometer can count more or less ions per emitted electron, but it does so in the same manner for all kinds of ions

[9]the reference sensibility is by convention equal to the absolute sensibility of the mass spectrometer for H_2^+
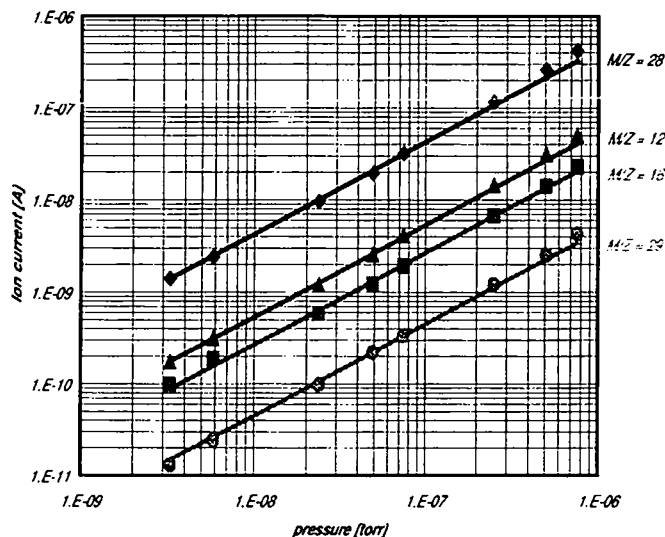
Figure 4.7: A set of calibration curves for carbon monoxide

numerical values for s_j^* and $x_{m,j}$, respectively, obtained from calibration process.

4.3.2 Measurement procedure

The molecular desorption yield shall be determined for the gases hydrogen (H_2), methane (CH_4), nitrogen (N_2), carbon monoxide (CO), carbon dioxide (CO_2), neon (Ne), argon (Ar), krypton (Kr), xenon (Xe) and gas mixtures corresponding to: (all compositions given in atomic percent) 25% H_2, CH_4, CO, CO_2 and 0.8% H_2, 2.3% CH_4, 6.2% CO, 90.7% CO_2 condensed on a liquid helium (4.2 K) cooled copper surface. For this purpose data are recorded with the mass spectrometer set at M/Z = 2, 15, 20, 28, 40, 44, 66 and 84. For each setting of the mass spectrometer a desorption pulse is recorded, i.e. the bias voltage of the sample is switched from 0 V to +49 V, 0 V to +109 V, 0 V to +309 V, 0 V to +509 V, 0 V to +709 V, 0 V to +1009 V, kept there for about 10 seconds, and then switched back to 0 V, while at the same time the signals of the total pressure gauge and the mass spectrometer and the sample current are recorded.

In figure 4.8, signals of a desorption pulse, recorded with a setting of the QMS of M/Z = 44 are shown. The graph shows the signal from a CO_2 condensed

50
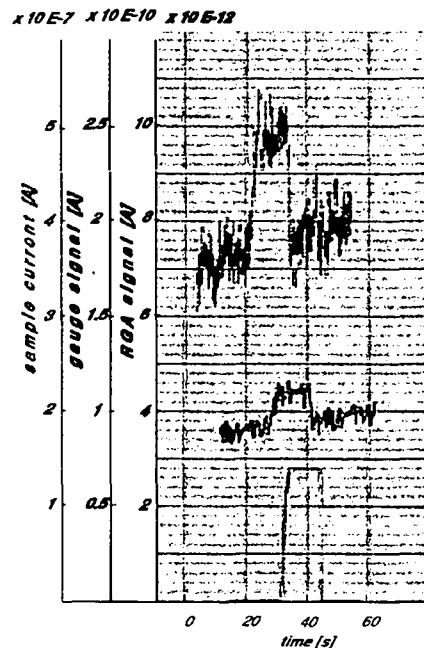
Figure 4.8: Desorption pulses, recorded at M/Z = 44.

sample. This graph gives a good example of how the current of bombarding electrons (i.e. the sample current) has to be chosen sufficiently high in order to get an acceptable signal-to-noise ratio in the gauge and QMS signals. Of course, a higher sample current would produce a better signal (i.e. a higher Δp), but this also means that molecules would be desorbed at a much higher rate, which in turn means that the sample would already be cleaned by the measurement process itself. Hence, the correct choice of the sample current represents a compromise between a good signal and a sufficiently low desorption rate. Since the rate of electrons emitted by the filament is a strong function of its temperature (*Richardsons law*, cf. [101]), the sample current can be adjusted by limiting the current which is heating the filament.

The desorption pulses as shown in figure 4.8 contain all the information required to calculate η (except for calibration data). As mentioned already in the previous section, the formula for the calculation of the molecular desorption yield is given by

$$\left(p_j^{(1)} - p_j^{(0)}\right) S_j = \eta_j \, \frac{I_S}{e} \, kT \tag{4.11}$$

51

or

$$\eta_j = \frac{(p_j^{(1)} - p_j^{(0)})\ S_j\ e}{I_S\ kT}.$$ (4.12)

The partial pressures $p_j^{(0)}$ are determined from the gauge and mass spectrometer signals before and after the desorption pulse. Likewise, the partial pressures $p_j^{(1)}$ are determined from the gauge and mass spectrometer signals during the desorption pulse. T is assumed as 300 K. The estimated variance of η_j is given through the law of propagation of uncertainties as

$$\frac{\sigma^2(\eta_j)}{\eta_j^2} = \frac{\sigma^2(p_j^{(0)}) + \sigma^2(p_j^{(1)})}{(p_j^{(1)} - p_j^{(0)})^2} + \frac{\sigma^2(S_j)}{S_j^2} + \frac{\sigma^2(I_S)}{I_S^2}$$ (4.13)

where the variances $\sigma^2(p_j^{(0)})$, $\sigma^2(p_j^{(1)})$, $\sigma^2(S_j)$ are estimated from the total pressure gauge and mass spectrometer data as indicated in appendix D and the variance of the sample current, $\sigma^2(I_S)$, is taken from measurement.

4.4 Determination of the sticking probability

4.4.1 Theoretical and experimental prerequisites

Basic equations

In an adsorption cell with a steady pressure and a clean target, gas is introduced through an orifice with the conductance C_j. The cell pressure rises almost instantaneously by an amount $p_j(0)$ and then continues to rise more slowly as adsorption proceeds on the flow area of the target. A typical recorder trace is shown in fig. 4.9. We define the time as $t = 0$ when the gas is allowed into the cell; the pressure at any time t during gas adsorption is $p_j(t)$. At steady state the rate of gas inflow, given by the flux intensity $A_j\ Q$ (molecules $\cdot$ sec^{-1}), is balanced by the rates of adsorption on the condensation area A_j of the target and the target supports.

$$S_j = \Delta p_j(t)\ C_j = s(t)A_j\ Q = s(t)A_j \frac{p_j(t)}{\sqrt{2\pi mkT}}$$ (4.14)

here $s(t)$ is the sticking probability on the condensation area of the target and the target supports at time t. The following expression is the obtained for $s(t)$:

$$s(t) = \frac{S_j}{A_j\ Q} = \frac{S_j\sqrt{2\pi mkT}}{A_j\ p_j(t)}$$ (4.15)
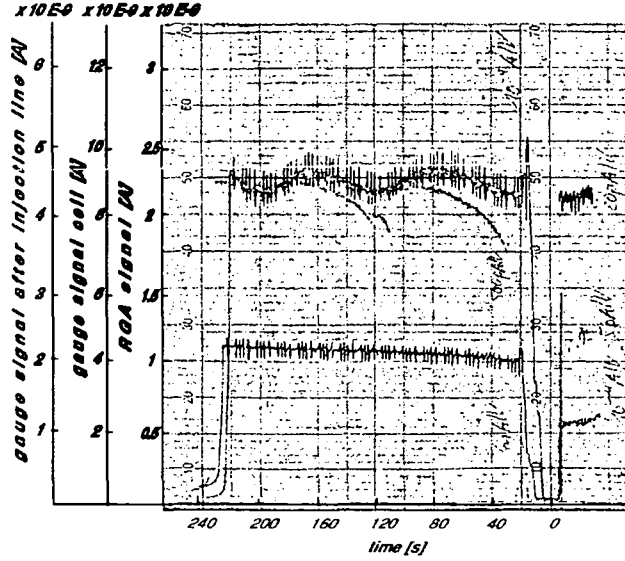
Figure 4.9: Recorder trace of the cell pressure during adsorption on the copper target at 4.2K.

All the parameters of equation 4.15 are experimentally accessible. Surface coverages $\Theta(t)$ (molecules $\cdot$ cm^{-2}) can be obtained, since

$$\Theta(t) = Q \int_0^t s(t)dt, \qquad (4.16)$$

and the sticking probability profile, s versus Θ, can therefore constructed.

Condensation area

In order to calculate the sticking probability s from equation 4.15, the partial pressure of species j, the effective pumping speed of the vacuum system for species j must be measured and and the condensation area A_j for species j must be calculated. The results of the condensation area have been determined for each gas. It shall be explained briefly in the following paragraph.

For the calculation of the condensation area, we have to determine, depending from the condensation temperature of each gas, the area of the two bellows as illustrated in figure 4.2. The use of bellows between room temperature and liquid nitrogen temperature and between liquid nitrogen and liquid helium temperature allows reducing the area of the surfaces at intermediate temperature. This results in a reduced uncertainty on the condensing area

and hence on the condensed gas coverage. This area is characterised by the equation

$$A_{b,j} = d\pi l_j. \tag{4.17}$$

$A_{b,j}$ is the condensation area on the bellow for species j, d is the diameter of the bellow and l_j is the effective length of condensation for species j, which is given by

$$l_j = \frac{A_{b,cross} \int_{T_0}^{T_L} \lambda dT}{P} \tag{4.18}$$

where $A_{b,cross}$ is the cross section of the bellow, λ the thermal conductivity and P the heat of flow. Data for the thermal conductivity integrals for stainless steal are given in table C.6 in appendix C. The total condensation area is then given by

$$A_j = A_{b,j} + A_T \tag{4.19}$$

where A_T is the condensation area on the target and the target support at 4.2 K and $\sim$ 2 K for H_2, respectively. Table C.7 in appendix C summarises the values of the condensation area for the injected gases.

4.4.2 Measurement procedure

The sticking probability shall be determined for the gases hydrogen (H_2), methane (CH_4), nitrogen (N_2), carbon monoxide (CO), carbon dioxide (CO_2), neon (Ne), argon (Ar), krypton (Kr), and xenon (Xe) condensed on a liquid helium (4.2 K and $\sim$ 2 K for H_2) cooled copper surface. For this purpose data are recorded with the mass spectrometer set at $M/Z = 2$, 15, 20, 28, 40, 44, 66 and 84. For each setting of the mass spectrometer the signals of the total pressure gauge in the adsorption cell and after the injection line, and the mass spectrometer are recorded.

The signals during gas injection as shown in figure 4.9 contain all the information required to calculate s. As mentioned already in the previous section, the formula for the calculation of the sticking probability is given by

$$s(t) = \frac{S_j}{A_j\, Q} = \frac{S_j \sqrt{2\pi m k T}}{A_j\, p_j(t)}. \tag{4.20}$$

The partial pressures $p_j(t)$ are determined from the gauge and mass spectrometer signals before and during the gas injection. The estimated variance of s_j is given through the law of propagation of uncertainties as

$$\frac{\sigma^2(s_j)}{s_j^2} = \frac{\sigma^2(S_j)}{S_j^2} + \frac{\sigma^2(A_j)}{A_j^2} + \frac{\sigma^2(p_j(t))}{p_j^2(t)} \tag{4.21}$$

where the variances $\sigma^2(S_j)$ and $\sigma^2(p_j(t))$ are estimated from the total pressure gauge and mass spectrometer data as indicated in appendix D and the variance of the condensation area, $\sigma^2(A_j)$, is taken from calculation.

4.5 Results

4.5.1 Sticking probability

The sticking probability, s, defined as the ratio of adsorption rate to bombardment rate, and the surface coverage, Θ, are two fundamental parameters in the interaction of gases with metal surfaces. In our case its copper. Sticking probabilities as a function of coverage have been determined for gases H_2, CH_4, CO, N_2, CO_2 and for noble gases Ne, Ar, Kr, Xe. These sticking probabilities of each injected gas are shown in figure 4.10, 4.11, 4.12, 4.13, 4.14, 4.15, 4.16, 4.17, 4.18.
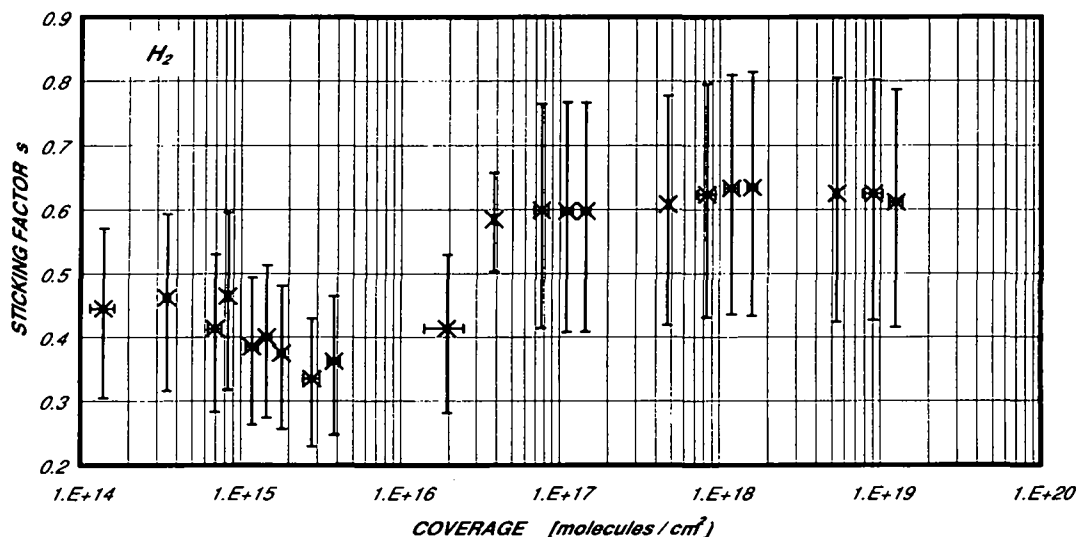

Figure 4.10: Sticking probability as a function of H_2 coverage at approx. 2 K.

Since the adsorption process on clean metal surfaces, here copper, is efficient, with s normally between 0.1 and 1 [102], a method has been devised for measuring adsorption kinetics at very low gas impingement rates (pressures between 10−9 torr and 10−6 torr) in order to achieve a reasonable
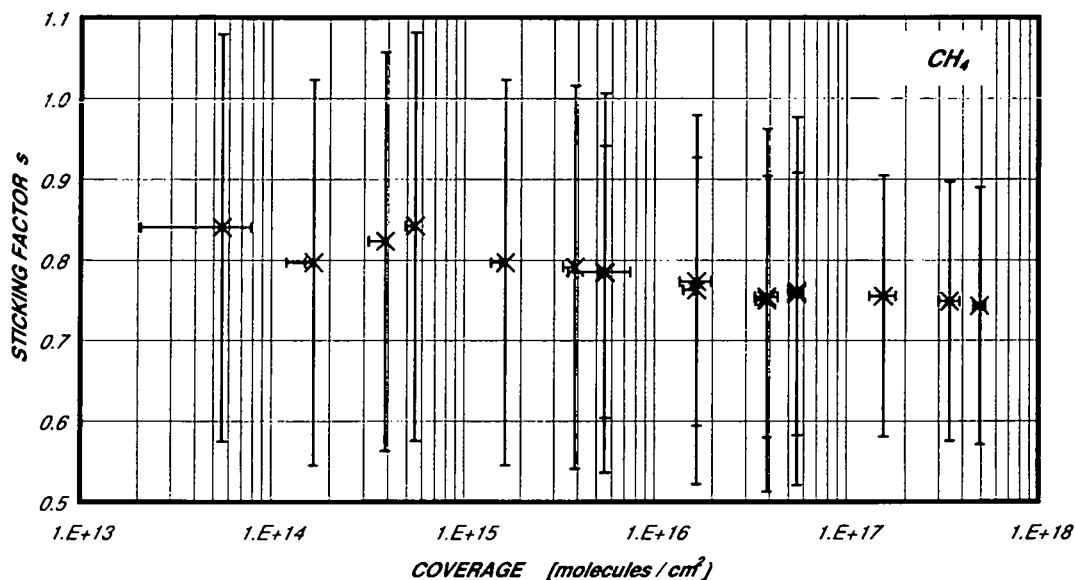
Figure 4.11: Sticking probability as a function of CH_4 coverage at 4.2 K.

experimental time-period. Errors of about 30% in the absolute values of both sticking probabilities and coverages obtained by this technique have been estimated. Figure 4.19 shows the evolution of the sticking probabilities for the same gases as a function of the gas coverage. In this graph error bars have been omitted for reason of clearness. One might say there is a decreasing of the sticking probability s with increasing coverage Θ with the exceptions of H_2, CO_2, Ne and Xe which show an increasing sticking probability with increasing coverage. But in general, under the conditions of coverage between 10^{13} and 10^{20} molecules resp. atoms $\cdot$ cm^{-2} and temperatures of 4.2 K resp. $\sim$ 2 K for H_2, s was found to be independent from Θ within the experimental errors. This is in good agreement with the study from Hayward, King and Tompkins [103].

4.5.2 Desorption yield of H_2, CH_4, N_2, CO, CO_2, Ne, Ar, Kr, Xe and gas mixtures

The desorption of condensed gases has been studied extensively in the context of space research and astrophysics, more especially the case of water ice [104], [105], or in the context of the study of sputtering processes [87], [106], [107].

Figure 4.12: Sticking probability as a function of CO coverage at 4.2 K.

Figure 4.13: Sticking probability as a function of N₂ coverage at 4.2 K.

Figure 4.14: Sticking probability as a function of CO_2 coverage at 4.2 K.
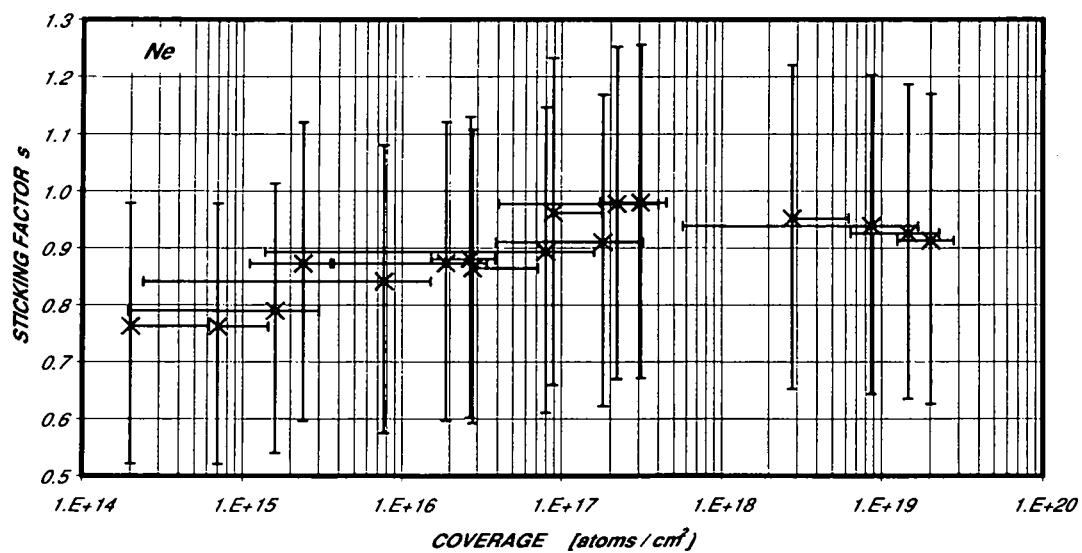
Figure 4.15: Sticking probability as a function of Ne coverage at 4.2 K.
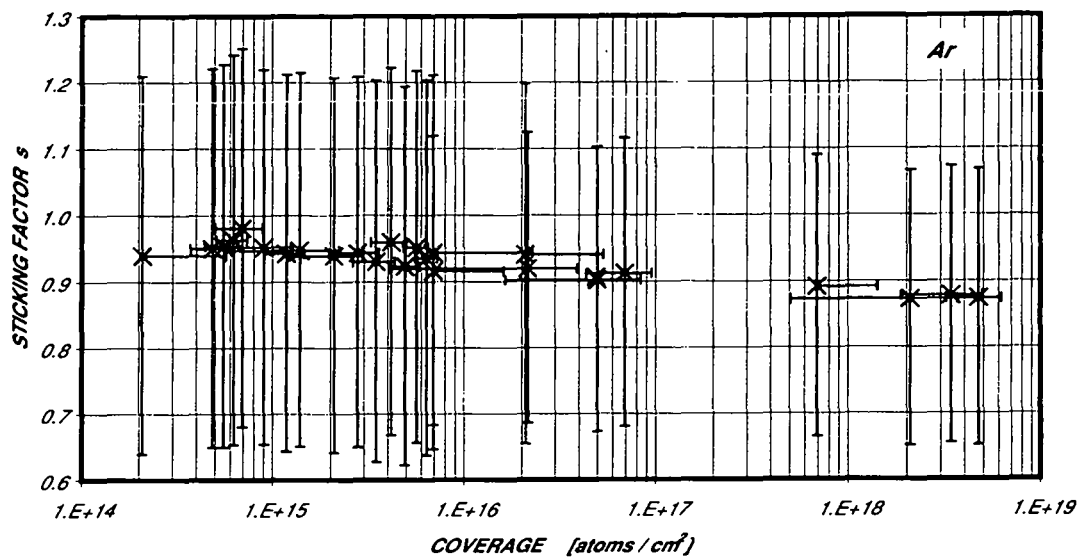
Figure 4.16: Sticking probability as a function of Ar coverage at 4.2 K.
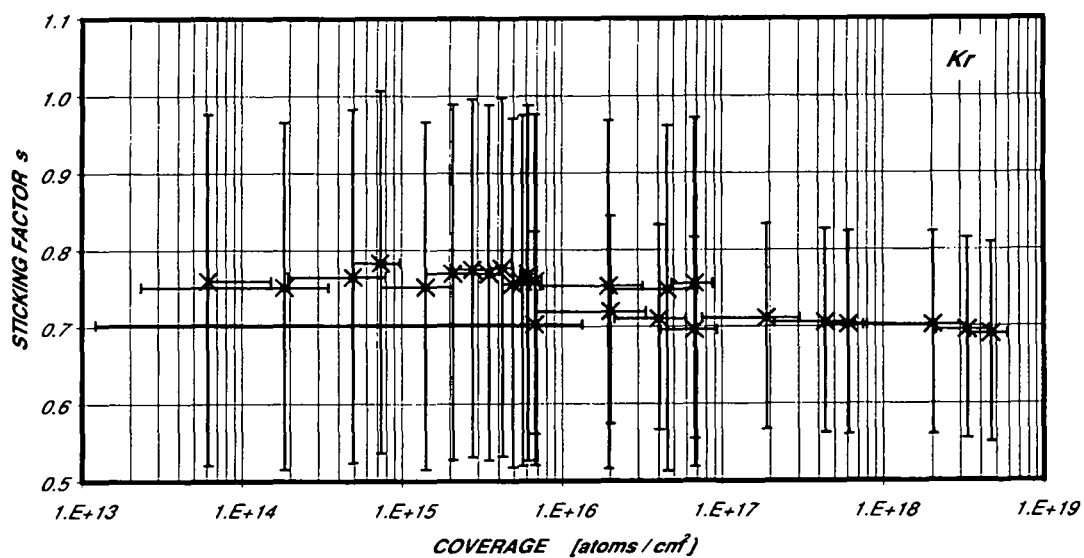
Figure 4.17: Sticking probability as a function of Kr coverage at 4.2 K.
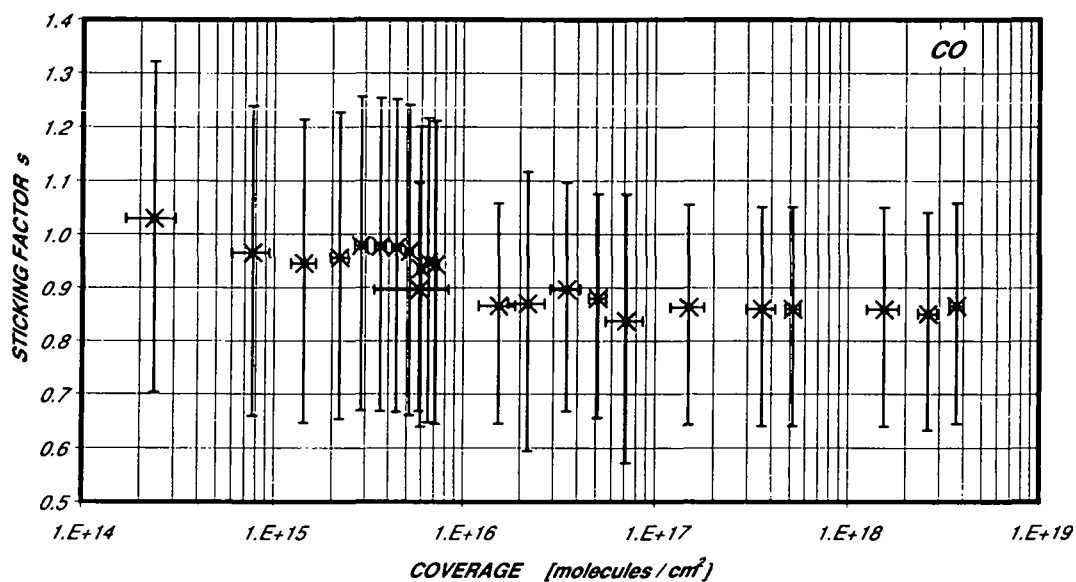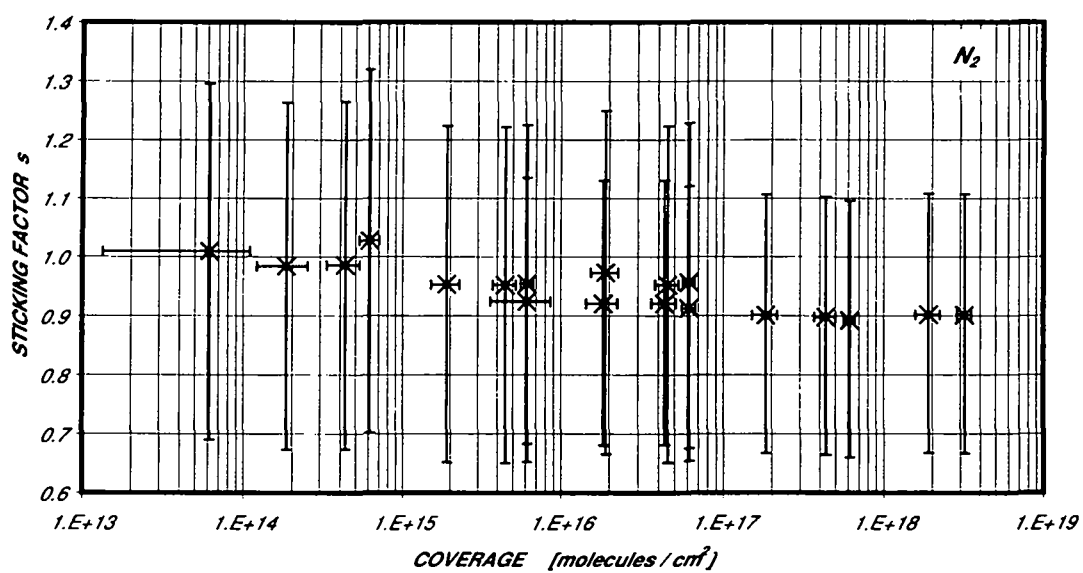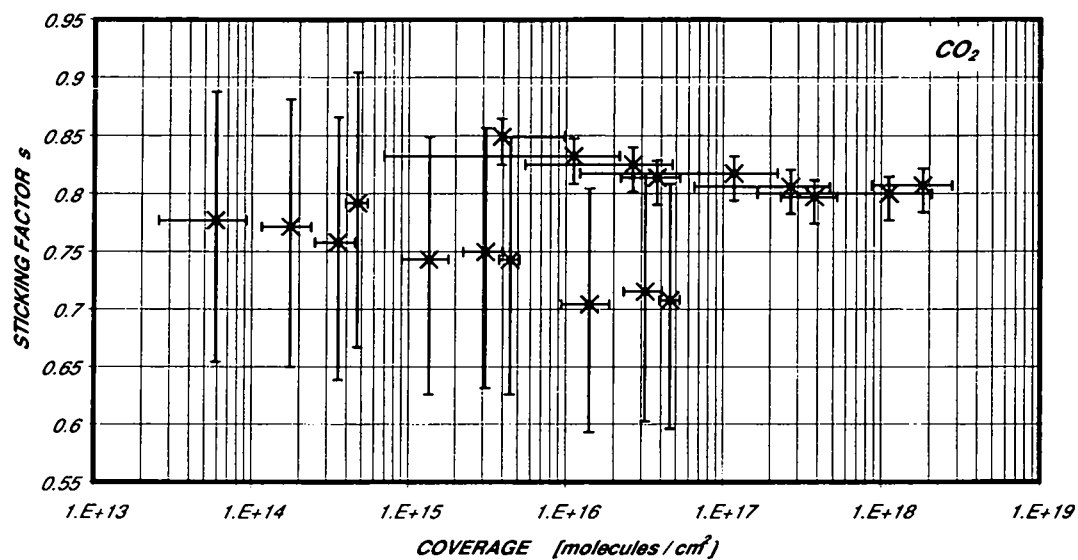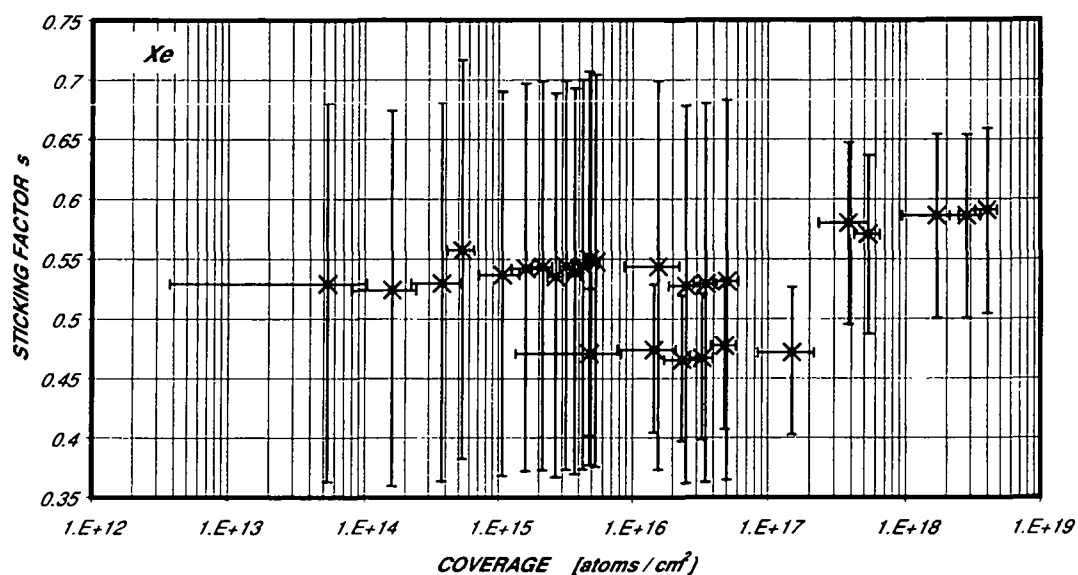
Figure 4.18: Sticking probability as a function of Xe coverage at 4.2 K.
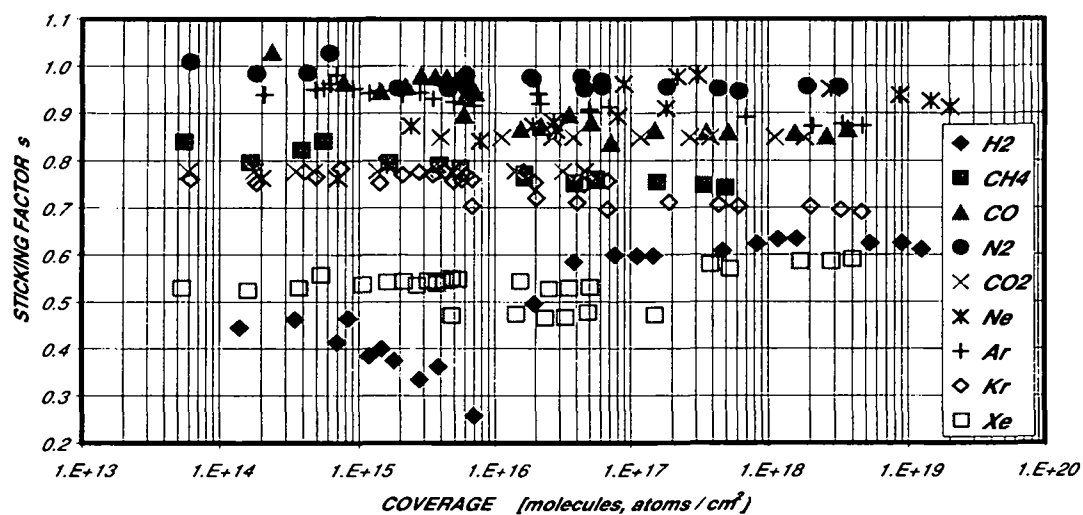
Figure 4.19: Sticking probabilities as a function of gas coverage at 4.2 K resp. ~ 2 K for H₂.

Nevertheless, to our knowledge, few results are available for the desorption of thin condensed gas layers ($<$ 100 monolayers) and low electron energy ($<$ 1 keV). The desorption yields (number of neutral molecules desorbed per incident electron η) have been determined for noble gases Ne, Ar, Kr, Xe; for gases H_2, CH_4, CO, N_2, CO_2 and gas mixtures corresponding to: (all compositions given in atomic percent) 25 % H_2, CH_4, CO, CO_2 and 0.8 % H_2, 2.3 % CH_4, 6.2 % CO, 90.7 % CO_2 using respectively the peaks 20, 40, 84, 66 and 2, 15, 28, 44 of the mass spectrum.

Desorption yields of H_2, CH_4, CO, N_2 and CO_2

The variation of the desorption yield as a function of the gas coverage at different electron energies is shown in figure 4.20, 4.21, 4.22, 4.23 and 4.24.
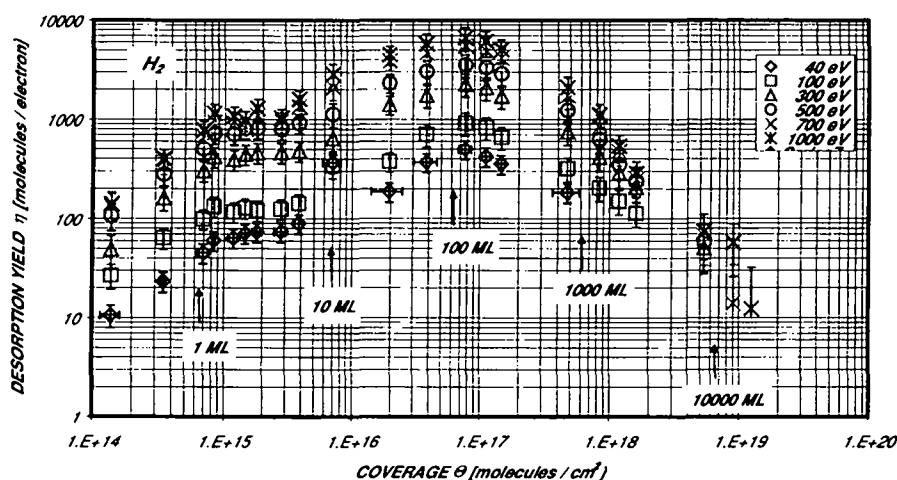
Figure 4.20: The desorption yield of H_2 as a function of H_2 coverage at different electron energies.

For H_2 and CH_4 the maximum of the desorption yield is at an electron energy of 1000 eV, whereas for CO, N_2 and CO_2 the maximum of the desorption yield is at an electron energy of 700 eV within the experimental errors. Errors in the absolute desorption yield of about 30% have been estimated. In figure 4.25 the gases show a maximum in the desorption yield at about 10^{15} molecules $\cdot$ cm^{-2} followed by a minimum when the coverage increases and a

Figure 4.21: The desorption yield of CH₄ as a function of CH₄ coverage at different electron energies.

Figure 4.22: The desorption yield of CO as a function of CO coverage at different electron energies.

Figure 4.23: The desorption yield of N_2 as a function of N_2 coverage at different electron energies.

Figure 4.24: The desorption yield of CO_2 as a function of CO_2 coverage at different electron energies.

63

Figure 4.25: The desorption yield of H_2, CH_4, CO, N_2 and CO_2 as a function of the gas coverage at an electron energy of 300 eV.

constant value at a coverage greater than 10^{17} resp. 10^{18} molecules $\cdot$ cm^{-2}. Error bars have been omitted for reason of clearness. Exception is hydrogen were the maximum of the desorption yield lies at about 10^{17} molecules $\cdot$ cm^{-2}. Figure 4.26 shows the evolution of the desorption yields for the same gases as a function of the electron energy for a low coverage, corresponding to the first peak of desorption in figure 4.25 i. e. a coverage of $\sim 10^{15}$ atom $\cdot$ cm^{-2} resp. $\sim 10^{17}$ atom $\cdot$ cm^{-2} for H_2. Again, error bars have been omitted for reason of clearness.

Desorption yields of noble gases

The variation of the desorption yield as a function of the gas coverage at different electron energies is shown in figure 4.27, 4.28, 4.29 and 4.30.

The maximum of the desorption yield is at an electron energy of 1000 eV within the experimental errors.

The variation of the desorption yield as a function of the gas coverage is shown in figure 4.31. At a coverage close to 10^{15} atom $\cdot$ cm^{-2} the desorption yield passes a maximum. For heavier gases: Xe, Kr, this maximum is followed by a minimum when the coverage increases and a constant value is reached at
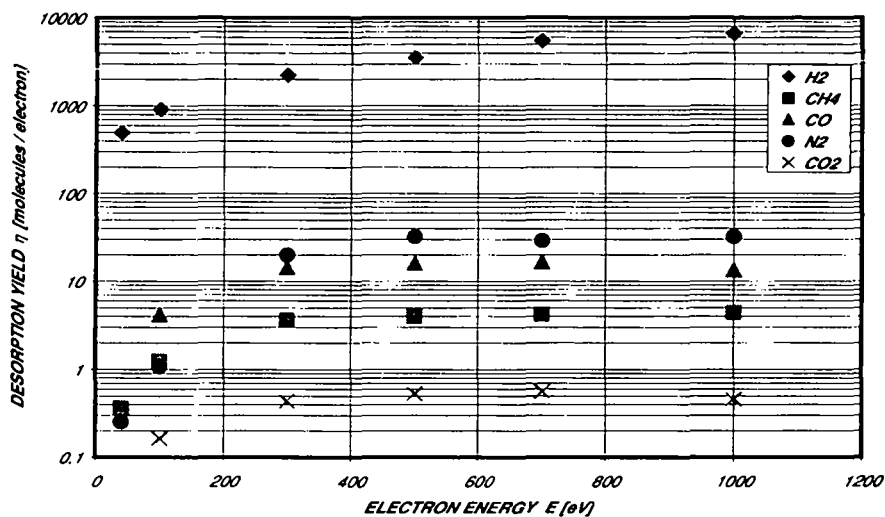
Figure 4.26: The desorption yield of H_2, CH_4, CO, N_2 and CO_2 as a function of the electron energy.
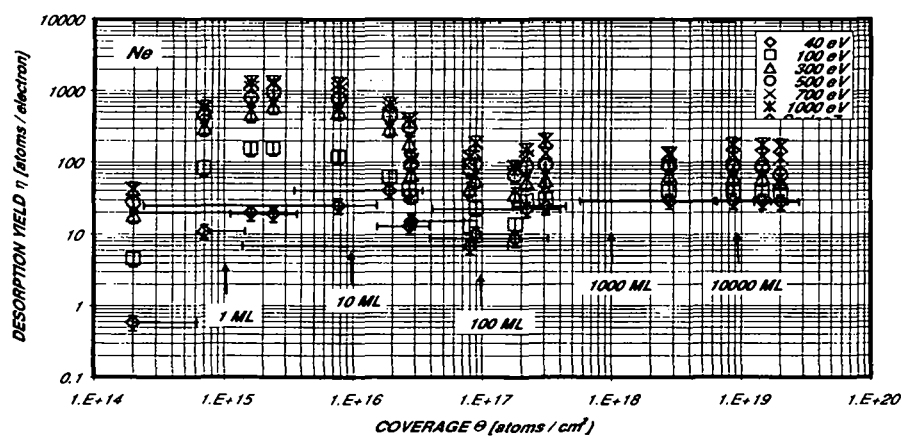
Figure 4.27: The desorption yield of Ne as a function of Ne coverage at different electron energies.
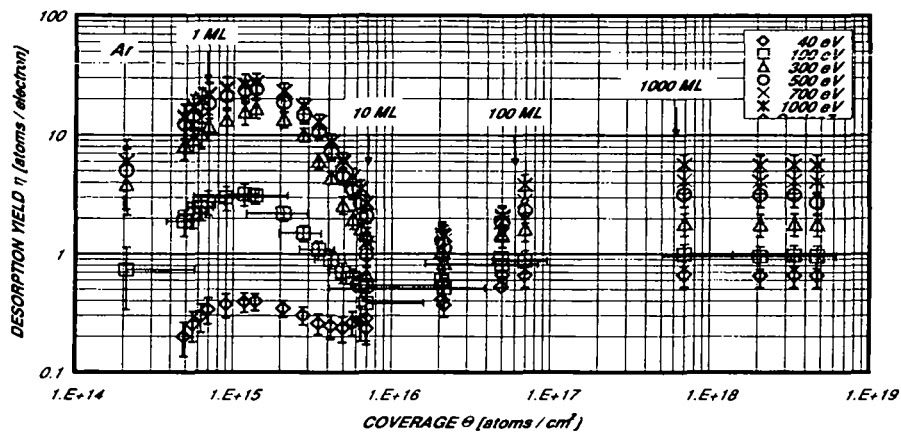
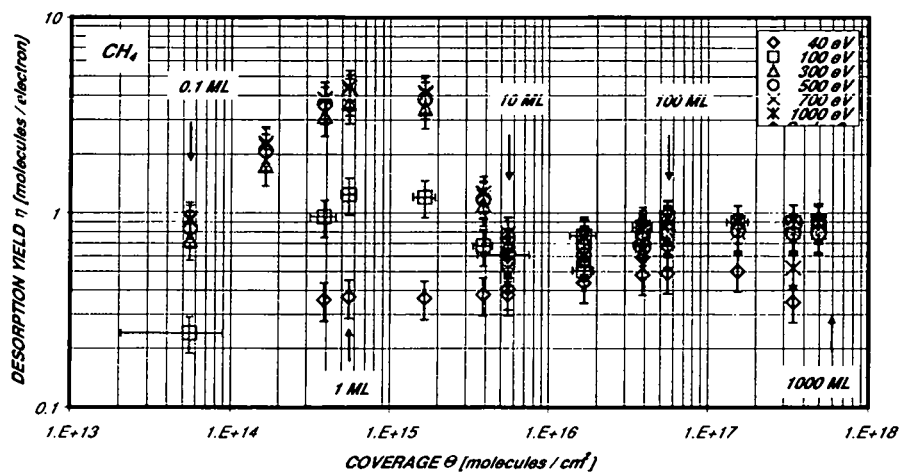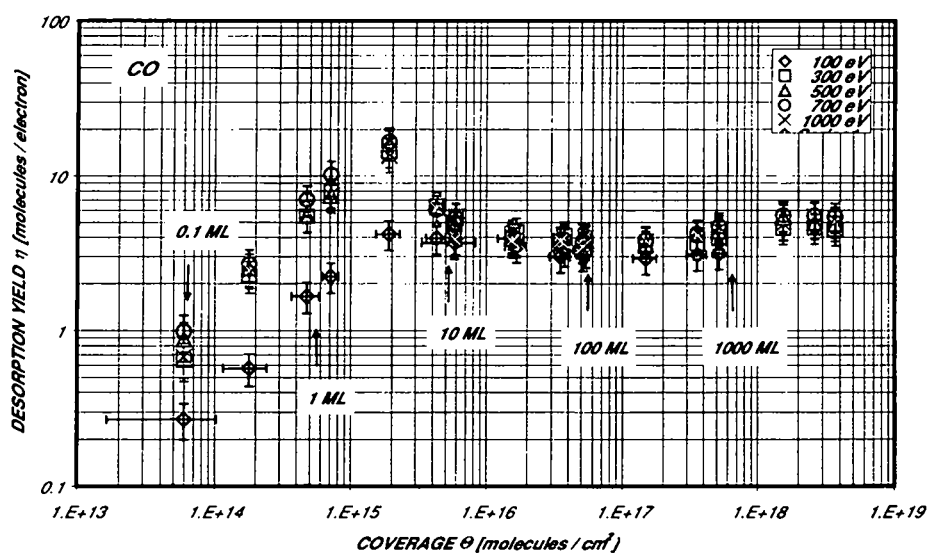Figure 4.28: The desorption yield of Ar as a function of Ar coverage at different electron energies.
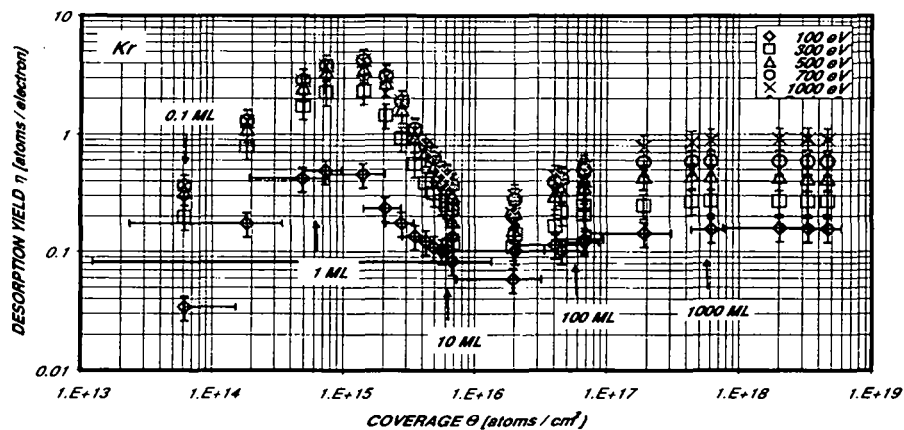
Figure 4.29: The desorption yield of Kr as a function of Kr coverage at different electron energies.
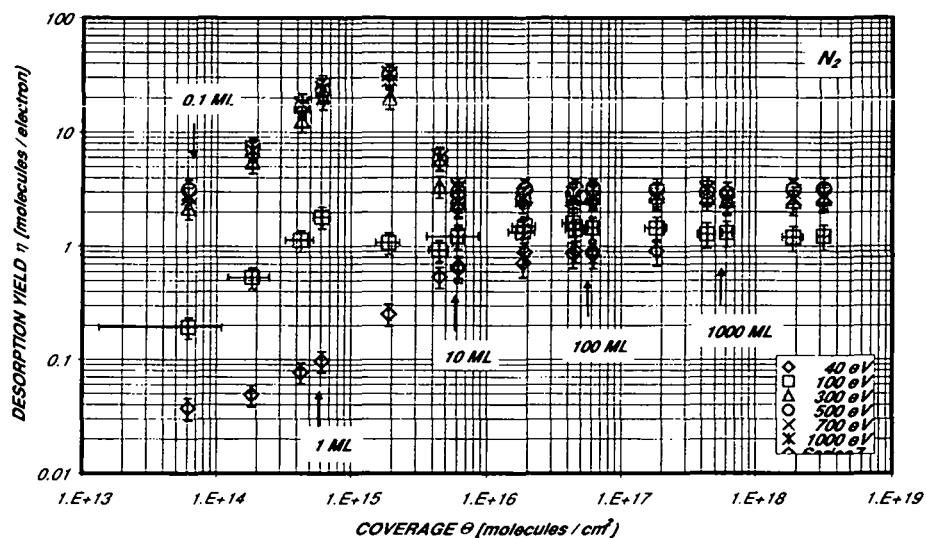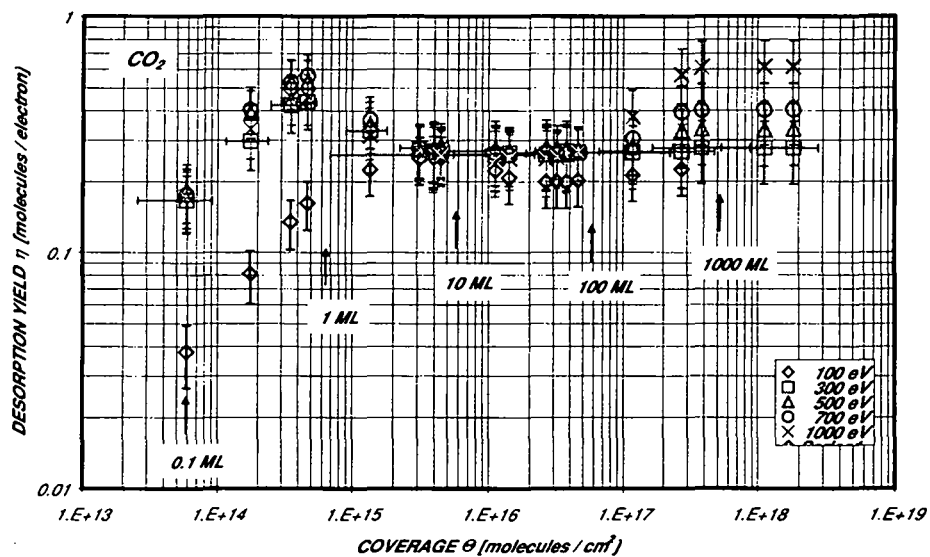
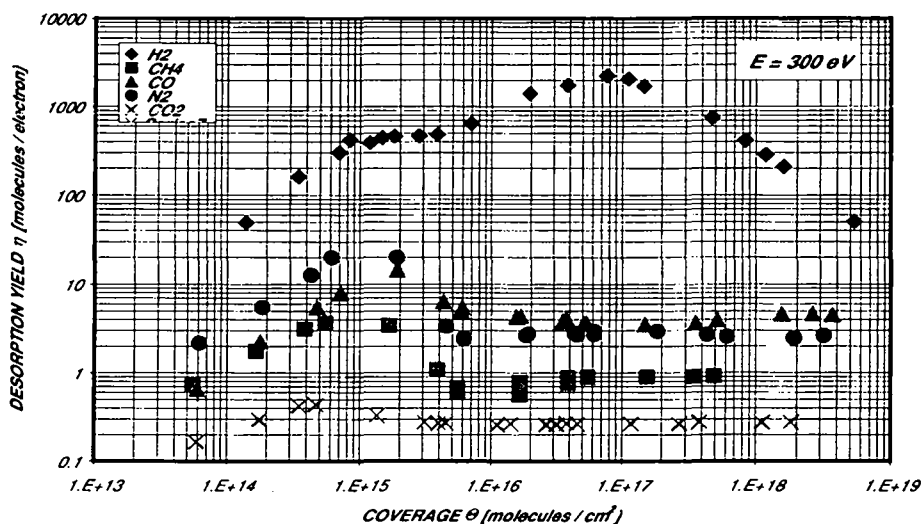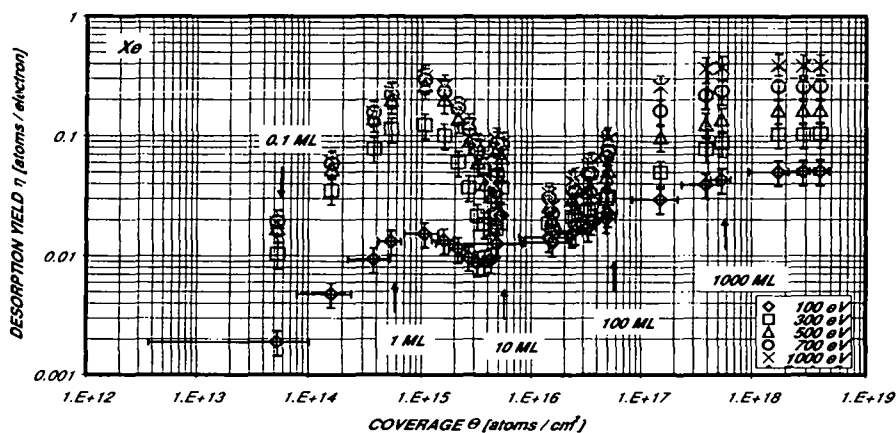Figure 4.30: The desorption yield of Xe as a function of Xe coverage at different electron energies.
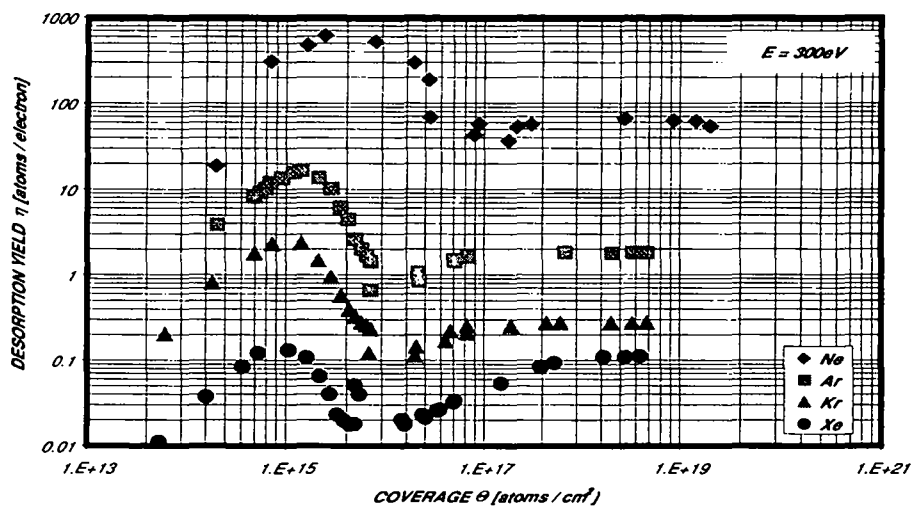
Figure 4.31: The desorption yield of noble gases as a function of the gas coverage at an electron energy of 300 eV.

67
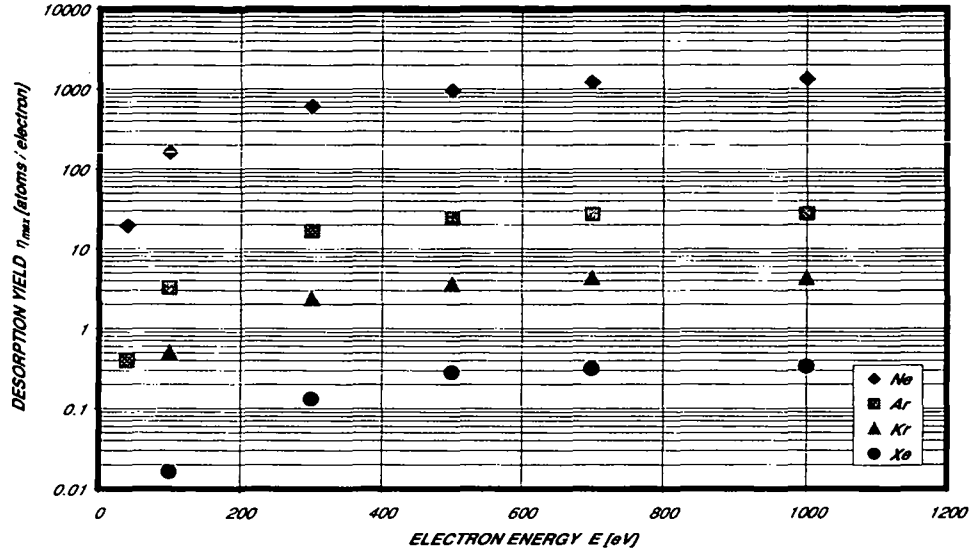
Figure 4.32: The desorption yield of noble gases as a function of the electron energy.

a coverage greater than 10^{18} atom $\cdot$ cm^{-2}. Figure 4.32 shows the evolution of the desorption yields for the same gases as a function of the electron energy for a low coverage, corresponding to the first peak of desorption in figure 4.31 i. e. a coverage of $\sim 10^{15}$ atom $\cdot$ cm^{-2}. Figure 4.33 shows the variation of the normalised desorption yields ($\eta_N = \eta(E)/\eta(1000\ eV)$) in the case of low coverage ($\sim 10^{15}$ atom $\cdot$ cm^{-2}) and in the case of a high coverage ($\sim 10^{18}$ atom $\cdot$ cm^{-2}). This curve shows a linear increase of η_N with the energy at low coverage and a much stronger dependence of η_N on the energy for high coverage.

The desorption yields obtained for a thick coverage are in good agreement with those obtained by Adachi et al [108] in the case of Kr and with those of Schou [109] for Ne. In the case of thick Ar layer Moog et al. [75] give a cross section of 4×10^{-16} cm^2 to be compared to our measurement of 6×10^{-17} cm^2.

Desorption yields of gas mixtures

In LHC, the gases desorbed by the energetic particles impinging on the beam screen will re-condense as a mixture on the beam screen. Hence it is needed, in order to predict the gas density during operation, to know the desorption
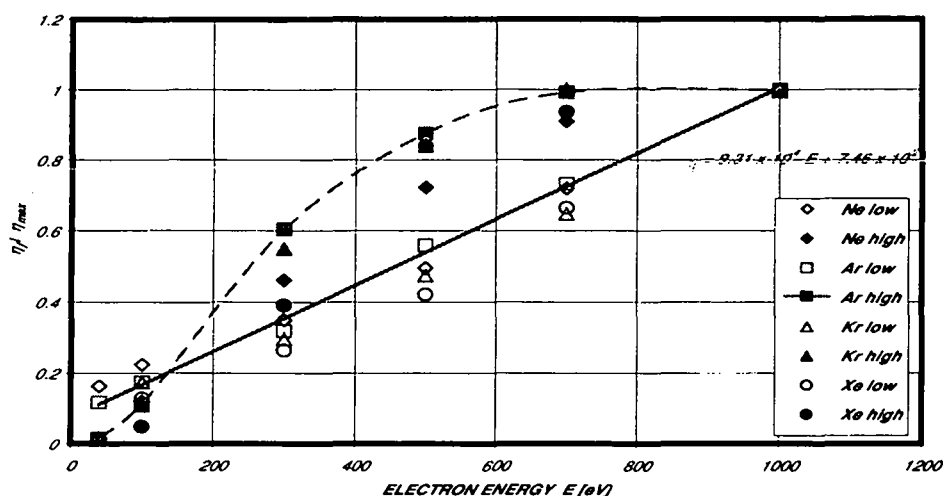
Figure 4.33: The normalised desorption yield of noble gases as a function of the electron energy. Curves labelled "low": coverage at 10^{15} atom $\cdot$ cm^{-2}; curves labelled "high": coverage at 10^{17} atom $\cdot$ cm^{-2}.

yield of the various gases (H_2, CH_4, CO, CO_2) not only when condensed as a pure gas but also when present as part of a mixture. Two mixtures were investigated: the first one is an equimolecular mixture of the four gases (25 % atomic of each gases), the second one closer to the expected gas composition on the beam screen during operation, has the following atomic composition: H_2: 0.8 %, CH_4: 2.3 %, CO: 6.2 %, CO_2: 90.7 %. The desorption yields of these different gases are shown on figure 4.34, 4.35, 4.36, 4.37,

as a function of the coverage of each individual gas (i.e. the number of molecule of the corresponding gas condensed per unit area on the sample) for the pure gases and the two mixtures. These curves show an important reduction of the desorption yields for the gases having high η like H_2 or CH_4 as well as a modification of their shapes at low coverages.

69
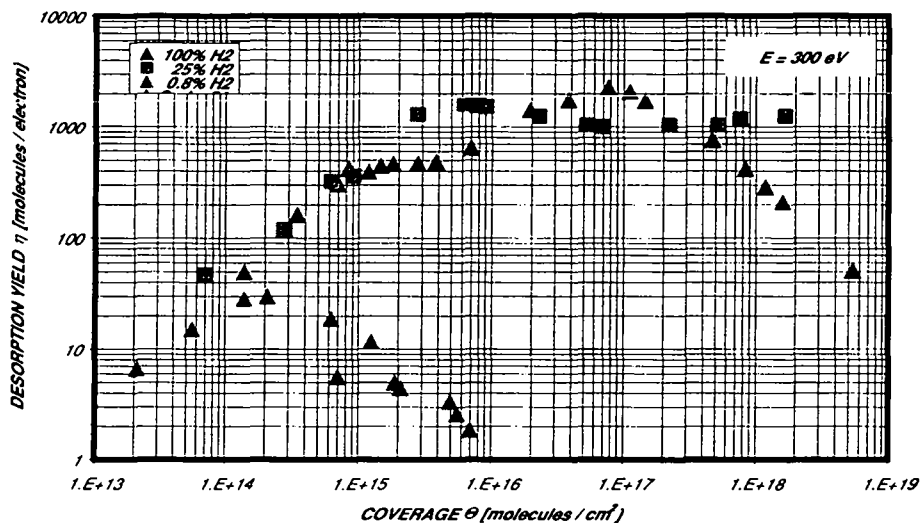
Figure 4.34: The H_2 desorption yield as a function of H_2 coverage for different condensed gas composition at an electron energy of 300 eV.
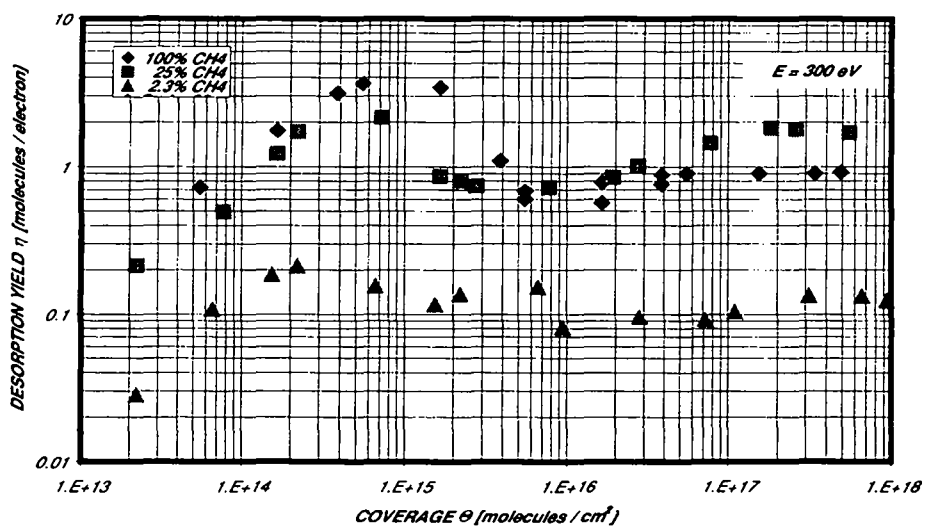
Figure 4.35: The CH_4 desorption yield as a function of CH_4 coverage for different condensed gas composition at an electron energy of 300 eV.
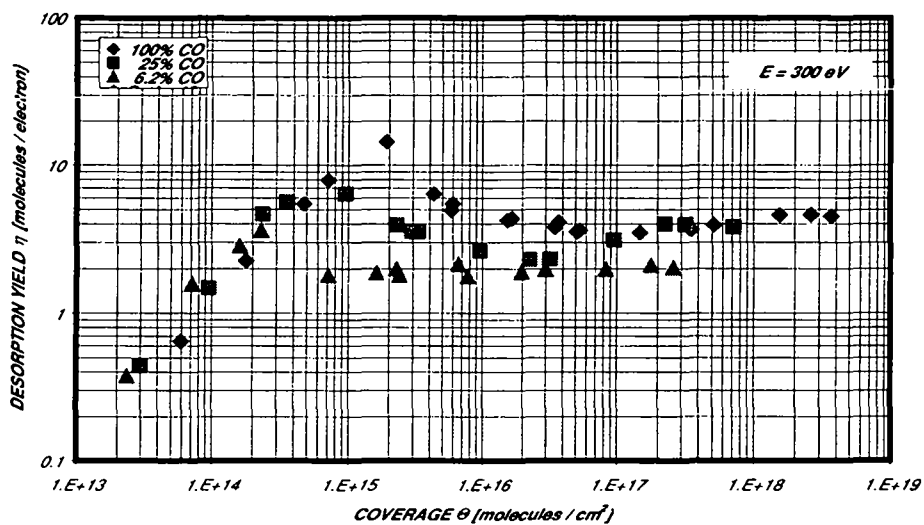
Figure 4.36: The CO desorption yield as a function of CO coverage for different condensed gas composition at an electron energy of 300 eV.
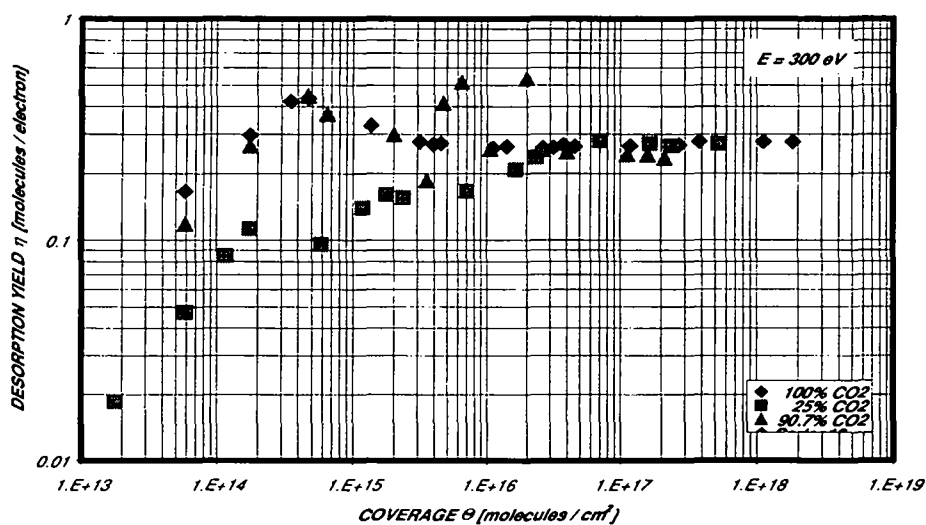
Figure 4.37: The CO_2 desorption yield as a function of CO_2 coverage for different condensed gas composition at an electron energy of 300 eV.

71

Chapter 5

Discussion of results

5.1 Sticking probability

For an average sticking probability and coverage, the maximum error is made up from the conductance $C \sim 2\%$, the condensation area A may have an error of $\sim 10\%$ and the gauge sensitivity is known to $s_G \sim 20\%$. This yields a maximum total error in s and Θ of $\sim 30\%$.

The departure of s from unity could be attributed [110], [111] to the inefficiency of energy transfer to the surface, as in accommodation coefficient theory. Two experimental factors militate against this, however. (i) An impinging molecule will be accommodated into the precursor state if only the transitional energy component normal to surface is transferred to the surface; unaccommodated translational energy parallel to the surface will simply cause the molecule to "skid" across the surface, thus allowing further opportunities for this translational component to be lost. A grazing incidence gas molecule, with a small perpendicular translational energy component, would therefore be more easily accommodated to the surface than a gas molecule normally incident. (ii) At 4.2 K, s was found to be accurately independent of surface coverage on copper films up to very high coverages.

It is well known, however, that the accommodation coefficient of rare gases on metal surfaces *increases* as the metal surface is covered with a chemisorbed layer [112]; energy transfer to a surface oscillator of similar mass to the impinging molecule is more efficient than transfer to a heavy surface metal atom. It might therefore be expected that at low temperatures, where extensive migration occurs in the precursor state, the sticking probability would *increase* with increasing coverage. This phenomena could not be verified in our experiment. Two other factors may contribute to the non-unity value of

72

s: (i) successful collisions require a particular rotational orientation of the molecule on impact; (ii) molecules impinging on certain inactive surface regions, fractionally $(1 - s)$ of the surface, are not adsorbed into the precursor state.

5.2 Desorption yields of Rare gases

The electron- and ion-induced desorption yield of condensed rare gases has been studied extensively by J. Schou and co workers [87], [107], [109], [113] for film thicknesses larger than 10^{16} atom $\cdot$ cm^{-2} and electron energy in the keV region. As stated above, our study is more focused on the low coverage and low electron energy region. The variation of with the gas coverage exhibit, for low coverage ($\sim 10^{15}$ atom $\cdot$ cm^{-2}), a pronounced peak followed by a decrease and a stabilisation for coverages above 2×10^{17} atom $\cdot$ cm^{-2}. This behaviour is in agreement with measurements by Schou et al [109] on Ne for coverage above 10^{16} atom $\cdot$ cm^{-2}. For thick coverage ($> 10^{17}$ atom $\cdot$ cm^{-2}) η (~ 60 for 300 eV electrons) is also in good agreement with those given in [109].

The desorption yields show, for most of the pure gases a pronounced peak for a coverage around 10^{15} molecule or atom $\cdot$ cm^{-2}. In this coverage range, close to the monolayer for each gas, the adsorbed layer is transparent to the incoming electrons and the electron energy is deposited in the subjacent copper. As a consequence, the flux of energy from the copper to the adsorbed layer is constant and independent of the condensed gas. The desorption yield for gases having similar type of bond and desorption mechanism, e.g. rare gases, should hence depend only on their binding energy. Figure 5.1 shows the variation of the peak desorption yield of rare gases as a function of their sublimation enthalpy (H_{sub}) [87] fitted to the equation:

$$\eta = \eta_0 \, e^{-\frac{H_{sub}}{kT}} \qquad (5.1)$$

where T is the temperature of the target as the result of beam heating. One can get T from equation 5.1 and the values for different electron energies are given in table C.8 in appendix 4. The cross section (σ) for electron induced desorption can be calculated from our data using the expression:

$$\eta = \Theta \cdot \sigma \qquad (5.2)$$

For thick coverages, exceeding the penetration depth of the electrons in the considered gas, the coverage (Θ) has been taken equal to the range of the

73
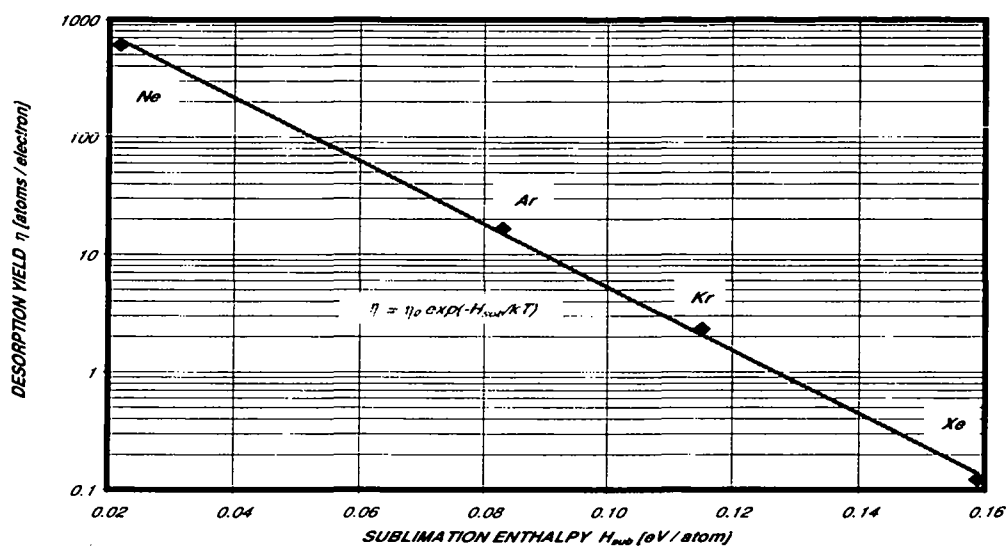
Figure 5.1: The desorption yield of rare gases as a function of their sublimation enthalpy at an electron energy of 300 eV.
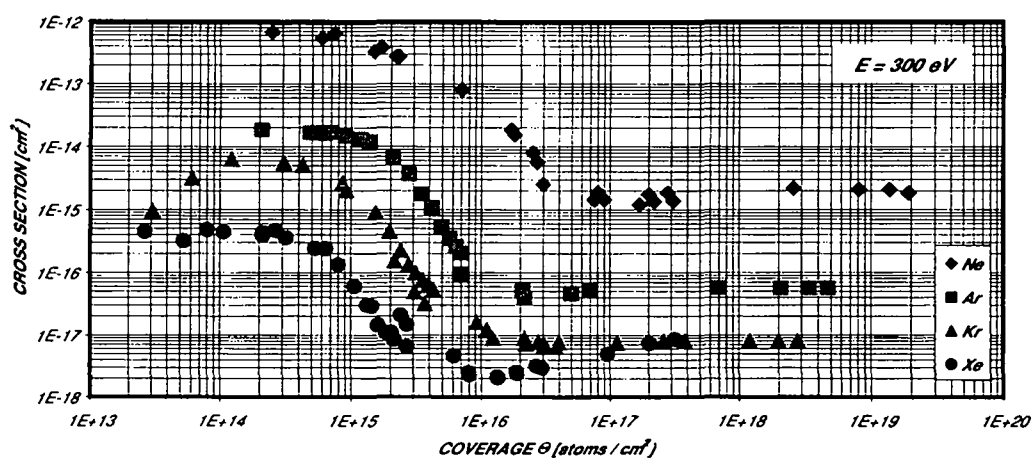
Figure 5.2: The desorption cross section of rare gases as a function of the gas coverage at an electron energy of 300 eV.

electrons in that gas. The variation of the cross section (σ) with the coverage is shown in figure 5.2 for electrons (300 eV energy) indicating clearly an important change between a coverage of 10^{15} and 10^{17} atom $\cdot$ cm^{-2}. This modification reflects a change in the desorption process and can possibly be explained the following way: The desorption from a thin film can be decomposed in two fractions: the first one (η_L) originates from the energy deposited by the electron beam in the layer and the second (η_S) from the energy dissipated in the substrate. At low coverage, the amount of energy (coming from the copper substrate) available for desorption is constant and the coverage increase leads to a regular raise of the desorption yield. For thicker layer, an increasing fraction of the energy reflected from the copper substrate is absorbed in the layer leading to a decrease of η_c and a concomitant enhancement of η_L. Finally when all the energy of the electron is absorbed in the layer (for thicknesses between 10^{16} and 6×10^{16} atom $\cdot$ cm^{-2}), η stabilises to a constant value, characteristic of the rare gas solid.

5.3 Desorption yields of gas mixtures

The most marked effect is seen in the case of hydrogen. For the 0.8 % mixture, the highest yield is obtained at a hydrogen coverage of approximately 10^{14} molecule $\cdot$ cm^{-2} corresponding to the maximum of desorption of the leading gas CO_2. In the case of CO_2, CO and CH_4 the desorption yields for thick layers are not affected for mixtures between 100 % and 25 %. For thinner coverage the presence of other gases reduces, at constant coverage of the desorbed gas, the desorption yield. Such an effect, due to the presence of impurities was also noted in the case of rare gases [109].

Part III

Application to the LHC Beam Vacuum System

Chapter 6

Prediction for the beam related dynamic vacuum effects

The requirements for the beam vacuum are stringent, driven by the requested beam lifetime and background to the experiments. Rather than quoting equivalent pressures at room temperature, the requirements at cryogenic temperature are expressed as gas densities and normalised to hydrogen taking into account the ionisation cross sections for each gas species. Equivalent hydrogen gas densities should remain below 10^{15} $H_2 \cdot m^{-3}$ to ensure the required 100 hours beam lifetime [14]. In the interaction regions around the experiments the densities should be below 10^{13} $H_2 \cdot m^{-3}$ to minimise the background to the experiments [114]. The requirements for the room temperature part are driven by the background to the experiments as well as by the beam lifetime and call for a value in the range from 10^{-8} to 10^{-9} Pa (10^{-10} and 10^{-11} mbar).

A number of dynamic phenomena have to be taken into account for the design of the beam vacuum system. Synchrotron radiation will hit the vacuum chambers in particular in the arcs; electron clouds (multipacting) could affect almost the entire ring. Extra care has to be taken during the design and installation to minimise these effects, but conditioning with beam will be required to reach nominal performance.

The LHC presents several original requirements with respect to classical vacuum systems. It has to provide adequate beam lifetime in a cryogenic system, where heat input to the 1.9 K helium circuit must be minimised and where significant quantities of gas can be condensed on the vacuum chamber.

In the cold part of the LHC vacuum system, running at 1.9 K, all gases except hydrogen have a low enough vapour pressure ($4 \cdot 10^{-13}$ Pa for CO at 20 K)

when condensed on the beam screen surface, as long as the beam screen surface is kept at a temperature below 20 K. Hydrogen will be pumped on the 1.9 K surface of the cold bore through the pumping slots of the beam screen. The strong dynamic effects that the LHC vacuum system will experience, as well as the usage of "saturable" pumping elements like NEG or cryosorbers, impose some running-in and operational constraints.

During the start up of LHC, some period(s) will be dedicated to the necessary preparation of the beam screen surfaces in order to reach LHC nominal performance. This preparation is obtained by the impact of energetic particles on the beam screen surface and consists:

- In a reduction of the number (primary desorption yield, PDY) of tightly bound molecules released per incident particle (photon or electron) called beam scrubbing

- In a reduction of the number of secondary electron (secondary electron yield, SEY) or photoelectron released per incident electron or photon called beam conditioning

During this period, gas previously tightly bound to the beam screen material will be released (primary desorption) and subsequently condensed partly on the beam screen, partly on the cold bore (through the pumping slots). The fraction condensed on the beam screen is directly exposed to the impact of the energetic particles created and/or accelerated by the beam and is hence submitted to redesorption (recycling) described by the condensed gas desorption yield (CDY).

In this work, experimental data have been collected concerning the CDY under electron bombardment of various gases condensed on a copper substrate.

Using these data, this thesis gives an input to evaluate, under realistic operation and calculation conditions, the beam lifetime in the LHC arcs as a function of operation time under electron cloud conditions. In order to evaluate this beam lifetime, several experimental inputs have to be taken into account, where CDY is one of this input.

Physical description and relevant equations

The dynamic of the gas evolution in a cold system has been described in [115]. For this discussion, it is considered that LHC operate under such conditions that an electron cloud is present generating an intense bombardment (corresponding to a heat load of 1 W/m/aperture) of the beam screen by

78

electrons with a mean energy of 100 eV. The calculation of the beam lifetime requires to evaluate the pressure evolution during the conditioning process and hence to consider all mechanisms leading to gas creation/exchange in the LHC cold vacuum system. These various processes have been reviewed in the references [116], [119]. In the present case, the main "external" gas source is due to the intense electron bombardment generated by the electron cloud

$$Q_p = \eta_p \ N_{e^-} , \tag{6.1}$$

where:

- Q_p is the number of tightly bound molecules released of the beam screen per second per cm^2

- η_p is the desorption yield of tightly bound molecules under electron impact

- N_{e^-} is the number of impinging electrons per second per cm^2

This gas condenses on the beam screen and can be re-desorbed by the electron impact

$$Q_c = \eta_c \ N_{e^-} \tag{6.2}$$

where:

- Q_c is the number of condensed (physisorbed) molecules released from the beam screen per second per cm^2

- η_c is the desorption yield of condensed gases under electron impact, which is a function of the condensed gas coverage.

The variations of the gas density and of the coverage on the beam screen are given by the following set of equations where B(T) is the isothermal equilibrium pressure for

$$V\frac{\partial N}{\partial t} = A_{BS}N_{e^-}(\eta_p + \eta_c) - Kp(s \ A_{BS} + A_h) + KB(T)A_{BS} \tag{6.3}$$

$$\frac{V}{A_{BS}}\frac{\partial N}{\partial t} = N_{e^-}(\eta_p + \eta_c) - Kp(s + \frac{A_h}{A_{BS}}) + KB(T) \tag{6.4}$$

$$A_{BS}\frac{\partial \Theta}{\partial t} = Kp \ s \ A_{BS} - N_{e^-} \ \eta_c A_{BS} - KB(T)A_{BS} \tag{6.5}$$

$$\frac{\partial \Theta}{\partial t} = Kp \ s - N_{e^-} \ \eta_c - KB(T) \tag{6.6}$$

79

the gas concerned. Where

$$K = \frac{1}{kT}\frac{\bar{v}}{4} \tag{6.7}$$

with k the Boltzmann constant, T the temperature on the beam screen and $\bar{v}$ the average mean velocity of the molecules and

$$p = NkT. \tag{6.8}$$

V is the volume of the beam screen per unit length, p the pressure, s the sticking probability, A_{BS} and A_h the area (cm^2) per unit length of the beam screen and of the pumping holes of beam screen.

After some period of operation, an equilibrium pressure (p_{eq}) and coverage (Θ_{eq}) can be reached when the net quantity of gas entering the system (primary desorption) equals the amount Q_h leaving through the pumping holes

$$A_h \; Q_h = A_h \; p_{eq} \; K. \tag{6.9}$$

$$Q_h = p_{eq} \; K. \tag{6.10}$$

When this equilibrium is reached, the coverage of the beam screen is such that the amount of molecules sticking per unit area and unit time is equal to the amount of condensed molecules desorbed from the beam screen surface.

It should be noted that separate equilibrium can also be reached for the pressure and the coverage, depending on the relation η_c versus Θ. The origin and consequences of this situation are discussed as follows: In previous calculation, the desorption yield of condensed layer has been considered to increase linearly with the coverage. The measurements in this work have shown that for thick layers the desorption yield tends to a limit.

In the present case these molecules are mainly released by the electron impact and the subsequent calculation will show that the contribution of the static pressure can be neglected in that case. The equilibrium coverage is linked to the equilibrium pressure by the following relation

$$K \; p_{eq} - N_{e^-} \; \eta_c(\Theta_{eq}) = 0. \tag{6.11}$$

That equilibrium is only reached if a sufficient number of molecules is liberated by the primary desorption during the conditioning process.

Figure 6.1 shows the ratio between primary desorption and desorption of condensed gas as a function of the electron dose. One can see that at a certain value of electron dose the ratio between primary desorption and desorption of condensed gas is constant for the different gases. In this case a equilibrium

80
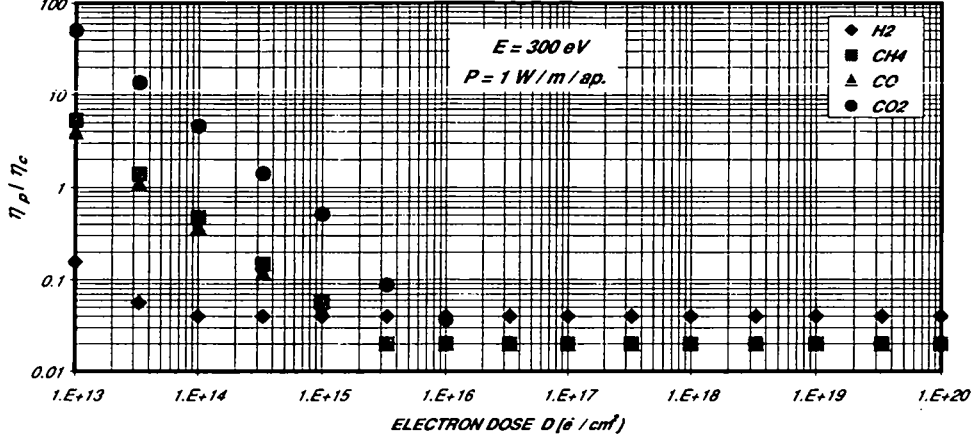
Figure 6.1: Ratio of primary desorption yield and desorption yield of condensed gas as a function of the electron dose at an electron energy of 300 eV.

is reached between primary desorption and gas molecules which go through the pumping holes of the beam screen. The pressure/gas density in the beam screen is given by

$$p(D) = N_{e^-} \frac{\eta_c(\Theta_{BS}(D)) + \eta_p(D)}{K(s + \frac{A_h}{A_{BS}})} \tag{6.12}$$

and is shown in figure 6.2. It is hence possible to calculate the evolution of the lifetime in the LHC arcs as a function of the electron dose received by the beam screen if the following input parameters are extracted from the available experimental data:

- Variation of the PDY with D

- Variation of the desorbed gas quantity with D

- Variation of the CDY with the gas coverage

The beam lifetime as a function of the electron dose is illustrated in figure 6.3.

81
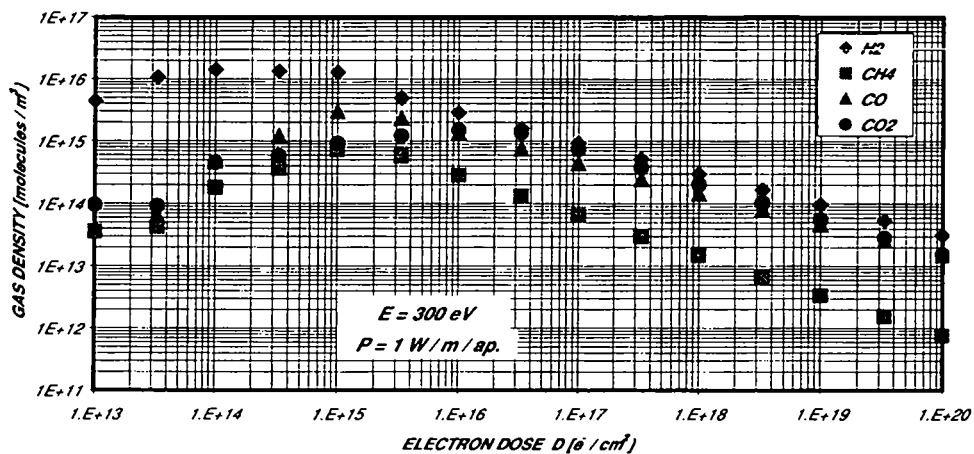
Figure 6.2: Gas density as a function of the electron dose at an electron energy of 300 eV and a temperature of 15 K.
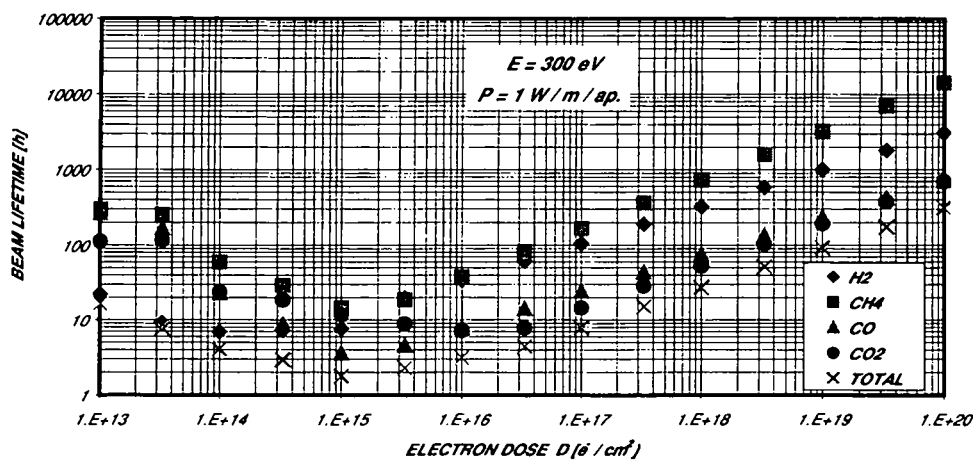
Figure 6.3: Beam lifetime as a function of the electron dose at an electron energy of 300 eV.

Chapter 7

Conclusion

This work was carried out in the vacuum group of the AT division at CERN. Its aim was to investigate the electron stimulated desorption in general and its application for the surfaces in the LHC beam vacuum system in particular.

This work has presented the desorption yields of gases condensed at liquid helium temperature on a copper surface. Thanks to the experimental set up and procedure used, allowing a simple and accurate definition of coverage and pumping speed, desorption yields can be unambiguously measured and complex effects as the influence of mixing gases, can be studied. Very large yields were measured indicating, in the case of the rare gases, a clear correlation with the gas sublimation energy. A peak in the desorption yield of pure gases appears at low coverage (close to 10^{15} atom $\cdot$ cm^{-2}, i.e. a coverage of the order of one monolayer). The study of noble gases has shown that two different mechanisms lead to desorption depending on the gas coverage. They result in two largely different cross-sections for desorption. For other gases, commonly desorbed in accelerator vacuum systems, the influence of the mixing has been determined. This mixing leads to a reduction, at constant coverage, of the desorption yields compared to those measured on pure condensed gases for the coverage range of interest in LHC.

Appendix A

Fundamental physical constants

The numerical values of the fundamental physical constants are taken from [117], page 1808.

Quantity		Value
c	speed of light in vacuum	$299\ 792\ 458$ m $\cdot$ s^{-1}
μ_0	magnetic constant ($4\ \pi\ 10^{-7}$)	$12.566\ 470\ 614\ldots \times 10^{-7}$ N $\cdot$ A^{-2}
ϵ_0	electric constant ($\frac{1}{\mu_0 c^2}$)	$8.854\ 187\ 817\ldots \times 10^{-12}$ F $\cdot$ m^{-1}
h	Planck constant	$6.626\ 068\ 76(52) \times 10^{-34}$ J $\cdot$ s
$\hbar$	reduced Planck constant ($\frac{h}{2\pi}$)	$1.054\ 571\ 596(82) \times 10^{-34}$ J $\cdot$ s
e	elementary charge	$1.602\ 176\ 462(63) \times 10^{-19}$ C
α	fine structure constant ($\frac{e^2}{4\pi\epsilon_0 \hbar c}$)	$7.297\ 352\ 533(27) \times 10^{-3}$
k	Boltzmann constant	$1.380\ 650\ 3(24) \times 10^{-23}$ J $\cdot$ K^{-1}
N_A	Avogadro constant	$6.022\ 141\ 99(47) \times 10^{23}$ mol^{-1}
R	molar gas constant	$8.314\ 472(15)$ J $\times$ mol^{-1} K^{-1}
m_e	electron mass	$9.109\ 381\ 88(72) \times 10^{-31}$ kg
m_p	proton mass	$1.672\ 621\ 58(13) \times 10^{-27}$ kg
u	atomic mass unit ($\frac{1}{12}m(^{12}C)$)	$1.660\ 538\ 73(13) \times 10^{-27}$ kg

Appendix B

Some LHC design parameters

The values in this table, taken from [5], apply if LHC is operated with protons at nominal, or collision energy.

Parameter	Value	Unit
Proton energy at collision (nominal energy)	7	TeV
Relativistic factor	7461	
Ring circumference	26658.883	m
Revolution frequency	11.2455	kHz
Bunch spacing	7.48	m
Bunch separation	24.95	ns
Number of available bunch places	3564	
Number of bunches	2835	
Number of protons per bunch	1.05×10^{11}	
R.m.s. x,y beam size in the arc	0.303	mm
R.m.s. x,y beam size at interaction points	15.9	μm
R.m.s. bunch length	7.7	cm
R.m.s. bunch length	0.257	ns
Circulating beam current	0.536	A
Stored energy per beam	334	MJ
Expected luminosity	1.00×10^{34}	$cm^{-1} \cdot s^{-1}$
Main bending magnets (dipoles)		
Number of main dipoles	1232	
Magnetic length per dipole	14.2	m
Bending radius	2784.32	m
Nominal field	8.386	T
Synchrotron radiation in main dipoles		
Instantaneous power loss per proton	1.84×10^{-11}	W
Energy loss of a proton per turn	6.71	keV
Critical photon energy	44.1	eV
Number of emitted photons per unit time per proton	8.46×10^6	s^{-1}
Synchrotron radiation power per unit length	0.206	$W \cdot m^{-1}$

Appendix C

ESD experiment: settings and calibration data

This appendix summarises the numerical values of the parameters required to calculate the molecular desorption yield in chapter 4.

	300 K		4.2 K	
	$S \, [\text{l} \cdot \text{s}^{-1}]$	$S \, [\text{m}^3 \cdot \text{s}^{-1}]$	$S \, [\text{l} \cdot \text{s}^{-1}]$	$S \, [\text{m}^3 \cdot \text{s}^{-1}]$
H_2	143.17	1.43×10^{-1}	670.94	6.71×10^{-1}
CH_4	107.57	1.08×10^{-1}	532.54	5.33×10^{-1}
Ne	105.70	1.06×10^{-1}	394.45	3.95×10^{-1}
CO	94.58	9.46×10^{-2}	437.02	4.37×10^{-1}
N_2	93.76	9.38×10^{-2}	419.96	4.20×10^{-1}
Ar	86.30	8.63×10^{-2}	366.23	3.66×10^{-1}
CO_2	83.23	8.32×10^{-2}	439.84	4.40×10^{-1}
Kr	59.87	5.99×10^{-2}	247.75	2.48×10^{-1}
Xe	29.29	2.93×10^{-2}	202.17	2.02×10^{-1}

Table C.1: Effective pumping speed at a sample temperature of 300 K and 4.2 K

Gauge 4	Gauge 15	mass spectrometer
$I_e^* = 0.1$ mA	$I_e^* = 4$ mA	$I_e = 1$ mA

Table C.2: Emission current of the Bayard Alpert gauges and the quadrupole mass spectrometer

	Gauge 4		Gauge 15	
	s^* [torr^{-1}]	s^* [Pa^{-1}]	s^* [torr^{-1}]	s^* [Pa^{-1}]
H_2	19.27	1.45×10^{-1}	19.80	1.49×10^{-1}
CH_4	70.46	5.28×10^{-1}	66.34	4.98×10^{-1}
Ne	15.73	1.18×10^{-1}	15.73	1.18×10^{-1}
CO	41.05	3.08×10^{-1}	42.51	3.19×10^{-1}
N_2	39.85	2.99×10^{-1}	40.26	3.02×10^{-1}
Ar	51.40	3.86×10^{-1}	51.07	3.83×10^{-1}
CO_2	45.26	3.39×10^{-1}	54.41	4.08×10^{-1}
Kr	65.06	4.88×10^{-1}	65.06	4.88×10^{-1}
Xe	83.79	6.28×10^{-1}	83.79	6.28×10^{-1}

Table C.3: Absolute sensibilities of the Bayard Alpert gauges

	H_2	CH_4	Ne	CO	N_2	Ar	CO_2	Kr	Xe
s'	1.000	0.3879	0.1224	0.3612	0.4416	0.1362	0.1855	0.0418	0.0057

Table C.4: Sensibilities relative to H_2^+ of the quadrupole mass spectrometer

M/Z	H_2	CH_4	Ne	CO	N_2	Ar	CO_2	Kr	Xe
1	0.0352								
2	1.0000								
10			0.0160						
12		0.1415		0.1477			0.3027		
13		0.1108							
14		0.2046			0.2496				
15		0.8717							
16		1.0000		0.1089			0.4320		
17		0.0071							
20			1.0000			0.2446			
22			0.0900				0.0295		
28				1.0000	1.0000		0.3240		
29				0.0284	0.0063				
40						1.0000			
41								0.0749	
42								0.3631	
43								0.1030	
44							1.0000		
45							0.0120		
46							0.0043		
64									1.0000
65									0.8292
66									0.9796
67									0.3689
68									0.3100
78								0.0044	
80								0.0408	
82								0.2203	
83								0.2237	
84								1.0000	
86								0.2924	

Table C.5: Cracking pattern of the quadrupole mass spectrometer (the numbers in the first column are approximate values for the mass-to-charge-ratio of the ions, measured in atomic mass unit per elementary charge)

T [K]	$\int_{T_0}^{T_L} \lambda\, dT$ $[W \cdot cm^{-1}]$
6	0.0063
8	0.0159
10	0.0293
15	0.0816
20	0.163
25	0.277
30	0.424
35	0.607
40	0.824
50	1.35
60	1.98
70	2.7
76	3.17
80	3.49
90	4.36
100	5.28
120	7.26
140	9.39
160	11.7
180	14.1
200	16.6
250	23.4
300	30.6

Table C.6: Thermal conductivity integrals for stainless steel.

	T_C [K]	A [cm^2]
H_2	3.7	31.59
CH_4	32.0	43.29
Ne	7.3	31.79
CO	26.7	39.24
N_2	23.7	36.59
Ar	26.8	39.27
CO_2	76.1	113.75
Kr	36.8	48.11
Xe	50.8	67.09

Table C.7: Condensation temperatures and areas for different gases.

E [eV]	T_B [K]
100	174
300	187
500	194
700	192
1000	191

Table C.8: Target temperature as a result of the beam for different electron energies E.

Appendix D

Calculation of partial pressures from gauge and mass spectrometer data

The procedure which is described in this chapter has been used in this work to calculate partial pressures and their variances from gauge and mass spectrometer data. It is based on a procedure frequently used in data analysis, the so-called *chi-square minimisation*, as described in [121], chapter 14.

If we consider a gas mixture consisting of J species, we have $J+1$ unknowns, which are the partial pressures p_j $(j = 1 \ldots J)$ and the reference sensibility of the mass spectrometer s_{ref}. Hence, we need at least $J+1$ equations to determine partial pressures of J species. These equations have to be provided by means of measurement. Since one equation results from the signal of the total pressure gauge, at least J different measurements are needed for different settings M/Z of the mass spectrometer. The system of equations is then given by

$$I_{m_1}^+ = I_e \; s_{ref} \; \sum_{j=1}^{J} s_j' \; x_{m_1,j} \; p_j$$

$$I_{m_2}^+ = I_e \; s_{ref} \; \sum_{j=1}^{J} s_j' \; x_{m_2,j} \; p_j$$

$$\vdots \qquad\qquad\qquad\qquad\qquad\qquad (D.1)$$

$$I_{m_N}^+ = I_e \; s_{ref} \; \sum_{j=1}^{J} s_j' \; x_{m_N,j} \; p_j$$

$$I^* = I_e^* \; \sum_{j=1}^{J} s_j^* \; p_j$$

where N is the number of measurements from the mass spectrometer ($N \geq J$). $I_{m_i}^+$ are the signals from the mass spectrometer at $M/Z = m_i$, I_e the emission current, s_j' the relative sensibilities for species j, and $x_{m_{i,j}}$ the cracking pattern for species j at $M/Z = m_i$. I^* is the signal from the total pressure gauge, I_e^* the emission current of the gauge, and s_j^* are the absolute sensibilities of the gauge for species j. With the definitions

$$y_i = \frac{I_{m_i}^+}{I_e}, \tag{D.2}$$

$$a_j = s_{ref}\ p_j, \tag{D.3}$$

and

$$X_{i,j} = s_j'\ x_{m_{i,j}}, \tag{D.4}$$

equations D.1 can be rewritten as

$$y_i = \sum_{j=1}^{J} X_{i,j}\ a_j; \quad i = 1\dots N \tag{D.5}$$

and

$$s_{ref} = \frac{I_e^*}{I^*} \sum_{j=1}^{J} s_j^*\ a_j. \tag{D.6}$$

If $N > J$ the system of equations D.5 is overdetermined and in general does not have a solution in a mathematical sense. Hence, we have to find the most likely values for a_j by some estimation. The mathematical means to do this is given by the chi-square minimisation. The χ^2 for D.5 is given by

$$\chi^2 = \sum_{i=1}^{N} \frac{\left(y_i - \sum_{j=1}^{J} X_{i,j}\ a_j\right)^2}{\sigma^2(y_i)}. \tag{D.7}$$

$\sigma^2(y_i)$ is the variance of y_i which has to be determined from measurement. From equation D.2, it follows from the law of propagation of uncertainties that

$$\frac{\sigma^2(y_i)}{y_i^2} = \frac{\sigma^2(I_{m_i}^+)}{(I_{m_i}^+)^2} + \frac{\sigma^2(I_e)}{(I_e)^2} \tag{D.8}$$

with $\sigma^2(I_{m_i}^+)$ and $\sigma^2(I_e)$ being the (measured) variances of $I_{m_i}^+$ and I_e, respectively.

Finding the minimum of χ^2 with respect to the parameters a_j is mathematically equivalent to solving the vector matrix equation

$$\tilde{\alpha} \cdot \vec{a} = \vec{\beta} \tag{D.9}$$

95

if the square matrix $\tilde{\alpha}$ and the vectors $\vec{a}$ and $\vec{\beta}$ are given by

$$\tilde{\alpha} = \begin{pmatrix} \alpha_{1,1} & \cdots & \alpha_{1,J} \\ \vdots & \ddots & \vdots \\ \alpha_{J,1} & \cdots & \alpha_{J,J} \end{pmatrix}, \vec{\beta} = \begin{pmatrix} \beta_1 \\ \vdots \\ \beta_J \end{pmatrix}, \vec{a} = \begin{pmatrix} a_1 \\ \vdots \\ a_J \end{pmatrix} \tag{D.10}$$

with the definitions

$$\alpha_{k,j} = \sum_{i=1}^{N} \frac{X_{i,j} X_{i,k}}{\sigma^2(y_i)} \tag{D.11}$$

and

$$\beta_k = \sum_{i=1}^{N} \frac{y_i X_{i,k}}{\sigma^2(y_i)}. \tag{D.12}$$

Hence, values of a_j that minimise χ^2 in equation D.7 are given by the solution of equation D.9

$$\vec{a} = \tilde{\alpha}^{-1} \cdot \vec{\beta}. \tag{D.13}$$

Besides of getting a mathematically well justified estimation of the parameters a_j (i.e. the so-called *maximum likelihood estimation*), the method of chi-square minimisation has also the huge advantage to give estimations for the variances (and covariances) of the parameters a_j , from which we can estimate the variances of the partial pressures p_j. The estimated variances of a_j are given by the main diagonal elements of inverse matrix $\tilde{\alpha}^{-1}$ and the covariances by the off-diagonal elements of $\tilde{\alpha}^{-1}$, hence

$$Cov(a_j, a_k) = (\tilde{\alpha}^{-1})_{j,k}. \tag{D.14}$$

and

$$\sigma^2(a_j) = Cov(a_j, a_j) = (\tilde{\alpha}^{-1})_{j,j}. \tag{D.15}$$

With the results from equation D.13, the reference sensibility s_{ref} can be directly calculated using equation D.6. The estimated variance of s_{ref} follows from the law of propagation of uncertainties (cf. [122], appendix A).

$$\frac{\sigma^2(s_{ref})}{\sigma_{ref}^2} = \frac{\sigma^2(I^*)}{(I^*)^2} + \frac{\sigma^2(I_e^*)}{(I_e^*)^2} + \frac{\sum_{j=1}^{J} \sum_{k=1}^{J} s_j^* s_k^* \, Cov(a_j, a_k)}{\left(\sum_{j=1}^{J} s_j^* a_j\right)^2} \tag{D.16}$$

Finally the partial pressures can be calculated according to equation D.3, hence

$$p_j = \frac{a_j}{s_{ref}} \tag{D.17}$$

96

and the estimated variance for p_j follows again from the law of propagation of uncertainties as

$$\frac{\sigma^2(p_j)}{p_j^2} = \frac{\sigma^2(a_j)}{a_j^2} + \frac{\sigma^2(s_{ref})}{s_{ref}^2} - 2\frac{Cov(a_j, s_{ref})}{a_j \; s_{ref}} \qquad \text{(D.18)}$$

where the covariance of a_j and s_{ref} follows from equation D.6 as

$$Cov(a_j, s_{ref}) = \sum_{k=1}^{J} \frac{\partial s_{ref}}{\partial a_k} \; Cov(a_j, a_k) = \frac{I_e^*}{I^*} \sum_{k=1}^{J} s_k^* \; Cov(a_j, a_k). \qquad \text{(D.19)}$$

Bibliography

[1] CERN - Centre Européene pour la Recherche Nucléaire, Route de Meyrin, CH - 1211 Genève 23; http://www.cern.ch.

[2] G. M. Fraser, editor. *The particle century*. Institute of Physics Publishing, Bristol, 1998.

[3] W. Noel Cottingham and Derek A. Greenwood. *An introduction to the standard model of particle physics*. Cambridge University Press, 1998.

[4] F. Gianotti. Collider physics: LHC. In A. Olchovski, editor, *7th European School of High-Energy Physics*, Casta-Papiernicka, Slovak Republic 22 August - 4 September 1999. Also published as CERN Yellow Report CERN-2000-007.

[5] LHC Study Group. The Large Hadron Collider: conceptual design. Technical Report CERN-AC-95-05, CERN, 1995.

[6] L. R. Evans. The Large Hadron Collider project. LHC Project Report 53, CERN, 1996.

[7] ATLAS collaboration. ATLAS: technical proposal for a general purpose p-p experiment at the Large Hadron Collider at CERN. Technical Report CERN-LHCC-94-43, CERN, 1994.

[8] CMS collaboretion. CMS, the Compact Muon Solonoid: Technical Proposal. Technical Report CERN-LHCC-94-38, CERN, 1994.

[9] LHCb collaboration. LHCb: Technical Proposal. Technical Report CERN-LHCC-98-004, CERN, 1998.

[10] ALICE collaboration. ALICE: technical proposal for a large ion collider experiment at the CERN LHC. Technical Report CERN-LHCC-95-71, CERN, 1995.

[11] Ph. Lebrun. Advanced Superconducting Technology for Global Science: The Large Hadron Collider At Cern. LHC Project Report 499, CERN, 2001.

[12] A. P. Verweij and L. Buchsbaum. Experimental results of current distribution in Rutherford-type LHC cables. *cryogenics*, 40: 663-670, 2000.

[13] Ph. Lebrun. Cryogenics for the Large Hadron Collider. LHC Project Report 338, CERN, 1999.

[14] O. Gröbner. Overview of the LHC vacuum system. *Vacuum*, 60(1-2): 25-34, 2001.

[15] C. Wyss. LHC arc dipole status report. In *1999 Particle Accelerator Conference*, New York City, NY, USA, 29 March - 2 April 1999.

[16] P. Fessia, D. Perini, S. Russenschuck, Ch. Voellinger, R. Vuillermet and C. Wyss. Selection of the cross-section design for the LHC main dipole. LHC Project Report 347, CERN, 1999.

[17] C. Wyss. The LHC magnet programme: From accelerator physics requirements to production in industry. In *7th European Particle Accelerator Conference* [118], pages 207-211.

[18] M. Modena, M. Bajko, L. Bottura, M. Buzio, P. Fessia, O. Pagano, D. Perini, P. Pugnat, S. Sanfilippo, F. Savary, W. Scandale, A. Siemko, G. Spigo, E. Todesco, I. Vanenkov, J. Vlogeart and C. Wyss. Final prototypes, first pre-series units and steps towards series production of the LHC main dipoles. LHC Project Report 487, CERN, 2001.

[19] B. Angerth, F. Bertinelli, J.-C. Brunet, R. Calder, F. Caspers, P. Cruikshank, J.-M. Dalin, O. Gröbner, N. Kos, A. Mathewson, A. Poncet, C. Reymermier, F. Ruggiero, T. Scholz, S. Sgobba and E. Wallén. The Large Hadron Collider Vacuum System. In *1995 Particle Accelerator Conference*, Dallas, Texas, USA, 1 - 5 May 1995.

[20] O. Gröbner. Vacuum system for LHC. *Vacuum*, 46(8-10): 797-801, 1995.

[21] O. Gröbner. The LHC vacuum system. LHC Project Report 181, CERN, 1998.

[22] O. Gröbner. LHC vacuum system. In Turner [119], pages 291-305. Also published as CERN Yellow Report CERN-99-05.

[23] Edmund Wilson. *An Introduction to Particle Accelerators*. Oxford University Press, 2001.

[24] C. Rathjen, F. Caspers, P. Pugnat, S. Russenschuck and A. Siemko. Currents in, forces on and deformation / displacements of the LHC beam screen expected during a magnet quench. LHC Project Report 489, CERN, 2001.

[25] P. Cruikshank, K. Artoos, F. Bertinelli, J.-C. Brunet, R. Calder, C. Campedel, I. Collins, J.-M. Dalin, B. Feral, O. Gröbner, N. Kos, A. Mathewson, L. Nikitina, I. Nikitine, A. Poncet, C. Reymermier, G. Schneider, I. Sexton, S. Sgobba, R. Valbuena and R. Veness. Mechanical design aspects of the LHC beam screen. LHC Project Report 128, CERN, 1997.

[26] K. Artoos, P. Cruikshank and N. Kos. Mechanical and thermal measurements on a 11 m long beam screen in the LHC magnet test string during RUN 3 A. LHC Project Note 178, CERN, 1999.

[27] F. Caspers, M. Morvillo, F. Ruggiero and J. Tan. Surface resistance measurement and estimate of the beam-induced resistive wall heating of the LHC dipole beam screen. LHC Project Report 307, CERN, 1999.

[28] F. Caspers, A. Mostacci, F. Ruggiero and L. Palumbo. Image currents in azimuthally inhomogeneous metallic beam pipes. LHC Project Report 493, CERN, 2001.

[29] O. Gröbner, A. G. Mathewson, H. Störi, P. Strubin and R. Souchet. Studies of photon induced gas desorption using synchrotron radiation. *Vacuum*, 33(7): 397-406, 1983.

[30] E. M. Williams, F. Le Normand, N. Hilleret and G. Dominichini. Studies of photo induced desorption of surface gas within an aluminium vacuum chamber using a X-ray source. *Vacuum*, 35(3): 141-148, 1985.

[31] O. Gröbner, A. G. Mathewson and P. C. Marin. Gas desorption from an oxygen free high conductivity vacuum chamber by synchrotron radiation photons. *Journal of Vacuum Science and Technology A*, 12(3): 846-853, 1994.

[32] V. V. Anashin, O. B. Malyshev, V. N. Osipov, I. L. Maslennikov and W. C. Turner. Investigation of synchrotron radiation-induced photodesorption in cryosorbing quasi-closed geometry. *Journal of Vacuum Science and Technology A*, 12(5): 2917-2921, 1994.

100

[33] V. V. Anashin, G. Derevyankin, V. G. Dudnikov, O. B. Malyshev, V. N. Osipov, C. L. Foerster, F. M. Jacobsen, M. W. Ruckmann, M. Strongin, R. Kersevan, I. L. Maslennikov, W. C. Turner and W. A. Lanford. Cold beam tube photodesorption and related experiments for the Superconducting Super Collider Laboratory 20 TeV proton collider. *Journal of Vacuum Science and Technology A*, 12(4): 1663-1672, 1994.

[34] V. Baglin, I. R. Collins, O. Gröbner, C. Grünhagel and B. Jenninger. Molecular desorption by synchrotron radiation and sticking coefficient at cryogenic temperatures for H_2, CH_4, CO and CO_2. LHC Project Report 518, CERN, 2001.

[35] R. Calder, O. Gröbner, A. G. Mathewson, V. V. Anashin, A. Dranichnikov and O. B. Malyshev. Synchrotron radiation induced gas desorption from a prototype Large Hadron Collider beam screen at cryogenic temperatures. *Journal of Vacuum Science and Technology A*, 14(4): 2618-2623, 1996.

[36] V. V. Anashin, O. B. Malyshev, R. Calder and O. Gröbner. A study of the photodesorption process for cryosorbed layers of H_2, CH_4, CO and CO_2 at various temperatures between 3 K and 68 K. *Vacuum*, 53: 269-272, 1999.

[37] V. V. Anashin, O. B. Malyshev, I. R. Collins and O. Gröbner. Photon-stimulated desorption and the effect of cracking of condensend molecules in a cryogenic vacuum system. *Vacuum*, 60(1-2): 15-24, 2001.

[38] I. R. Collins, O. Gröbner, O. B. Malyshev, A. Rossi, P. Strubin and R. Veness. Vacuum stability for ion induced gas desorption. LHC Project Report 312, CERN, 1999.

[39] O. B. Malyshev. The ion impact energy on the LHC vacuum chamber walls. In the *7th European Particle Accelerator Conference* [118], pages 951-953.

[40] Marie-Hélène Achard. Desorption des gaz induite par des electrons et des ions de l'acier inoxydable, du cuivre OFH, du titane et de l'aliminium purs. Technical Report CERN-ISR-VA/76-34, CERN, 1976.

[41] Marie-Hélène Achard, R. Calder and A. Mathewson. The temperature dependence of the electron and ion induced gas desorption coefficients of some technological materials. Technical Report CERN-ISR-VA/78-2, CERN, 1978.

[42] Marie-Hélène Achard, R. Calder and A. Mathewson. The effect of bake-out temperature on the electron and ion induced gas desorption coefficients of some technological materials. *Vacuum*, 29(2): 53-65, 1979.

[43] William C. Turner. Ion desorption stability in superconducting high energy physics proton colliders. *Journal of Vacuum Science and Technology A*, 14(4): 2026-2038, 1996.

[44] J. C. Barnard, I. Bojko and N. Hilleret. Desorption of H_2 and CO_2 from Cu by 5 keV Ar^+ and H_2^+ ion bombardment. *Vacuum*, 47(4): 347-350, 1996.

[45] C. M. Lyneis, P. Kneisel, O. Stoltz and J. Halbritter. On the role of electrons in RF breakdown. *IEEE Transaction on Magentics*, MAG-11(2): 417-419, 1975.

[46] W. Peter. Vacuum breakdown and surface coating of RF cavities. *Journal of Applied Physics*, 56(5): 1546-1547, 1984.

[47] R. Calder, G. Dominichini and N. Hilleret. Influence of various vacuum surface treatments on the secondary electron yield of niobium. Technical Report CERN-LEP-VA-87-61, CERN, 1987.

[48] Mauro Pivi. *Beam Induced Electron Multipacting in the CERN Large Hadron Collider Accelerator LHC*. PhD thesis, Università degli studi di Torino, 2000.

[49] I. R. Collins, O. Gröbner, N. Hilleret, J. M. Jimenez and M. Pivi. Electron cloud potential remedies for the vacuum system of the SPS. In Le Roux et al. [120], pages 150-154.

[50] G. Arduini, K. Cornelius, O. Gröbner, N. Hilleret, W. Höfle, J. M. Jimenez, J. M. Laurent, G. Moulard, M. Pivi and K. Weiss. Electron cloud: Observations with LHC-type beams in the SPS. In *7th European Particle Accelerator Conference* [118], pages 939-941.

[51] G. Arduini, V. Baglin, O. Brünig, R. Cappi, F. Caspers, P. Collier, I. R. Collins, K. Cornelius, R. Garoby, O. Gröbner, B. Henrist, N. Hilleret, W. Höfle, J. M. Jimenez, J. M. Laurent, T. Linnecar, E. Mercier, M. Pivi, F. Ruggiero, G. Rumolo, C. Scheuerlein, J. Tuckmantel, L. Vos and F. Zimmermann. Elecytron cloud effects in the CERN SPS and LHC. In *7th European Particle Accelerator Conference* [118], pages 259-261.

102

[52] Oliver S. Brünig. Simulations for the beam-induced electron cloud in the LHC beam screen with magnetic field and image charges. LHC Project Report 158, CERN, 1997.

[53] Miguel A. Furman. The electron-cloud effect in the arcs of the LHC. LHC Project Report 180, CERN, 1998. Also published as LBNL-41482/CBP Note 247.

[54] G. V. Stupakov. Photoelectrons and multipacting in the LHC: Electron cloud build-up. LHC Project Report 141, CERN, 1997.

[55] V. Baglin, I. Collins, B. Henrist, N. Hilleret and G. Vorlaufer. A summary of main experimental results concerning the secondary electron emission of copper. LHC Project Report 472, CERN, 2001.

[56] V. Baglin, I. Bojko, O. Gröbner, B. Henrist, N. Hilleret, C. Scheuerlein and M. Taborelli. The secondary electron yield of technical materials and its variation with surface treatments. In *7th European Particle Accelerator Conference* [118], pages 217-221.

[57] I. Bojko, J.-L. Dorier, N. Hilleret and Ch. Scheuerlein. Lowering the secondary electron yield of technical copper surfaces by strong oxydation. Vacuum Technical Note 97-19, CERN, 1997.

[58] Iouri Bojko, Noël Hilleret and Christian Scheuerlein. Influence of air exposures and thermal treatments on the secondary electron yield of copper. *Journal of Vacuum Science and Technology A*, 18(3): 972-979, 2000.

[59] N. Hilleret, V. Baglin, I. Collins, O. Gröbner, B. Henrist and G. Vorlaufer. The secondary electron yield of copper: New experimental results and their implications. In *International Workshop on Two-Stream Instabilities in Particle Accelerators and Storage Rings*, KEK, Tsukuba, Japan, 11 - 14 September 2001.

[60] M. Q. Ding and E. M. Williams. Electron stimulated desorption of gases at technological surfaces of aluminium. *Vacuum*, 39(5): 463-469, 1989.

[61] J. Goméz-Goñi and A. G. Mathewson. Temperature dependence of the electron induced gas desorption yields on stainless steel, copper and aluminium. *Journal of Vacuum Science and Technology A*, 15(6): 3093-3103, 1997.

[62] F. Billard, N. Hilleret and G. Vorlaufer. Some results on the electron induced desorption yield of OFHC copper. Vacuum Technical Note 00-32, CERN, 2000.

[63] M. Henzler, W. Göpel. Oberflächenphysik des Fest körpers. B. G. Teubner Stuttgart 1991.

[64] Ponec, V.; Knorr, Z.; Černý, S.: Adsorption on Solids, London: Butterworths 1974

[65] Hirschfeld, J. O.; Curtiss, Ch. F.; Bird, R. B.: Molecular Theory of Gases and Liquids, New York: Wiley 1964

[66] Esser, P.; Göpel, W.: Physical Adsorption on Single Crystal Zinc Oxide, Surf. Sci. **97** (1980) 309

[67] Flood, E. A.: Simple Kinetic Theory and Accommodation, Reflection and Adsorption of Molecules, in: Flood, E. A.: The Solid Gas Interface, Vol. 2, New York: Dekker 1967

[68] Devienne, F. M.: Accommodation Coefficients and the Solid-Gas Interface, in: Flood, E. A.: The Solid Gas Interface, Vol. 2, New York: Dekker 1967

[69] Rendulic, K. D.: The Influence of Surface Defects on Adsorption and Desorption, Appl. Phys. A **47** (1988) 55

[70] Hayward, D. O.; Trapnell, B. M. W.: Chemisorption, London: Butterworths 1964

[71] Clark, A.: The Theory of Adsorption and Catalysis, New York: Academic Press 1970

[72] Laidler,K. J.: Reaktionskinetik I, Homogene Gasreaktionen, Mannheim: Hochschultaschenbücherverlag 1970

[73] H. S. W. Massey, Atomic and Molecular Collisions (Halsted, New York, 1979).

[74] P. R. Antoniewicz, Phys. Rev. B **21**, 3811 (1980)

[75] Q.-J. Zhang and R. Gomer, Surf. Sci. **109**, 567 (1981); Q.-J. Zhang, R. Gomer, and D. R. Browman, *ibid.* **129**, 535 (1983); E. R. Moog, J. Unguris, and M. B. Webb, *ibid.* **134**, 849 (1983); P. Feulner, D. Menzel, H. J. Kreuzer, and Z. W. Gortel, Phys. Rev. Lett. **53**, 671 (1984);

Z. W. Gortel, H. J. Kreuzer, P. Feulner, and D. Menzel, Phys. Rev. B **35**, 8951 (1987); Z. W. Gortel, R. Teshima, and H. J. Kreuzer, *ibid.* **37**, 3183 (1988).

[76] Z. W. Gortel, Surf. Sci. **231**, 193 (1990); W. Hübner and K.-H. Bennemann, Z. Phys. B **78**, 131 (1990); R. E. Walkup, P. Avouris, N. D. Lang, and R. Kawai, Phys. Rev. Lett. **63**, 1972 (1989).

[77] Z. W. Gortel and A. Wierzbicki, Surf. Sci. **239**, L565 (1990)

[78] R. D. Ramsier and J. T. Yates, Jr., Surf. Sci. Rep. **12** (1991) 243-378.

[79] Z. W. Gortel, H. J. Kreuzer, P. Feulner and D. Menzel, DIET III, p. 173

[80] R. E. Johnson and M. Inokuti, Nucl. Instrum. Methods **206**, 289 (1983); C. T. Reimann, R. E. Johnson, and W. L. Brown, Phys. Rev. Lett. **53**, 600 (1984).

[81] F. Coletti, J. M. Debever, and G. Zimmerer, J. Phys. Lett. **45**, L467 (1984); T. Kloiber, W. Laasch, G. Zimmerer, F. Coletti, and J. M. Debever, Europhys. Lett. **7**, 77 (1988).

[82] N. Schwentner, E.-E. Koch, and J. Jortner, *Electronic Excitations in Rare Gas Solids*, Springer Tracts in Modern Physics Vol. 107 (Springer, Berlin, 1985); G. Zimmerer, in *Excited State Spectroscopy in Solids*, edited by U. M. Grassano and N. Terzi (Società Italiana di Fiscia, Bologna, 1987), p.36.

[83] F. V. Kusmartsev and E. I. Rashba, Czech. J. Phys. B **32**, 54 (1982).

[84] J. Schou, Phys. Rev. B **22**, 2141 (1980).

[85] O. Ellegard, Ph.D. Thesis, Risø National Laboratory, 1986 (unpublished).

[86] H. Niedrig, Scanning **1**, 17 (1978).

[87] J. Schou, Nucl. Instr. Meth. Phys. Res. B **27** (1987) 188-200.

[88] P. Sigmund, Phys. Rev. 184 (1969) 383; 187 (1969) 768.

[89] P. Sigmund, in: Sputtering by Particle Bombardment I, ed. R. Behrisch (Springer, Berlin, 1981) p. 9.

[90] J. Lindhard, V. Nielsen, M. Scharff and P. V. Thomsen, Mat. Fys. Medd. Dan. Vid. Selsk, 33, No. 10 (1968).

[91] O. Ellegard, J. Schou, H. Sørensen and P. Børgesen, Surf. Sci. 167 (1986) 474.

[92] W. L. Brown and R. E. Johnson, Nucl. Instr. and Method. B13 (1986) 295.

[93] B. J. Garrison and R. E. Johnson, Surf. Sci. 148 (1985) 388.

[94] O. Ellegard, R. Pedrys, J. Schou, H. Sørensen and P. Børgesen, to be published.

[95] R. Pedrys, presented at SOS 86, Symp. on Sputtering, Spitz (1986).

[96] P. Sigmund and C. Claussen, J. Appl. Phys. 52 (1981) 990.

[97] C. Claussen, Ph. D. Thesis, University of Odense (1982).

[98] C. Claussen, Nucl. Instr. and Meth. 194 (1982) 567.

[99] Karl Jousten. Pressure measurement with ionization gauges. In Turner [119], pages 7587. Also published as CERN Yellow Report CERN-99-05.

[100] J. H. Leck. Partial pressure measurement. In Turner [119], pages 8997. Also published as CERN Yellow Report CERN-99-05.

[101] Gernot Eder. *Atomphysik.* Wissenschaftsverlag, Mannheim Wien Zürich, 1989. 2., überarbeitete Auflage.

[102] P. A. Redhead, J. P. Hobson and E. V. Kornelsen, *The Physical Basis of Ultra-High Vacuum* (Chapman and Hall, London, 1968).

[103] D. O. Hayward, D. A. King and F. C. Tompkins, (a) Proc. Roy. Soc. (London) A **297** (1967) 305; (b) Proc. Roy. Soc. (London) A **297** (1967) 321.

[104] R. A. Baragiola, R. A. Vidal, W. Svendsen, J. Schou, M. Shi, D. A. Bahr, and C. L. Atteberrry, Nuclear Instruments and Methods in Physics Research Section B: Beam Interactions with Materials and Atoms **209**, 294 (2003).

[105] M. Shi, D. E. Grosjean, J. Schou, and R. A. Baragiola, Nuclear Instruments and Methods in Physics Research Section B: Beam Interactions with Materials and Atoms **96**, 524 (1995).

[106] R. E. Johnson and J. Schou, Mat. Fys. Medd. K. Dan. Vidensk. Selsk. **43**, 403 (1993).

[107] R. Pedrys, D. J. Oostra, A. Haring, A. E. de Vries, and J. Schou, Nuclear Instruments and Methods in Physics Research Section B: Beam Interactions with Materials and Atoms **33**, 840 (1988).

[108] T. Adachi, T. Hirayama, T. Miura, I. Arakawa, and M. Sakurai, Surface Science **528**, 60 (2003).

[109] J. Schou, P. Børgesen, O. Ellegaard, H. Sorensen, and C. Claussen, Physical Review B **34**, 93 (1986).

[110] P. J. Kisliuk, J. Phys. Chem. Solids **5**, (1958) 78.

[111] G. Ehrlich, 1966 General Electric Research and Development Report No. 66-C-023.

[112] J. L. Morrison and J. K. Roberts, Proc. Roy. Soc. (London) A **137** (1939) 1.

[113] O. Ellegaard, J. Schou, and H. Sorensen, Nuclear Instruments and Methods in Physics Research Section B: Beam Interactions with Materials and Atoms **13**, 567 (1986).

[114] N. Hilleret, A. Rossi, "Estimations of the Residual Gas Densities in the LHC Experimental Interaction Regions", LHC-Project Note 2003-xx

[115] W. C. Turner, Journal of Vacuum Science and Technology (A) **14**, 2026 (1996).

[116] O. Grobner, "The LHC vacuum system", PAC97, 1997, Vancouver, B.C., Canada.

[117] Peter J. Mohr and Barry N. Taylor. CODATA recommended values of the fundamental physical constants: 1998. *Journal of Physical and Chemical Reference Data*, 28(6): 1713-1852, 1999.

[118] *7th European Particle Accelerator Conference*, Vienna, Austria, 26-30 June 2000.

[119] S. Turner, editor. *CERN Accelerator School on Vacuum Technology*, Scanticon Conference Center, Snekersten, Denmark, 28 May - 3 June 1999. CERN. Also published as CERN Yellow Report CERN-99-05.

[120] P. Le Roux, J. Poole and M. Truchet, editors. *10th Workshop on LEP-SPS Performance*, Chamonix, France, 17-21 Jan. 2000.

107

[121] William H. Press, Brian P. Flannery, Saul A. Teukolsky, and William T. Vetterling. *Numerical Recipes.* Cambridge University Press, 1986. see also http://www.nr.com/ for an online version.

[122] Barry N. Taylor and Chris E. Kuyatt. Guidelines for evaluating and expressing the uncertainty of nist measurement results. NIST Technical Note 1297, NIST, 1994.

Appendix E

Acknowledgements

Appendix F

Curriculum Vitae

Herbert Tratnik
born on 8th of May, 1972 in Villach, Austria

Education

Sep 1978 - June 1982	Primary School
Sep 1982 - June 1986	Secondary School
Sep 1986 - June 1992	Technical High-School (HTL), "Matura" degree obtained June 1992
Oct 1992 - June 2002	Vienna University of Technology, department of general physics, masters degree in "Business Management in Physics" obtained June 2002
Nov 2002 - Nov 2005	Doctoral student at CERN, defence of the thesis October 2005

Professional experience

Aug 1988	Siemens Villach, Austria (Department of Photo Technology), collected and statistically evaluated data for parameter verification of semiconductor chips.
July 1991	Post and Telegraph Administration Villach, Austria, theoretical and practical experiences and applications in telephone extensions for subscribers.
July 1998 - Oct 1998	Siemens Villach, Austria (Department of Photo Technology), operated the lithography procedure of semiconductor chips.
July 1999 - Oct 1999	Infineon Villach, Austria (Department of Product Technology), collected and statistically evaluated data for Quality Control of semiconductor chips.

Other biographic data

Apr 2001 - Dec 2001	military service